PASSIVE STABILIZATION OF FLYWHEEL MAGNETIC BEARINGS

by
PAUL ALAN BASORE

B.S., Oklahoma State University
(1978)

SUBMITTED IN PARTIAL FULFILLMENT
OF THE REQUIREMENTS FOR THE
DEGREE OF

MASTER OF SCIENCE

at the

MASSACHUSETTS INSTITUTE OF TECHNOLOGY

February 1980

© Massachusetts Institute of Technology

Signature of Author Signature redacted
Department of Electrical Engineering and Computer Science,
February 1, 1980

Certified by Signature redacted
Richard D. Thornton
Thesis Supervisor

Accepted by Signature redacted
Arthur C. Smith
Chairman, Department Committee

ARCHIVES
MASSACHUSETTS INSTITUTE OF TECHNOLOGY
MAR 25 1980
LIBRARIES

PASSIVE STABILIZATION
OF
FLYWHEEL MAGNETIC BEARINGS

by
Paul Alan Basore

Submitted to the Department of Electrical Engineering and Computer Science on February 1, 1980, in partial fulfillment of the requirements for the Degree of Master of Science.

ABSTRACT

A theoretical study was conducted to analyze ultra-reliable mechanisms for the stabilization of magnetically-levitated flywheels. The goal was to improve the reliability, efficiency, and lifetime of flywheel energy storage systems by incorporating the desirable features of magnetic levitation without requiring the use of active feedback-control circuitry. Although stationary free magnetic systems cannot maintain a stable equilibrium without external control, rotating systems are capable of self-stabilization. When a displacement occurs from equilibrium, currents induced in properly placed conductors draw energy directly from the rotor. These currents can be used without active processing to provide the necessary restoring force.

A study of flywheel mechanics was conducted to insure compatability of the stabilization mechanism with the rest of the energy storage system. The multi-rim, multi-material rotor was selected for study, with the inner surface used for levitation and propulsion. A study of magnetic levitation was also attempted, with emphasis on performance limitations. Both analytical and computer models were utilized to evaluate the effect of a toothed air-gap structure. The effect is described by four dimensionless factors normalized to the case of opposing flat plates. Levitation by transverse shear force requires six times the volume of magnets compared to flat plates.

A stabilization scheme which utilizes the same homopolar field as is used for levitation is proposed. A dominant feature of this mechanism is that it dissipates very little power, approaching zero under axisymmetric conditions. The system consists simply of conductors placed on the rotor either in the gap or in slots. Several models emphasizing different aspects of the system are combined to include effects of discrete conductors, toothed gap structure, and finite iron permeability.

Scaling laws for the rotor, levitation, and stabilization sub-systems were derived. For 10^8 Joules of storage, appropriate for residential applications, the rotor would have a mass of 1000 kg and require 25 kg of ceramic magnets to provide the lift. The system would have a maximum speed of 200 Hz, but would be stable above 6 Hz. The translational stiffness at full speed would be 270 N/mm, yielding a fundamental oscillation frequency of 2.6 Hz.

Thesis Supervisor: Richard D. Thornton
Title: Professor of Electrical Engineering

ACKNOWLEDGMENTS

The research described in this presentation has been funded through fellowships, the sources of which deserve recognition and genuine appreciation. Funding for the first year was provided jointly by the Tau Beta Pi fellowship board and the MIT EECS graduate office. The EECS office continued its support though the summer of 1979.

Professor R.D. Thornton's commitment to solar energy, combined with his experience and expertise in electromechanics, provided important support and direction in this project. Professor J.R. Melcher and the members of the Continuum Electromechanics group at MIT did much to make graduate study worthwhile, both by introducing the fascinations of electromechanics and for accepting the author as one of their own. This applies especially to office-mates Al Presser and Rick Ehrlich.

Finally, there is the essential support offered by my wife, Nancy, who has been an inspiration throughout and of crucial assistance in preparing this document under very trying conditions.

TABLE OF CONTENTS

LIST OF FIGURES

I. INTRODUCTION

A. Energy Utilization

Of the problems which plague modern society, the availability of energy is certainly among the most pressing. Faced with depletion of the domestic energy supply and an unacceptable dependence on imported oil, the nation is beginning to devote more attention to the development of alternate sources of energy and to making the best use of the energy which is available. Energy storage is a key factor in both efforts.

One of the most attractive energy alternatives is the direct conversion of sunlight into useful forms. Because of their diffuse nature, environmentally-derived energy sources perform best in a distributed capacity. By eliminating scaling factors which in the past favored centralization of facilities, the application in which solar energy has its greatest potential is in meeting residential energy needs on an individual-home basis. By locating the source at the point of consumption, transmission losses are eliminated and "waste heat" can be utilized. A distributed generation scheme also increases the national security by avoiding the vulnerability to aggressors and terrorists inherent in any highly-centralized system. The problem with environmental sources, however, is their intermittent character. Energy storage is

needed to obtain full use of the available power.

Of the two components of residential energy demand, thermal and electrical, efficient storage of electrical energy is the more acute problem. Yet electricity accounts for from 30 percent (in Madison, Wisconsin), to 85 percent (in Phoenix, Arizona) of the total consumption [20], and nationwide the thermal-electrical split is nearly even [25].

Both solar and wind energy are capable of supplying a great part of the electrical demand of homes [53], and both solar photovoltaics and wind power systems show signs of future cost reduction [23, 62]. The development of an efficient means of storing energy on a residential level, however, is a major complication in reaching the potential of these sources.

Clearly, energy storage is also important in making full use of conventional generating facilities. Efficient base-load generators could run full-time, and peak-handling would be accomodated through the energy-storage system. The storage could take place either at the utility level, or distributed at the consumer level. Actually, an individual homeowner can afford to pay four times as much per kilowatt-hour of storage as a small utility [37], so strong scaling incentives would have to exist for building a utility-sized unit before that option could be considered.

Electrical energy storage mechanisms are desirable now, and will be essential in the future if solar and wind power are to supply a significant fraction of this country's energy

needs. The problem remains that suitable energy storage schemes simply do not currently exist.

B. Energy Storage

Energy storage systems can be classified according to the form in which the energy is stored:

1. Thermal (hot water, hot rocks)
2. Chemical (battery, hydrogen)
3. Mechanical stress (springs, compressed gas)
4. Potential energy of gravity (pumped hydro)
5. Mechanical inertia (flywheels)
6. Electric fields (capacitors)
7. Magnetic fields (superconducting rings)

Of these various alternatives, thermal storage of electrical energy is too inefficient, capacitors are too bulky, and springs too costly for storing large amounts of energy. Because of complexity and supplemental hardware, superconducting rings and hydrogen are only being considered for utility-sized applications. Pumped hydro and compressed gas require large volumes of fluid and the reservoirs to store them in, generally restricting these options to utilities as well. Batteries and flywheels alone seem well adaptable for small-scale applications.

The feasibility of these various options has been studied by several groups. Studies performed at Sandia [37], General Electric [17], and MIT's Lincoln Lab [49] all concluded that,

except for geographical locations where pumped hydro or compressed gas facilities existed naturally, the residential storage schemes were generally more viable than the utility-sized options. Since residential-sized systems can be used with solar energy systems as well as for conventional peak-handling, they will be the initial focus of attention for this study.

The General Electric report shows that to be economically justified, a residential storage system must cost less than $100 per kw-hr (1976 dollars). This figure does not include inflation, peak power pricing, or using the waste heat from storage to meet thermal needs; all of which permit an even higher cost for a viable system. Also shown in the report is that when used with a photovoltaic system the increase in energy capture due to storage increases nearly linearly up to 25 kw-hr of capacity, then flattens off quickly. Twenty-five kw-hr is thus an appropriate figure to select for the proper size of a residential storage system. This figure is also used in the Lincoln Lab study. With this amount of storage, a typical residence would recover 500 kw-hr per year of additional energy through storage. This level of storage would also allow virtual independence of the power grid as it amounts to a full day's storage for most households.

Based on existing technology, the General Electric study found batteries to be the most competitive system, followed by flywheels. The Sandia study, on the other hand, found flywheels to be the best, though not yet economical. The

Lincoln Lab study found flywheels to be less expensive than batteries if the cost of a blow-out wall is added to the battery system to protect against the threat of explosion. The facts from these studies make it apparent that while the batteries themselves tend to appear less expensive; from a systems-analysis standpoint, the flywheel is superior. Batteries suffer from short life, frequent maintenance, inefficient peak-power capability, the threat of explosion, and disposal difficulties. By comparison, flywheels are long life, low maintenance, efficient devices. They do require a vacuum environment and are best located underground to protect against rotor failure. Research is underway on both battery and flywheel systems. Flywheels appear to have a great potential for improvement, and appear to be preferable for widespread residential use.

C. Flywheels

The first use of a flywheel in the generation of electrical power was in conjunction with a Soviet windmill built in 1920. Momentum wheels, until only recently, have only stored about 0.1 watt-hour (WH) per kilogram (kg) of wheel mass [60]. Tensile stress is the limiting factor in flywheel energy storage, so with the development of high-strength, light-weight materials in the 1960's for the space program, the progress of flywheel technology was destined to explode. The revolution in flywheel design was

signaled by an article in the December, 1973 issue of Scientific American [57]. The article analyzed flywheel capabilities, and proposed designs capable of storing 870 WH/kg of rotor mass! This figure, based on ideal material behavior, was grossly optimistic. However, ensuing efforts to design flywheel systems for spacecraft (at Rockwell [54] and Sperry Flight System [64]), and for automobiles (at Garrett Airesearch [22] and General Electric [45]), supplemented work at several universities in generating a great deal of information about the true capabilities and limitations of the new storage medium. Most of the work was funded by the government through ERDA (now DOE), with Sandia and Lawrence Livermore Labs coordinating the effort.

The first flywheel technology symposium was held in November, 1975 at Berkeley, California [58]. Most of the papers presented dealt with the fundamental analysis of flywheel rotors and rotor materials. Only one rotor utilizing the new concepts had actually been built and tested. Rockwell's flywheel stored a total of 892 WH, with an efficiency of 17.2 WH/kg. The rotor was made of expensive titanium, however, and the real promise clearly lay in the use of anisotropic fiber-composite materials.

By the time a second symposium was held in October, 1977, Rockwell had improved its module to 30 kWH-hr of storage and 25 WH/kg, still using titanium [15]. Union Carbide used Kevlar-49/epoxy composite to obtain 250 WH at 22 WH/kg [34]. In the past two years, composites have taken their rightful

lead, with Garrett's demonstration of 55 WH/kg using a combination of Kevlar and S-glass/epoxy [18]. General Electric has managed to obtain 1.3 kWH at 22 WH/kg with E-glass and Kevlar [46], and several rotors of 4340 steel have been built by General Electric and others with 22 WH/kg of storage [45].

Based on these results, a 750 kg rotor costing around $2500 could recover some 150 thousand additional kWH from a residential solar array over its 30 year expected lifetime. The resulting storage cost of less than two cents per kWh represents an excellent investment even at today's low energy prices. Unfortunately, the cost of supporting the flywheel and transferring power to and from it adds tremendously to this base cost. Even the most optimistic production-quantity price estimate for a complete system using existing technology is $12,000 [49].

Many factors contribute to the high cost of a flywheel system. Most arise from the high speed required and the need to make the accessary components match the long, maintenance-free qualities of the flywheel itself. Conventional bearings meeting these requirements are of the hydrodynamic variety, which are complicated and expensive [63]. In a 30 kWH flywheel system recently developed by Rockwell, mechanical bearings were used and the losses they introduced amounted to 20 kW [32]. The rotor must operate in a vacuum because of its high speed, thus a vacuum pump and rotating seals are needed in addition to the enclosure itself. A variable speed

motor-generator is required, along with the associated input/output electronics.

Several novel ideas indicate that new possibilities exist for designing a lower-cost flywheel system. The most important area where a significant advance is possible is to use magnetic, non-contact bearings. Although the technology of magnetic bearings is not well developed, several different designs have been proposed and tested. Permanent magnets can be used to provide the levitating force, cutting losses substantially. Since there is no contact, the life of a magnetic bearing should exceed that of all other components. Furthermore, magnetic bearings are well suited to the ten-to-twenty thousand rpm speeds necessary. If made from inexpensive ceramic magnets, the bearings can support over 100 times their own weight, making their cost only a small fraction of the cost of the flywheel rotor. Another important advantage is that since these bearings require no lubricant, generate very little heat, and are virtually maintenance-free; they can be placed with the flywheel inside the vacuum housing. Since no seals are then needed, the vacuum can retain its integrity over periods of months or years. Consequently, only a periodic repumping would be required, and the cost of an on-site vacuum pump is eliminated.

Another area for improvement is in the mechanical coupling to the rotor. Present designs use hub-and-axle configurations. Since materials expand radially when spun, tying the composite rotor to its axle is a major source of

stress concentration and premature failure [9]. Magnetic levitation, by its distributed nature, does not require a spindle for support. If, in addition, the motor-generator is made an integral part of the rotor assembly, then no axle would be required [40]. Elimination of the axle could be a great help in controlling unstable whirl modes in the rotor, as well [66].

Although magnetic bearings have been used for flywheel support, the full potential of magnetic levitation has not been realized. By incorporating the flywheel, motor-generator, and support into a simple, unified design; the cost of a complete flywheel system could be reduced significantly and the reliability increased through sheer simplicity.

D. Magnetic Bearings

With all of their advantages, a single complication has prevented the widespread use of magnetic bearings - they are all statically unstable and require some form of dynamic feedback to retain equilibrium. The fact that stability is impossible in any static system of particles whose forces vary as the inverse square of distance was first proven by Samuel Earnshaw in 1842 [18]. The picture was changed slightly in 1939 when Braunbek showed that stability was possible for objects whose permeabilities are less than that of free space [7]. Some materials are diamagnetic at room temperature, but the effect is far too weak to provide effective levitation

[43].

The nature of the required dynamic feedback can take many forms, but can generally be classified as active, tuned-circuit, or eddy-current. Active methods rely on sensing the position of the levitated object and feeding current as needed to control coils in the magnetic circuit. An external electronic control system is required. Tuned-circuit methods require that alternating current drive the lift coils. By using the levitation windings as a variable inductance in an L-C circuit, proper tuning can result in static stability. Dynamic stability, however, requires either eddy-current damping or the addition of non-linear elements to the circuit [39]. Eddy-current repulsion occurs when a conductor is subjected to a changing magnetic field. Forces are induced which attempt to reduce the generated currents according to Lenz's law, and stability can be obtained.

The eddy-current method has been used to levitate molten metals [33] and recently as the support mechanism for high speed transportation [68]. The power dissipation in both of these applications is very high, however, and this has precluded consideration of this technique for flywheel systems [64]. The power loss can be avoided by using superconductors, but the added cost and complexity of cryogenic equipment eliminated this option as well.

Tuned-circuit levitation was developed almost entirely at MIT's Instrumentation Lab (now Draper Lab) starting in 1953. The purpose of these devices was attitude sensing,

particularly for spacecraft, where the levitated member can be made very small [21]. Since all of the levitation force in these devices comes from current-carrying coils, the power required to support large masses is excessive for a flywheel storage system, where energy is at a premium [64].

The first active-feedback levitation schemes also relied entirely on electromagnets for the lift force. It was soon realized, however, that a great improvement could be made by using permanent magnets to provide the basic lift. Only enough current to maintain stability would then need to be fed the control coils. The first "virtually zero power" magnetic bearing with significant lift was built in 1971 by the Cambridge Thermionic Corporation [31]. All magnetic bearing designs proposed since then have utilized the actively-controlled permanent-magnet scheme.

There are a variety of ways of arranging permanent magnets and iron pieces to obtain levitation of a rotor. The options include horizontal versus vertical shaft, attraction versus repulsion, axial versus radial magnetization, selection of magnet material, and axial versus radial feedback control. A thorough discussion, including illustrations of all of these various possibilities is provided in a book by P. Geary [24]. In making these design choices, the specific application of the bearing has a large impact. The most important features for a flywheel system are low cost, reliability, and high lift-force capability. Less important are size and weight considerations.

Beginning with the choice of axis orientation; the flywheel is most easily contained safely in the event of rotor failure if it is spinning about a vertical axis and is located below ground. This requirement does subject the flywheel to precess with the earth's rotation, thus imposing a constant torque on the bearings which should be considered.

Attraction systems are nearly universally preferred over repulsion schemes in recent literature. In an attraction system, iron pole-pieces can be used to smooth out inhomogeneities in the magnet's flux. This is not practical in repulsion systems, and higher losses result. Also, attraction systems confine the flux more than repulsion techniques, thus reducing the generation of eddy currents in nearby conductors [49]. Finally, since repulsion systems impose severe demagnetizing fields on the magnets involved, such designs preclude the use of inexpensive magnet materials.

Magnetizing the magnet in an axial direction is generally easier than radially. Only one successful flywheel bearing with radial magnets has been reported, that being at Lincoln Lab [49].

Lured by high performance and the promise of future cost reductions, magnetic bearing designers have been drawn almost without exception to rare-earth-colbalt magnets. Cobalt has proven to be a critical problem, however. A by-product of copper and nickel mining, cobalt is fairly scarce and already 20% of all cobalt goes to the magnet industry. As a result, the price is increasing at the rate of 15% per year [78].

These price hikes have also had their effects on the less expensive Alnico magnets, which also contain cobalt. In fact, the current prices run \$100/kg for $SmCo_5$ and \$45/kg for Alnico V [16]. Use of these materials in a system designed for widespread use is virtually eliminated.

The lower performance of ceramic magnets means that about ten times as much magnet mass is required to do the same job when compared to rare-earths, but the low price of only \$4/kg makes them actually less expensive [16]. The materials comprising these magnets is in comparatively plentiful supply. The use of samarium-cobalt despite this situation can be attributed to the fact that magnetic bearings have been designed directly for, or at least influenced by, use in spacecraft where weight is very important.

In 1977, researchers at Matsushita, in Japan, developed a new manganese-aluminum magnet. They are very similar to ceramic magnets, but have a higher residual flux. Compared to rare-earths, these new magnets require only five times as much mass, yet because they are made of inexpensive elements, should cost no more than ceramics [78]. The long term performance of the magnets is not yet known, however, and they are not available in quantity [16].

The simplest way to obtain complete stability with magnetic bearings is the axial-active, radial-passive scheme using two bearings. The general topology is shown in figure 1.1a. If the two bearings are separated axially by a sufficient distance, then the radial restoring forces will

Figure 1.1

MAGNETIC BEARING CONFIGURATIONS

a. Axial-Gap Bearing

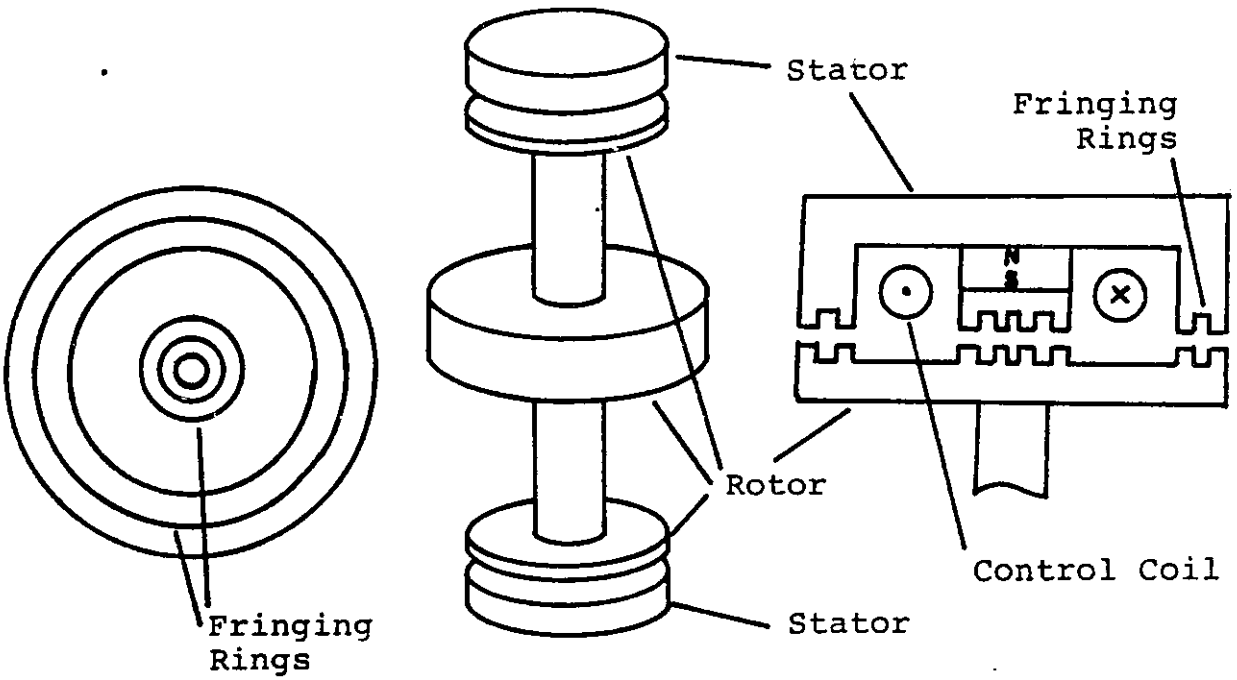

b. Radial-Gap Bearing

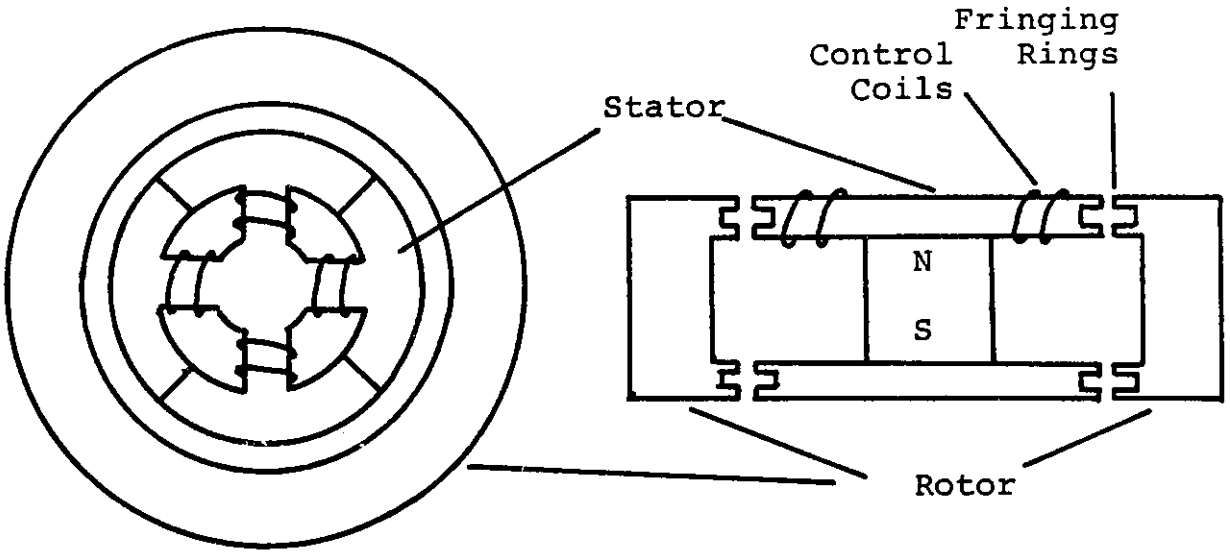

overcome the torsional instability which is characteristic of opposing plates. Active control is thus needed in only one axial dimension. Because of its simplicity, this approach was used in the early bearings of Cambridge Thermionic and Sperry [64] and is planned for use in the residential flywheel system being developed at Lincoln Lab [36].

The one great disadvantage of the radial-passive design is the low radial stiffness which can be achieved. Because of this, radial-gap motor-generators are difficult or impossible to use because of the radial imbalance forces they create [31]. The alternative is to use an expensive axial-gap motor-generator system and both the Cambridge Thermionic and Lincoln Lab designers chose this route.

The obvious way to maintain high stiffness in the radial direction is to make this the actively-controlled direction. The topology for this, the radial-active, axial-passive design, is shown in figure 1.1b. Angular stability with this design is obtained by making the radius sufficiently larger than the height of the bearing surfaces. General Electric in 1973 [31], Rockwell in 1974 [54], and James Kirk [42] and Philip Studer [45] in 1977, all presented designs for radially-active bearings, though none have used more than small (20 kg) rotors. As expected, several sacrifices are demanded in using this design. Two control system channels are required instead of one, and they are more complex than for radial-passive designs because allowance must be made for radial expansion of the spinning ring. The control windings

add axial asymmetry to the bearing, thus increasing hysteresis losses in the rotor [45].

Whatever form the levitation and stabilization mechanisms may take, they will require some power dissipation. If the resulting heating takes place on the rotor, then the heat can only be transferred out to the surroundings by radiation through the vacuum. To avoid excessive rotor temperature, a dissipation of no more than about 100 watts can be handled in this way for a 1000 kg rotor. The loss in these systems should also be less than that of the motor-generator system to avoid degrading the overall efficiency. This requirement also limits the dissipation to around 100 watts for a residential unit.

Another factor which must be entered into the design process is the flywheel's response to ground motions. Besides handling everyday vibrations without consequence, the unit must survive moderate earthquakes with only minimal damage.

Figure 1.2 summarizes the basic characteristics of the magnetic bearings which have been designed and built for flywheel support, as reported in the literature. The design options just discussed constitute the basis for comparison.

In summary, flywheels were found to be the most promising mechanism for electrical storage at the residential level. The use of magnetic bearings has been shown to offer the potential for considerable cost reduction in the complete flywheel system. In order to achieve this effectiveness, the magnetic bearing should possess these qualities:

Figure 1.2

CHARACTERISTICS OF COMPLETED MAGNETIC BEARINGS

Manufacturer	Rotor Mass (kg)	Active Control	Magnet Material	Magnetization	Date	Ref.
Cambridge Thermionic	3.6	axial	none	none	4/70	31
NASA/Goddard	9.1	axial	-	axial	1970	31
Cambridge Thermionic	4.1	axial	$SaCo_5$	axial	1972	31
General Electric	18.2	radial	-	axial	2/73	31
Cambridge Thermionic	22.7	both	$SaCo_5$	-	6/74	31
Sperry	29.1	axial	$SaCo_5$	axial	8/74	64
Aerospatiale (France)	10.3	axial	-	-	11/75	70
NASA/Goddard	.3	radial	$SaCo_5$	axial	9/77	65
MIT Lincoln Lab	68.2	axial	$SaCo_5$	radial	12/78	49

1. Require no axle connection to the rotor.
2. Be compatible with vacuum containment.
3. Operate at speeds up to 20,000 rpm.
4. Permit the use of a radial-gap motor-generator.
5. Dissipate less than 100 watts of power.
6. Allow the efficient use of ceramic magnets.
7. Incorporate the most reliable stabilization possible.
8. Withstand ground shocks with minimal damage.

By reinvestigating the fundamental concepts of magnetic levitation, the possibility exists to generate improved bearing designs.

E. Passive Stabilization

The term "passive" is applied in the literature both to refer to tuned-circuit levitation methods [21] and to the use of permanent magnets [77]. In the text which follows the term is used to describe any permanent-magnet levitation system where the dynamic feedback mechanism is an integral part of the bearing itself, and no external active control circuits are required. According to Earnshaw's theorem [18], such a system is necessarily unstable for stationary elements. However, in normal operation a flywheel bearing always has a rotating member, so Earnshaw's theorem does not apply, and opportunities for passive stability do exist. As long as the flywheel is turning, the energy needed to provide stability can be drawn directly from the rotor. If this stability can

be maintained down to slow enough speeds, then simple mechanical touch-down bearings can be provided to prevent contact between bearing surfaces during cold starts.

The manner in which power is obtained from the rotor can take one of two identifiable forms. One option is to use discrete coils of wire to generate current in proportion to the location of the rotor. If this coupling is strong enough, the output of the coils can be fed directly to control coils to provide the necessary corrections and obtain stability. This passive mechanism is really a limiting form of active stabilization.

Instead of constraining the current to discrete coils, the current could be allowed to flow in a continuous sheet of conducting material. This option thus becomes in reality an extension of the eddy-current levitation scheme. The difference is that current need only flow to correct for deviations from equilibrium, as the magnets provide the basic lift force.

An advantage shared by both of these passive schemes is clear: they eliminate the need for a complex control system, thus increasing the reliability of the system. These methods reduce both insulation and connection problems, and remove dependence on failure-prone power semiconductors. The disadvantage lies in having less room for adjustment after the system has been installed. The passive current-coil approach holds promise primarily if the same coils can serve double-duty as a part of the motor-generator system. The

eddy-current method, however, is by far the simplest and most durable option available. Furthermore, it opens an entirely new dimension of control because of its distributed nature.

Whether or not this concept can be used to overcome the limitations of existing bearing designs and successfully obtain the qualities listed previously is a question which has never been adequately addressed. In fact, in order to locate any previous mention of passive stabilization requires looking beyond the bounds of the immediate application.

During the early and mid 1970's, a great deal of work was performed in analyzing the generation of eddy currents in conductors by magnetic fields, as a part of a program to develop magnetically-levitated, high-speed ground transportation. Although in a considerably different context from flywheel bearings, many of the results are nevertheless useful. Good analytical results are given by Miericke and Urankar [48], Lee and Menendez [44], and Borcherts [6].

In the only presentation of a passive levitation scheme in recent literature, Jung and Rinnert of the University of Karlsruke, West Germany proposed that a high-speed vehicle could be levitated by permanent magnets and stabilized by the same eddy-current mechanisms being considered for vehicle levitation [38]. The 1977 article unfortunately offers no details of the stabilizing system, and the analysis of the permanent magnets simplistically treats them as point sources. Under conditions where this limit is valid, the scheme is completely useless for providing lift.

In an earlier 1975 article, R.D. Thornton of MIT suggested that an optimum design for a magnetically-levitated vehicle might incorporate aspects of both ferromagnetic and eddy-current schemes. The idea was not pusued, however, and no mention was made of using the eddy-currents to stabilize the ferromagnetic system [68].

The closest anyone has come to suggesting a passive approach for flywheel bearings was in 1975 at the flywheel technology symposium, when Aaland and Lane of Lawrence Livermore Lab demonstrated that eddy currents could support a small alluminum rotor stably, but they did not proceed with the issue or mention the incorporation of permanent magnets to provide the basic lift force.

The potential of the unexplored concept of passive magnetic bearings provides an excellent opportunity for reducing the cost of flywheel energy storage, and is thus the topic which the following presentation will address.

II. FLYWHEEL MECHANICS

The cost of the flywheel rotor, including fabrication, is the largest single expense in the energy storage system. The usefulness of any improvements in reliability or efficiency must be weighed against their effect on the cost of the rotor. For this reason, the particular requirements of cost-effective rotor design must be understood and their impact reflected in the design of the magnetic bearing and stabilization systems.

As mentioned in the introduction, desirable attributes of the system include elimination of the hub and axle, and provision for a radial-gap motor-generator. Because high-permeability iron is not particularly strong, it must be placed on the rotor in locations where stresses are not large. Thus the outer surface of the rotor cannot be used as an effective motor-generator interface, leaving the inner surface of an annular rotor as the primary alternative. The rotor geometry which is consistent with these requirements is the multi-rim design proposed by Post and Post [57]. The question to be answered is how this restriction on the rotor geometry affects the performance and cost of the flywheel.

The conditions which the rotor performance places on the levitation system are also of interest. Of particular concern are the total mass of the rotor for a given energy storage capacity, the speed of the rotor, the area on the inner edge of the annulus available for levitation, and the effect of

flywheel dynamics on magnetic bearing design.

The shape factors derived in section B have been given previously by Kirk [40], Gerstle and Biggs [58], and Rabenhorst [60]. The solution for stress in flat disks is taken primarily from Danfelt, Hewes, and Chow [14]. Although the multi-rim concept is well established, the method of analysis used in section D is original, as are the conclusions reached in section E concerning gyroscopic effects.

A. Fundamental Relations

When an axisymmetric mass is spun about its center of gravity, the energy stored is found from the simple relation

$$E = \tfrac{1}{2} J_p \Omega^2 \qquad (2.1)$$

where Ω is the rotational velocity in radians and J_p is the polar moment of inertia about the primary spin axis:

$$J_p = \int r^2 dm = \int r^2 \rho dV \qquad (2.2)$$

The amount of rotational energy which can be stored in a given piece of material is limited by the tensile stresses which result from the centrifugal force. The mass should never be spun so fast that the maximum stress found anywhere in its interior exceeds the linear elastic range. For objects restricted to this linear regime, the stress can be shown to be proportional to $\rho\Omega^2$. This can be readily defended simply on the basis of dimensional analysis.

For rotors having uniform material properties, ρ is constant so that

$$E = \tfrac{1}{2}\,\rho\Omega^2 \int r^2 dV \qquad (2.3)$$

Thus the energy stored is directly proportional to the stress in the material. Because of this, it is tempting to think that the energy is effectively stored in stretching of the inter-atomic bonds. Energy storage in flywheels in no way relies on the use of an elastic material, however, so such a view is fundamentally incorrect and can be quite misleading.

The important considerations in flywheel design are energy stored per kilogram of material and energy stored per dollar of material. The latter is immediately obtainable from the first if the material cost is known, so the maximum energy storage per kilogram of flywheel, the specific energy, is a useful description of performance. By dividing equation 2.3 by the mass of the rotor:

$$E_s = \frac{E_{max}}{M} = \frac{\tfrac{1}{2}(\rho\Omega^2_{max}) \int r^2 dV}{(\rho V)} = \frac{\sigma_{max}}{\rho} K_s \qquad (2.4)$$

The advantage of this representation is that the dimensionless constant K_s is nearly independent of material properties. σ_{max}/ρ, on the other hand, is a purely intrinsic quantity. Thus concerns about topology are effectively decoupled from selection of material.

B. Rotor Geometry

The particular rotor geometries which are of interest for flywheel energy storage are shown in figure 2.1. The relative performance of these designs is largely contained in the value of K_s, called the "shape factor". This factor can be analyzed for all of these proposed configurations. The initial step is to calculate the stress profile in the material. From this the maximum stress can be found and a value of K_s derived.

In general, both radial and circumferential stresses are induced in the material, but certain of these geometries strongly favor one or the other. This makes it possible to use anisotropic materials which may have very high longitudinal tensile strength, but low transverse strength. Only those configurations shown as figures 2.1d and 2.1e are candidates for these materials. Aside from this restriction, the designs can be compared with little regard for which material is used.

The design of figure 2.1a has been found to have a nearly constant stress throughout [73]. Referred to as the Stodolla disk, or simply "constant stress disk", this option has the highest possible shape factor, approaching unity. The thin ring, figure 2.1d, and the brush configuration, figure 2.1e, can be assumed to have uniform uniaxial stress over their cross sections.

The solid disk and the pierced disk require more effort

Figure 2.1

ROTOR GEOMETRIES

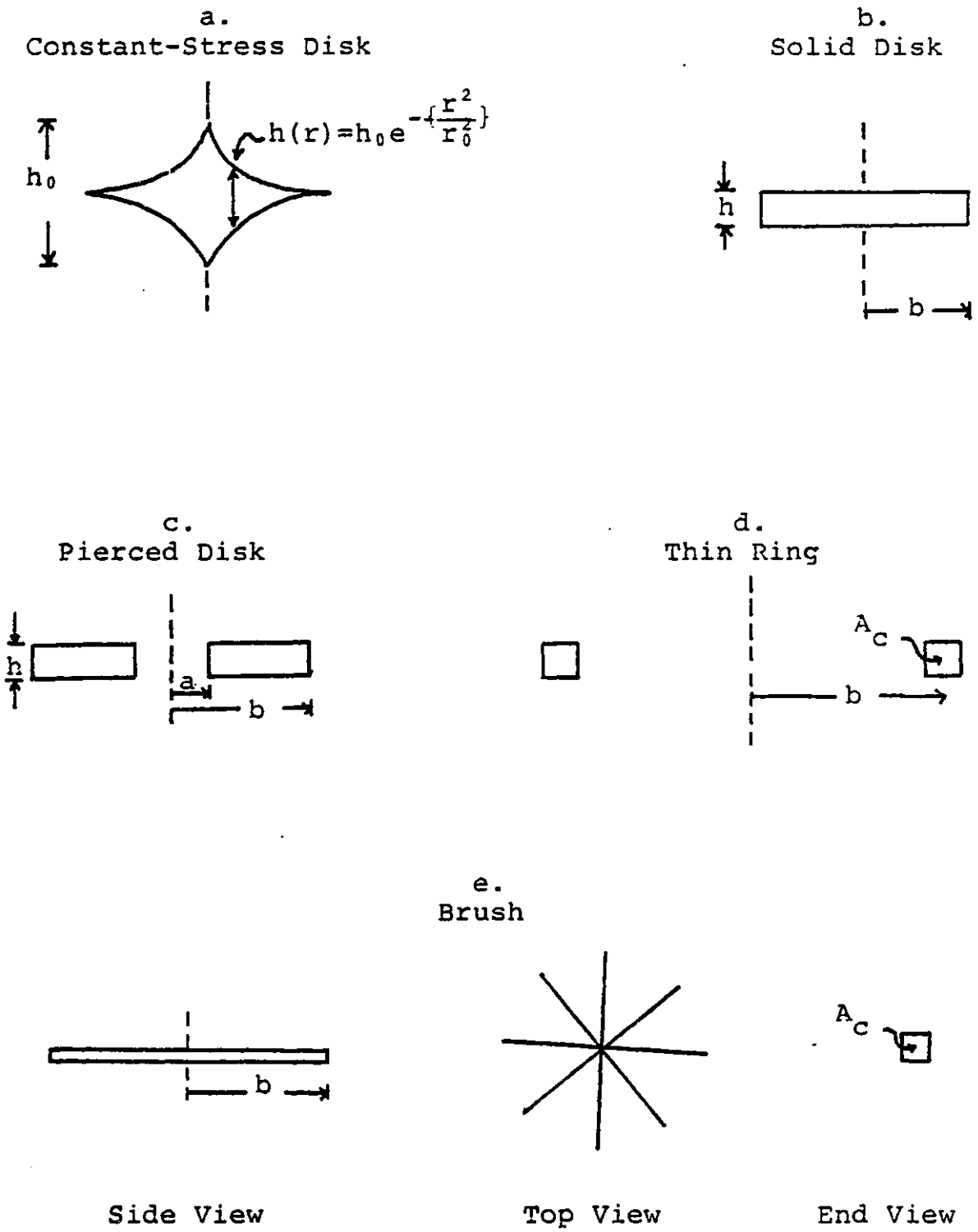

to obtain results. Neglecting gravity, recognizing that $E_r\nu_{\theta r}=E_\theta\nu_{r\theta}$, and defining $\lambda=\sqrt{E_\theta/E_r}$ as the anisotropy factor, solutions for the radial stress are of the form

$$\sigma_r = a_1 r^{\lambda-1} + a_2 r^{-\lambda-1} - \frac{(3 + \nu_{\theta r})\rho\Omega^2}{9 - \lambda^2} r^2 \qquad (2.5)$$

where Poisson's ratio ν_{ij} represents contraction in the j direction due to stress in the i direction, and E_k is Young's modulus in the k direction. The two boundary conditions to set values of a_1 and a_2 are that the radial stress is zero at the inner and outer surfaces, designated as r=a and r=b respectively. The resulting stress and displacement expressions are given in figure 2.2. These expressions have been evaluated for the isotropic case and two representative anisotropic situations for a range of inner-to-outer radius ratios. These stress profiles are shown in figures 2.3, 2.4, and 2.5. Note that over the range of interest for anisotropic materials, their behavior is well approximated by the isotropic relations. This exemplifies the fact that the stress, and hence the shape factor, are virtually independent of material properties. A simple formula for the maximum stress is possible for the isotropic case, and this is given along with the shape factor for all of the rotor geometries in figure 2.6.

It should be clear that the thin ring is simply a limiting case of the pierced disk. Using the results for a pierced disk it is now possible to determine just how thin the

Figure 2.2

PIERCED DISK STRESS PROFILES

Radial Stress

$$\sigma_r = \frac{(3+\nu_{\theta r})\rho\omega^2 b^2}{9-\lambda^2}\left\{C_1\left(\frac{r}{b}\right)^{\lambda-1} + C_2\left(\frac{r}{b}\right)^{\lambda-1} - \left(\frac{r}{b}\right)^2\right\}$$

$$C_1 = \frac{(b/a)^{\lambda} - (a/b)^3}{(b/a)^{\lambda} - (a/b)^{\lambda}}$$

$$C_2 = \frac{(a/b)^3 - (a/b)^{\lambda}}{(b/a)^{\lambda} - (a/b)^{\lambda}}$$

Circumferential Stress

$$\sigma_\theta = \frac{(1+3\nu_{r\theta})\lambda^2\rho\omega^2 b^2}{9-\lambda^2}\left\{C_3\left(\frac{r}{b}\right)^{\lambda-1} + C_4\left(\frac{r}{b}\right)^{-\lambda-1} - \left(\frac{r}{b}\right)^2\right\}$$

$$C_3 = \frac{(b/a)^{\lambda} - (a/b)^3}{(b/a)^{\lambda} - (a/b)^{\lambda}} \frac{(1+\lambda\nu_{r\theta})(3+\nu_{\theta r})}{(\lambda+\nu_{\theta r})(1+3\nu_{r\theta})}$$

$$C_4 = \frac{(a/b)^3 - (a/b)^{\lambda}}{(b/a)^{\lambda} - (a/b)^{\lambda}} \frac{(1-\lambda\nu_{r\theta})(3+\nu_{\theta r})}{(-\lambda+\nu_{\theta r})(1+3\nu_{r\theta})}$$

Displacement

$$u = \frac{(1-\nu_{\theta r}\nu_{r\theta})\lambda^2\rho\omega^2 b^3}{(9-\lambda^2)\,E_\theta}\left\{C_5\left(\frac{r}{b}\right)^{\lambda} + C_6\left(\frac{r}{b}\right)^{-\lambda} - \left(\frac{r}{b}\right)^3\right\}$$

$$C_5 = \frac{(b/a)^{\lambda} - (a/b)^3}{(b/a)^{\lambda} - (a/b)^{\lambda}} \frac{(3+\nu_{\theta r})}{(\lambda+\nu_{\theta r})}$$

$$C_6 = \frac{(a/b)^3 - (a/b)^{\lambda}}{(b/a)^{\lambda} - (a/b)^{\lambda}} \frac{(3+\nu_{\theta r})}{(-\lambda+\nu_{\theta r})}$$

Figure 2.3

ISOTROPIC STRESS PROFILES

$\lambda=1,\ \nu=.3$

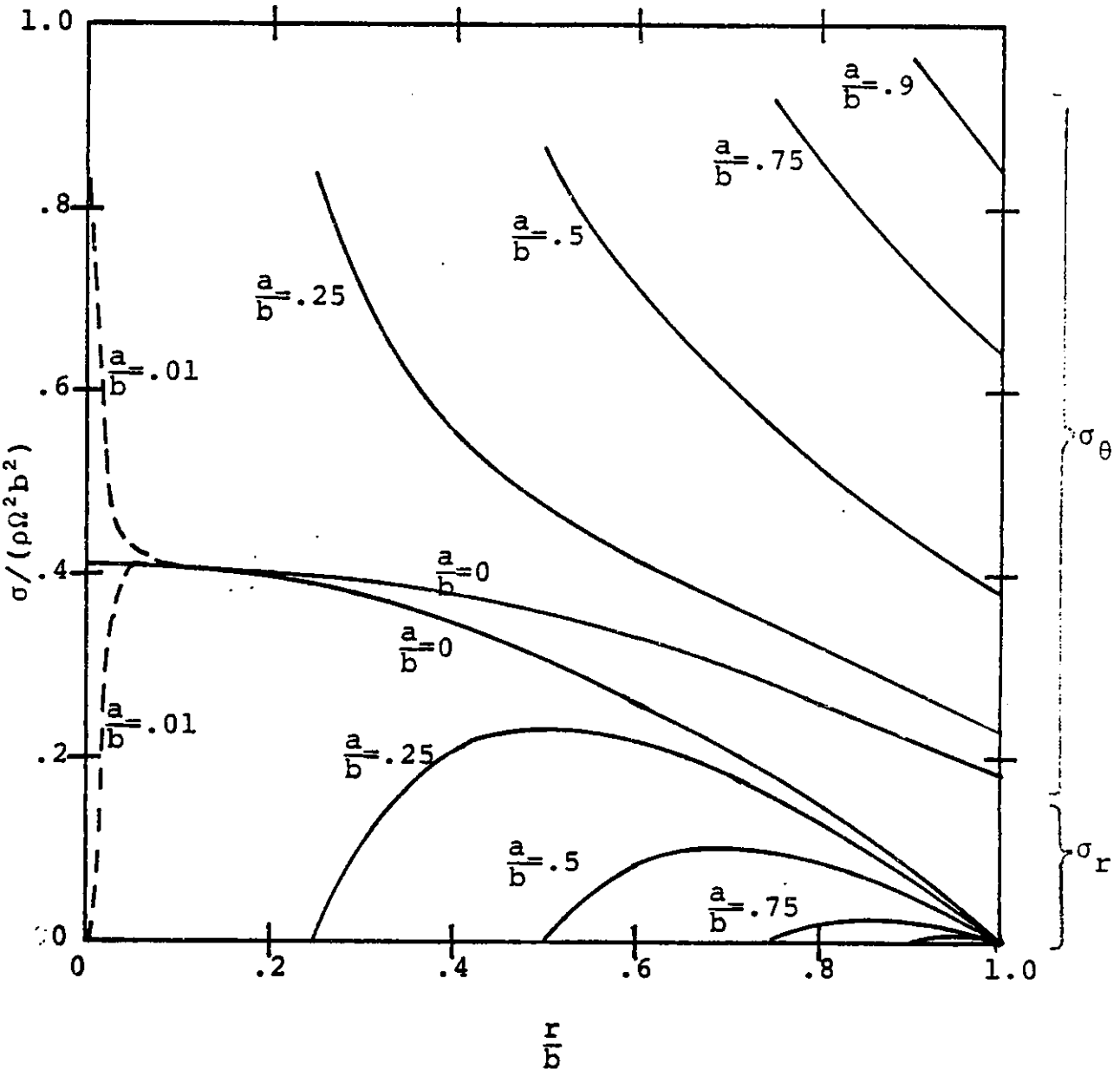

Figure 2.4

ANISOTROPIC STRESS PROFILE

-Circumferential-

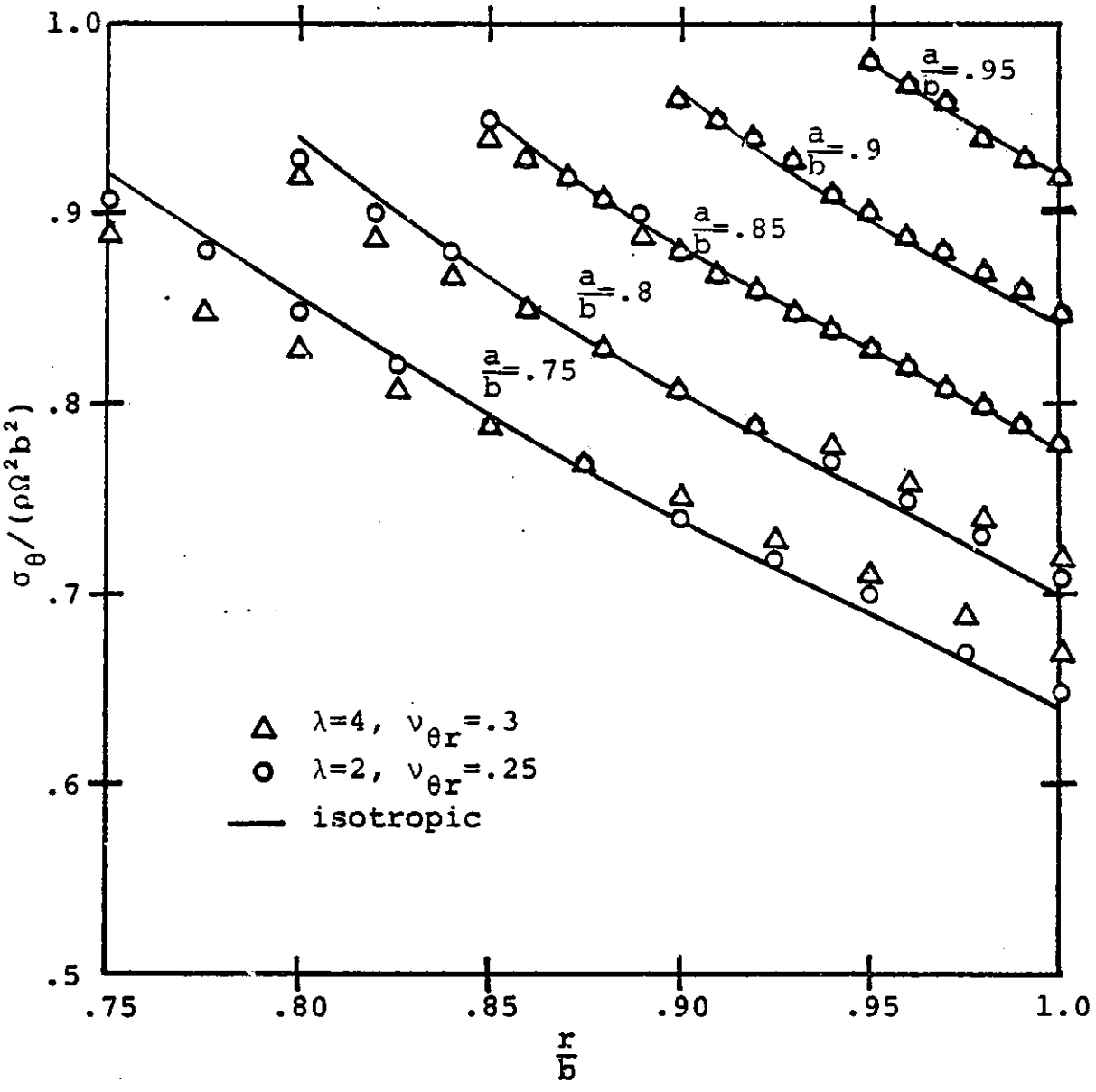

Figure 2.5

ANISOTROPIC STRESS PROFILE

-Radial-

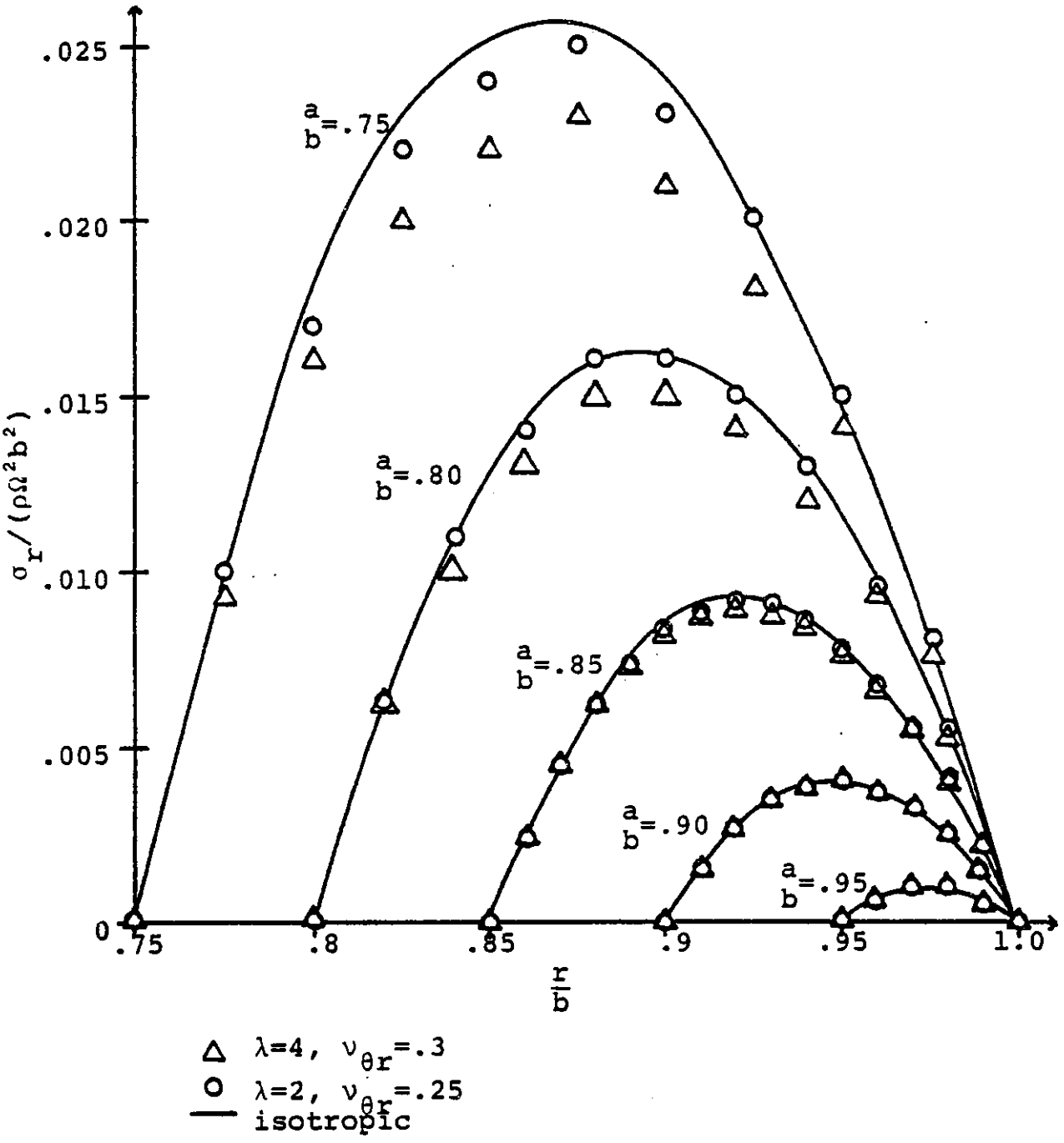

Figure 2.6

SHAPE FACTOR SUMMARY

on	Figure	Maximum Stress	J_p	K_s-Formula	K_s-Typical (ν=.3)
ress	a	$\frac{1}{2}\rho\Omega^2 r_o^2$	$\pi\rho h_o r_o^4$	1.0	.92
	b	$\frac{3+\nu}{8}\rho\Omega^2 b^2$	$\frac{1}{2}\pi\rho h b^4$	$\frac{2}{3+\nu}$	.61
k	c	$\frac{1}{4}(3+\nu+(\frac{a}{b})^2(1-\nu))\rho\Omega^2 b^2$	$\frac{1}{2}\pi\rho h(b^4-a^4)$	$\frac{1+(\frac{a}{b})^2}{3+\nu+(\frac{a}{b})^2(1-\nu)}$	$\frac{a}{b} \to 0$ .30 $\frac{a}{b} = .5$ .36 $\frac{a}{b} \doteq .9$ .47
	d	$\rho\Omega^2 b^2$	$2\pi\rho A_c b^3$	.50	.50
	e	$\frac{1}{2}\rho\Omega^2 b^2$	$\frac{1}{3}\rho A_c b^3$	.33	.33

ring must be in order to use uniaxial materials. The critical factor is the low transverse strength of these materials, typically between one and five percent of the longitudinal tensile strength. In order to insure that transverse stresses are unimportant, a configuration should be chosen which has a maximum radial stress sufficiently smaller than the maximum circumferential stress. The ratio of $\sigma_{r\ max}/\sigma_{\theta\ max}$ is plotted in figure 2.7 for a range of radius ratios and for both isotropic and anisotropic cases. They are all similar, and are well described by

$$\frac{\sigma_{r_{max}}}{\sigma_{\theta_{max}}} = .4\left(1 - \frac{a}{b}\right)^2 \quad \text{for } \frac{a}{b} > .5 \qquad (2.6)$$

Thus a radius ratio of .85 is sufficient to allow neglect of the radial stress. Thicker rings may be possible for some materials and for rings not stressed to their maximum potential.

Perhaps the most valuable information which can be obtained from the stress profiles is in contrasting the isotropic curve for a/b=0 with a/b=.01. By simply boring a tiny hole in the solid rotor the stress doubles near the center of the disk. Even if drilled holes are avoided, this stress concentration would still be present around any tiny voids or cracks which might exist near the center of the flywheel. The unstable nature of the stress near the center means that it is unlikely that a solid disk rotor could reliably sustain the high performance its shape factor of .6

Figure 2.7

STRESS RATIO FOR THIN RINGS

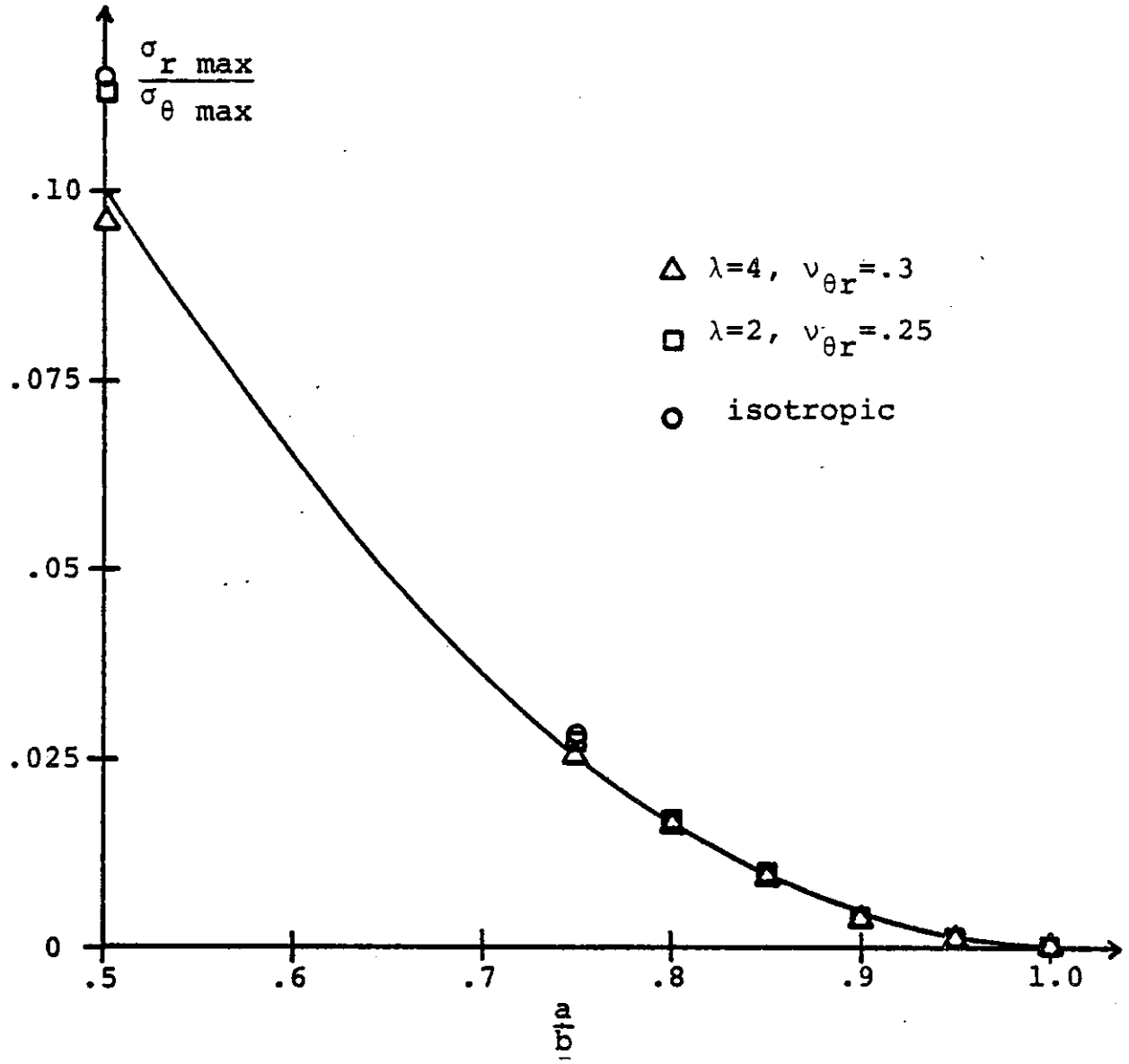

implies. Any real solid disk might be better modeled as a pierced disk with $a \to 0$, thus reducing its shape factor to .3.

From a comparison of the shape factors in figure 2.6, it would appear that the constant-stress configuration is by far the best. However, this concept, like the solid disk, relies heavily on material continuity at r=0, making it difficult to make secure attachment without inducing stress concentration. It is also difficult to fabricate the Stodolla design, as it must be formed as a single large unit. The disk designs, on the other hand, allow for the possibility of stacking several disks together. In the event of rotor failure, the ejected pieces would be smaller and only the affected disk would need replacing. The remaining brush configuration offers only a fair shape factor, and the volume required to house a given amount of energy storage with this design is about five times greater than for the disk.

From a practical standpoint, the constant stress disk is by no means the obvious selection. The thin ring design appears to have significant practical advantages despite its lower shape factor.

C. Materials

The primary effect of material selection is in the determination of two factors. The first is the ratio σ_{max}/ρ, which determines the specific energy, and the second is the cost per kilogram for the material, as this contributes to the

desirability of the system. Unfortunately, neither of these factors can be determined very accurately.

The maximum allowable stress in the rotor must be considerably derated from the ultimate tensile strength of the material. Because of the repeated stress cycling a flywheel must sustain, the strain must be kept well within the linear elastic range. In addition to the charge / discharge cycles, there is some variation of stress at the frequency of rotation which acts as another source for material fatigue.

Anisotropic materials are especially difficult to assign allowable stresses to, since existing fabrication technology is not well standardized. Different names are often assigned similar products by different manufacturers, and often the exact composition of the composite is not defined clearly. The wide spread in the performance of composite materials is illustrated by the time-to-failure plots generated at Lawrence Livermore Lab and shown in figure 2.8.

Similar confusion surrounds the cost of materials. In quoting a value for material cost, often it is the raw material cost which is given, while other times the price includes fabrication. Some estimates are current market prices, others are estimated cost for production quantities. Then of course there is the complication of inflation.

After reviewing material data from eight different sources, the values given by Garrett Corporation were selected as being the most representative [22]. The decision to use a single source is based on the fact that it is the relative

Figure 2.8
STRESS-RUPTURE TEST RESULTS

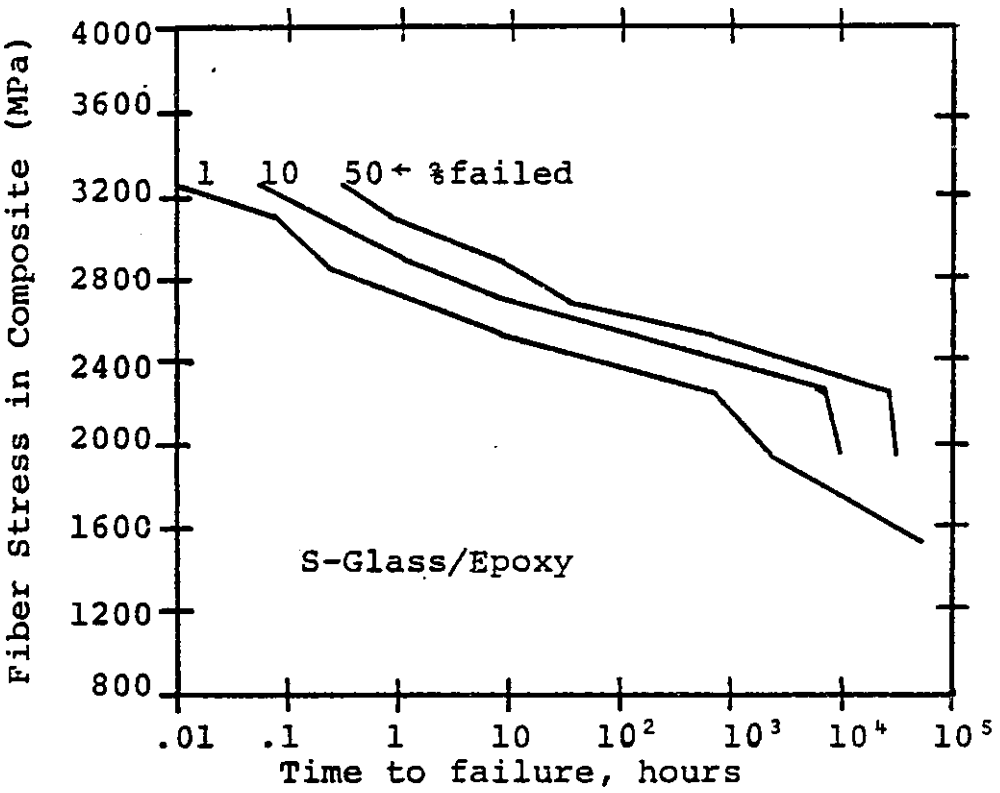

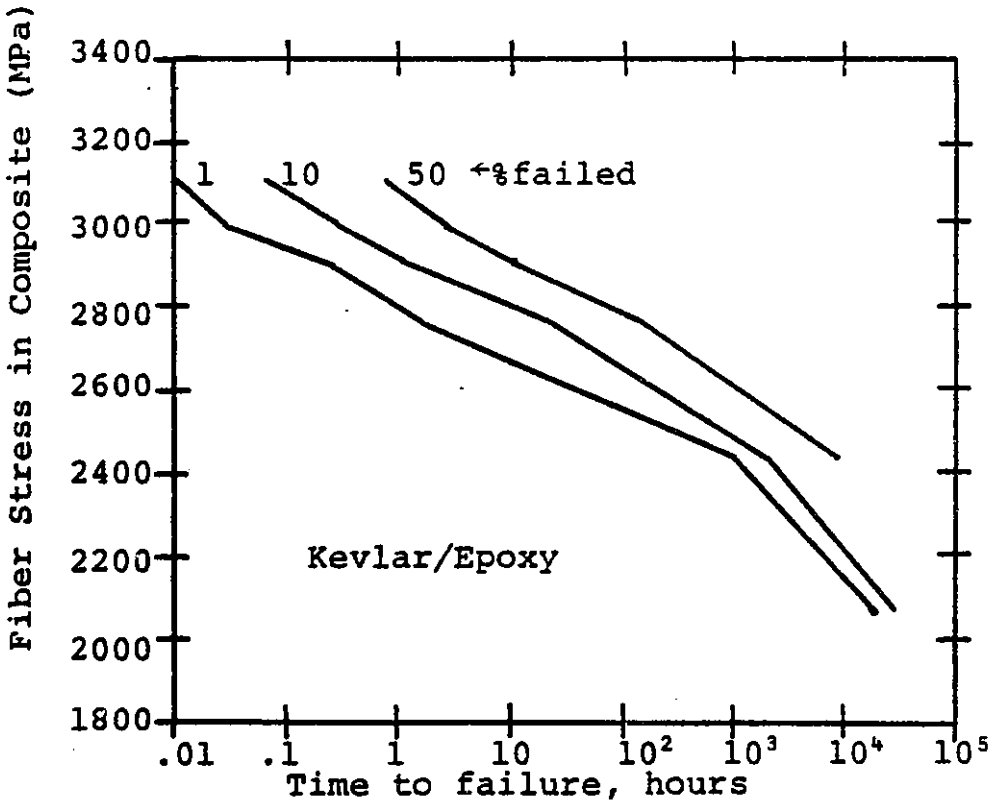

From: C. Chiao, "Long Term Performance of Fiber Composites," Proceedings of the 1975 Flywheel Technology Symposium.

performance of the various materials which is the most important factor. Also, Garrett has shown preeminence in the field of flywheel design, collecting a significant amount of experimental data. Their data for several interesting flywheel materials is shown in figure 2.9. Prices represent 1975 levels. Since then the anisotropic materials have shown only slight price increases, while steel has roughly followed the inflation rate.

The important point is that both of the glass-epoxy composites show performance comparable to the leading isotropic material, 4340 steel, even if the steel is allowed to have the unlikely realization of a unity shape factor. If a more reasonable factor of .5 is used for the steel then the anisotropic materials actually show a clear advantage.

In actual practice, it is not favorable to use a single thin ring of material, although such systems have been proposed [42]. The volume required to house such a design can become quite large. To overcome this problem, several rings can be nested one within another so that most of the swept area is filled with material. Such a concept, called the "multi-rim design" is shown in figure 2.10. By interconnecting the rings with flexible rubber, their stresses are effectively decoupled. The inner rings will not be exposed to as great a stress as the outer rings, however, and this leads to a reduction in the shape factor which must be considered.

Figure 2.9

Material	Density (kg/m^3)	Working Stress (MPa)	Raw Material Cost ($/kg)	$\frac{\sigma_{max}}{\rho}$ (kJ/kg)	Storage Rating at K_s=1 (kJ/$, WH/$)	Storage Rating at K_s=.5 (kJ/$, WH/$)
4340 Steel	7840	1000	2.00	130	65, 18	33, 9
E-glass/Epoxy	2200	800	2.60	360	-	69, 19
S-glass/Epoxy	2200	1200	4.20	540	-	64, 18
Kevlar-49/Epoxy	1400	1200	10.50	860	-	41, 11

From J. Friedericy and A. Raynard, "Garrett's Outlook on Vehicle Flywheels," Proceedings of the 1975 Flywheel Technology Symposium.

Figure 2.10

MULTI-RING ROTOR CONFIGURATION

-Cut-away view-

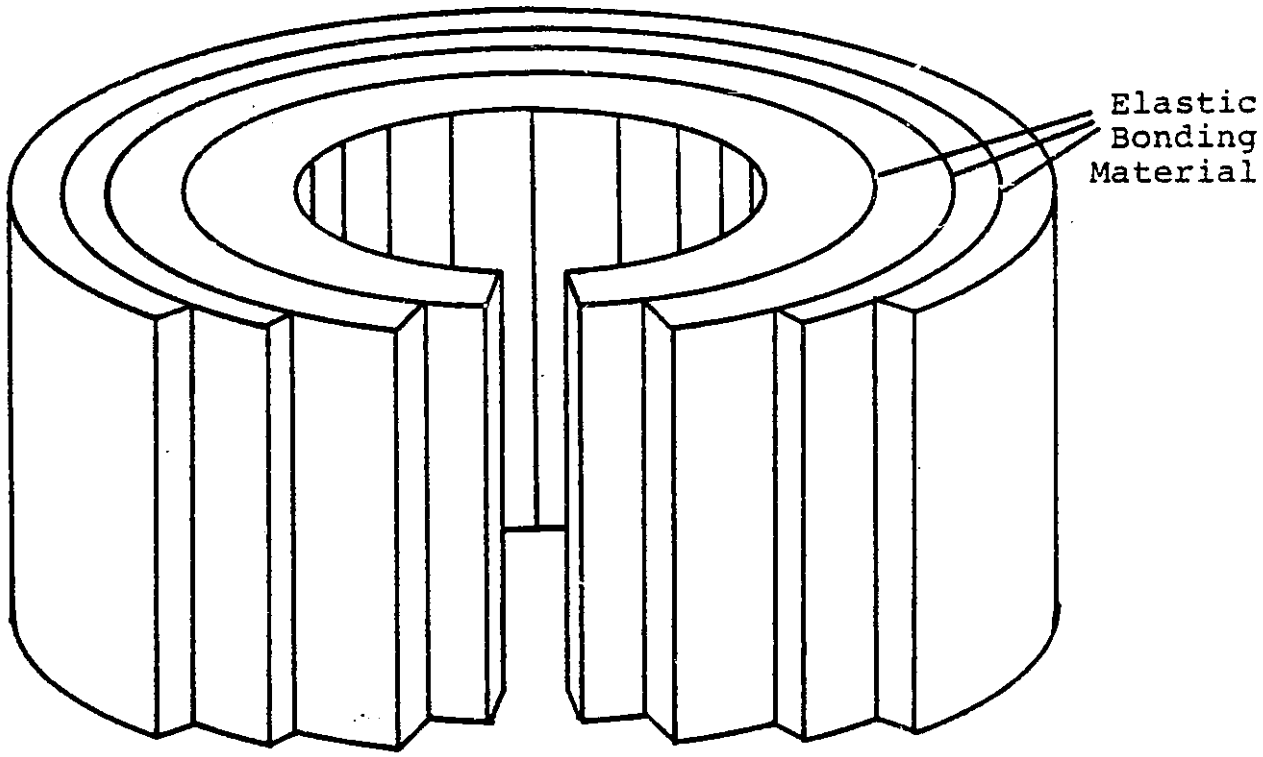

D. Multi-Rim, Multi-Material Rotors

If the outermost ring in a multi-rim design is thin, and acts as the limiting factor for the maximum rotational speed, then solving for the shape factor is straightforward if two assumptions are made:

1. The inter-ring elastomer is sufficiently elastic to retain the boundary conditions that $\sigma_r=0$ at the ring surfaces.
2. The radial extent of the inter-ring material can be neglected.

If all of the rings are of the same material, then the net effective shape factor is easily found. The rotational speed is limited by the outermost ring:

$$\Omega^2_{max} = \frac{\sigma_{max}}{\rho b^2} \qquad (2.7)$$

The mass and inertia expressions for the pierced disk are applicable, yielding a shape factor

$$K_s = \frac{1 + \left(\frac{a}{b}\right)^2}{4} \qquad (2.8)$$

Thus the effectiveness of the anisotropic materials appears to be cut nearly in half by this nesting arrangement.

The possibility exists, however, for making the

rings out of different materials. Investigation of this option is simplified if the circumferential stress at any radius can be given by

$$\sigma = \rho\Omega^2 r^2 \tag{2.9}$$

where the density may change for different radii. This expression is valid if many thin rings are used, and is approximately true for thicker rings. Notice that the combination Ωr is the velocity at the radius of interest. Thus

$$\frac{\sigma}{\rho} = v^2 \tag{2.10}$$

and the maximum velocity at which a thin ring of material can be run is an intrinsic property of the material. This value is often referred to as the material's "maximum tip speed". The specific energy relation can also be written, for thin rings only, as

$$E_s = \tfrac{1}{2} v^2 \tag{2.11}$$

This expression is valid for whatever the tip velocity might be, as long as it does not exceed the maximum allowed for the material.

A useful method for analyzing multi-material rotors is to envision the rotor as being composed of a very large number of thin rings. For a given rotational velocity, there is a maximum radius for each material

beyond which the tip speed exceeds its allowable limit. For smaller radius values, however, the specific energy decreases, and it might be more cost-effective to use a cheaper material where the stresses are not as high. Plotted in figure 2.11 is a graphical display of this situation. The storage cost plotted is for a thin ring at the velocity indicated. Since radius is proportional to velocity, the graph can be viewed with a cross-sectional perspective.

Clearly the layering of materials should be in the order of steel, E-glass, S-glass, and Kevlar. However, it is not necessary to use all of these materials. Shown in figure 2.12 are performance values for several combinations. To insure that failure will occur in the composites, rather than the steel, the steel is exposed to no more than 300 m/sec. Presumably silicon steel will be located on the innermost edge of the rotor. The minimum velocity for the rotor is thus selected as 200 m/sec, this being the highest velocity at which silicon steel can rotate. Single-material rotors are listed first, with the four-material rotor listed last. The 200 kJ/kg specific energy predicted is exactly what Garrett has obtained using the S-glass/Kevlar combination [69].

The arrangements marked by asterisks in the figure are all of comparable cost, and will be retained as likely candidates. Two combinations are especially enticing; the E-glass/S-glass combination is the lowest

Figure 2.11

STORAGE COSTS

-For Various Materials at Different Velocities-

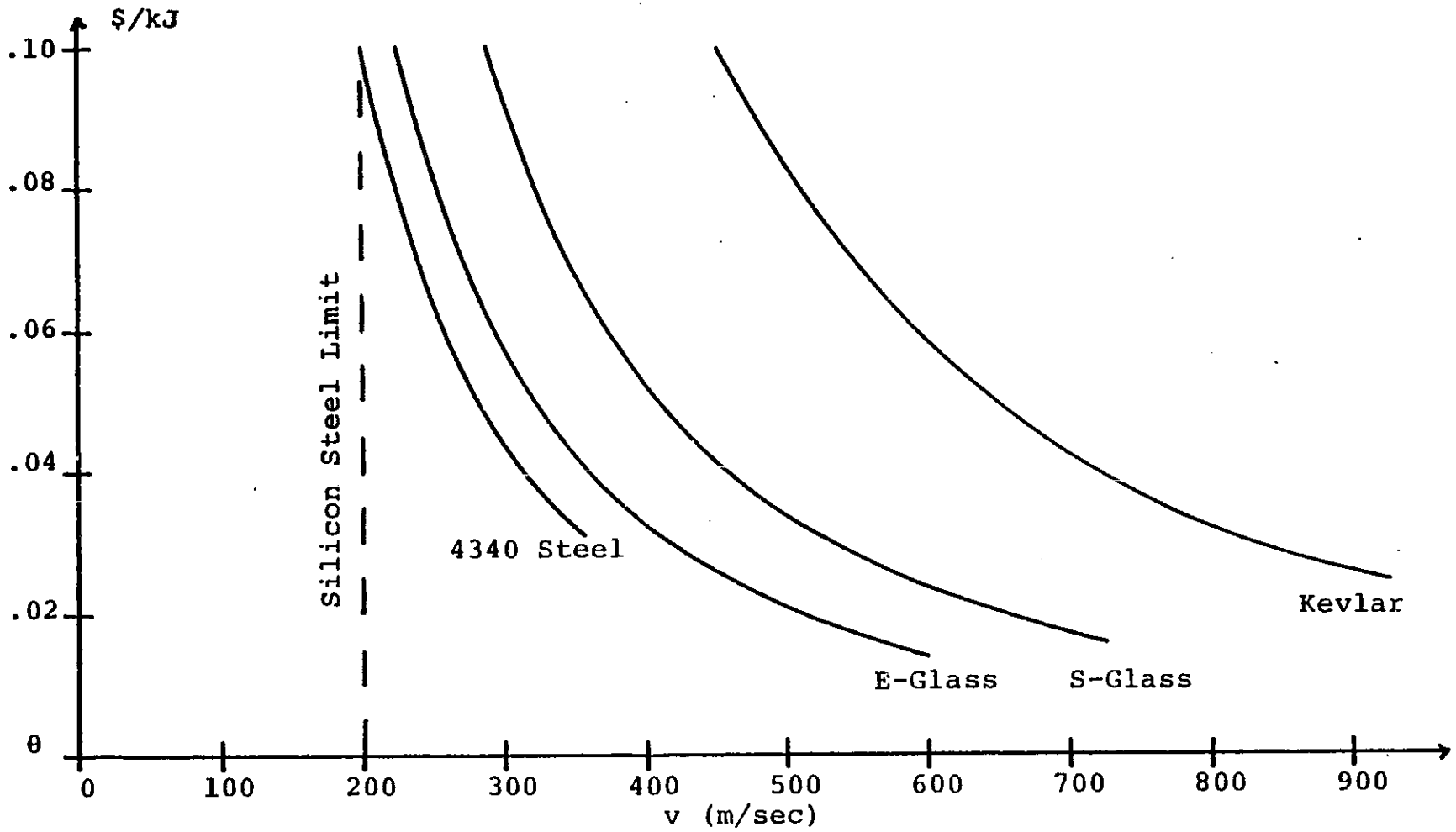

Figure 2.12

MATERIAL SELECTION
(BY RANGE)

200-300 (m/s)	300-600 (m/s)	600-725 (m/s)	725-925 (m/s)	E_s (KJ/Kg)	Storage Rating (KJ/$)	
E-glass	E-glass	-	-	100	38	*
S-glass	S-glass	S-glass	-	140	34	
4340	E-glass	-	-	80	34	
4340	S-glass	S-glass	-	120	33	
E-glass	E-glass	Kevlar	Kevlar	200	31	
S-glass	S-glass	S-glass	Kevlar	200	33	
E-glass	E-glass	S-glass	-	140	45	*
4340	E-glass	S-glass	-	120	42	*
4340	E-glass	Kevlar	Kevlar	170	30	
4340	S-glass	S-glass	Kevlar	170	33	
E-glass	E-glass	S-glass	Kevlar	200	38	*
4340	E-glass	S-glass	Kevlar	180	37	*

rotor cost option, but the very high specific energy of the E-glass/S-glass/ Kevlar arrangement may result in significantly lower containment and levitation expenses.

E. Gyroscopic Effects

Oscillatory motions of a flywheel other than the primary rotational mode are categorized together as "whirl modes". Rotor imbalance causes the center of mass to revolve about the axis of rotation at the same speed as the rotational velocity. This mode is referred to as "synchronous whirl", and although bothersome, rarely leads to instability. The interaction of centrifugal force and gyroscopic moment create other modes which occur at frequencies either above or below the rotational frequency, and are referred to as forward and retrograde whirl, respectively. Thomson, Younger, and Gordon of W.M. Brobeck and Associates have published a treatment of whirl modes for a pendulously supported flywheel [66]. These results can be specialized to the case of a flywheel with no shaft, as needed for the proposed multi-rim, magnetically- levitated design.

The levitation mechanism is presumed to have a translational spring stiffness k (in N/m) and a nutational stiffness K (in N/radian). In addition, define "a" as the ratio of the polar moment of rotational inertia to the inertia taken about the diameter of the

rotor:

$$a = \frac{J_p}{J_d} \tag{2.12}$$

The primary rotational velocity, Ω, is referred to as the spin, while the whirl is labeled ω. The resulting spin-whirl relationship is

$$\Omega = \frac{\omega^2 - \frac{K}{J_d}}{a\omega} \tag{2.13}$$

This is plotted, with the spin as the independent variable, in figure 2.13. Also shown is a typical spin-whirl relationship for a pendulously supported structure.

Mechanical hysteresis in the rotor materials can become quite large under whirl conditions. This energy is pumped into the whirl mode, causing potential instability, if two criteria are met:

1. The direction of the whirl is foward.
2. The spin frequency is greater than the whirl frequency.

When such a situation does exist, the system can only be stabilized if enough damping is present to remove the hysteresis power from the rotor.

Unfortunately, magnetic levitation has inherently very little damping [68]. It now becomes readily apparent why it is advantageous to eliminate the shaft

Figure 2.13

SPIN-WHIRL RELATIONSHIPS

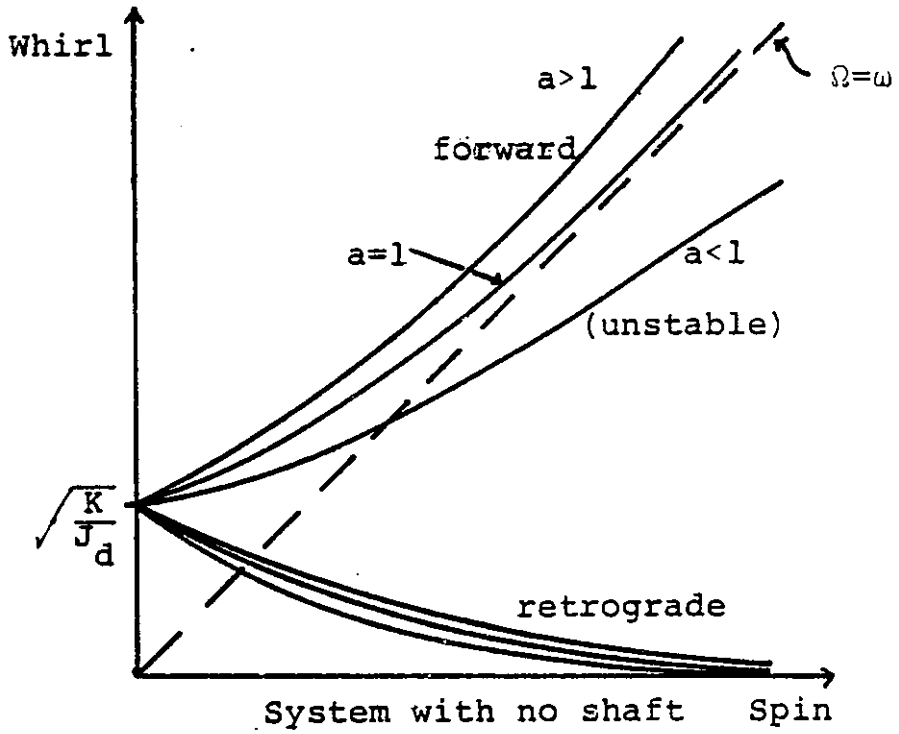

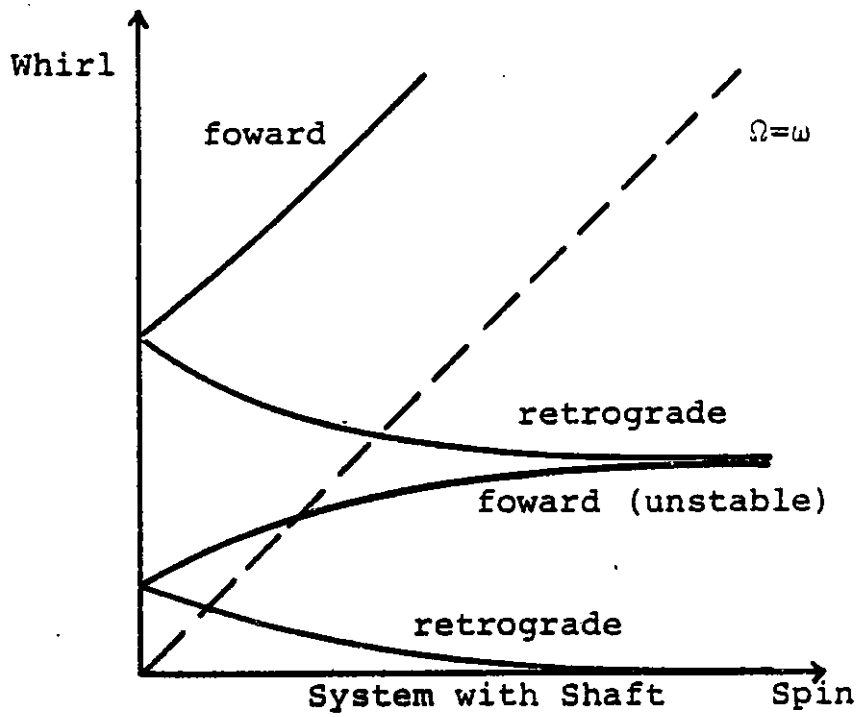

from the system. As seen in figure 2.13, when there is a shaft, there is always some spin beyond which $\Omega > \omega$. Thus extra damping mechanisms must be added to systems with shafts. With no shaft, stability is assured if a>1.

Requiring that J_p/J_d be greater than one places a restriction on the "aspect ratio" of the rotor:

$$\frac{J_p}{J_d} = \frac{\frac{1}{12} M(b^2-a^2)}{\frac{1}{12} M[3(b^2-a^2) + h^2]} > 1 \qquad (2.14)$$

or

$$\left(\frac{h}{b}\right)^2 < 3\left[1 - \left(\frac{a}{b}\right)^2\right] \qquad (2.15)$$

If a/b is small, then

$$h/b < 1.7 \qquad (2.16)$$

In order to minimize the surface area of the vacuum containment chamber, a ratio of h/b near 2 is best. Also high values of h/b provide more surface area on the inner edge of the rotor for levitation and propulsion. Thus h/b should be chosen near the top of the allowable range. A value of h/b = 1.5 will be taken as an initial design criteria, leaving an adequate margin of safety.

Another gyroscopic effect which must be considered is the imposed precession resulting from the earth's rotation. The flywheel is presumed to be located with its axis vertical. Thus there is an angle between its

axis of rotation and the earth's axis of rotation which is equal to 90 degrees minus the latitude. A body spinning at speed Ω, under imposed precession $\dot{\phi}$ induces a moment on its supports, m_o, which is orthogonal to both the spin and precession axes [2]. Let the angle between spin and precession axes be θ.

$$m_o = \{J_p[\Omega + \dot{\phi}\cos(\theta)] - J_d\,\dot{\phi}\cos(\theta)\}\dot{\phi}\sin(\theta) \quad (2.17)$$

For a flywheel, $\Omega >> \dot{\phi}$, so

$$m_o = J_p\,\Omega\,\dot{\phi}\sin(\theta) \quad (2.18)$$

On earth, $\phi = 7.27 \cdot 10^{-5}$ rad/sec. Usually this effect can be neglected, but because of the low stiffness of magnetic levitation and the narrowness of the magnetic gap, this factor can have a small but noticeable effect.

III. MAGNETIC LEVITATION

The possibility of using magnetic levitation for support of a flywheel requires investigation of several factors. If permanent magnets are to be used, then their magnetic and mechanical properties are important considerations. These topics are presented in the first section, much of which is taken from the work of J. Gould [26] and R. Parker [56]. The quantity of permanent magnets required is of concern both from a cost-feasibility standpoint and from a space-allocation point of view. Similar concerns apply to the amount of silicon iron needed for the system. As there is a limited amount of available area on the inner surface of the rotor, the area needed to provide adequate lift must be determined.

Evaluation of the force in a magnetic system excited by currents introduced through an electrical terminal pair is a subject treated by most textbooks on electromechanics. The possibility of using permanent magnets to provide the force is avoided by claiming that the permanent magnet could always be replaced by a current coil. The details of this equivalent circuit technique are rarely specified, and when they are it is without theoretical justification. The alternative method is to determine the force using the actual fields by application of the Maxwell stress tensor. This approach has a strong theoretical basis, but lacks the simple form the energy method provides.

As no satisfactory model for predicting forces in permanent-magnet systems could be found, a framework was derived which yielded results both convenient to apply and theoretically sound. This derivation covers sections B through D. The remaining sections are the application of this method to expressing the relationships governing permanent-magnet levitation in a unique and particularly useful form. The techniques and formulas derived in this chapter are applied to a sample bearing designed at MIT's Lincoln Lab in appendix 1. Comparison of the results to experimentally obtained data shows excellent agreement.

A. Permanent Magnets

There are a variety of ways in which the relationship of fields to their sources can be represented. All are equally correct, but often one representation is more convenient than the others. Organized, macroscopic flow of charge is generally introduced as a current density in Ampere's law. This is useful because such flows are generally related linerarly to the macroscopic imposed electric field through the point form of Ohm's law. Motion on an atomic scale, by contrast, is generally smoothed out and introduced as either a constitutive law for the bulk material or as sheet sources on planes of material discontinuity.

Permanent magnets have properties which do not lend themselves to simple representation in either the source or

constitutive-law representation. B versus H constitutive relations for several important permanent magnet materials are shown in figure 3.1. The level of induction remaining after application and removal of a saturation H-field is called the remanent induction, labeled B_r. The applied field required to drive the induction to zero is the coercive force, H_c. Because magnets generally operate in the second quadrant, these graphs are referred to as demagnetization curves. An extension to primarily source-type descriptions is illustrated by figure 3.2 for the case of uniform magnetization.

As shown in figure 3.3, once a magnet has assumed a certain operating point on its B-H curve, any perturbations in its environment cause the operating point to move in a small hysteresis loop somewhat removed from the original curve. This loop is well approximated by the dotted line shown. So long as perturbations from the operating point are small, they can be assumed to occur along this line of operation. The intersection of this line with the axis will be called the permanent induction, and labeled B_o. The slope of this line, which is the same as for the saturation part of the magnetization curve, is labeled μ_m and referred to as the recoil permeability. Notice that for $SmCo_5$ and ceramic V the line of operation will coincide with the magnetization curve for the majority of second-quadrant operation.

Magnets described by a linear line-of-operation curve assume the workable constitutive relation

Figure 3.1

CONSTITUTIVE RELATIONS FOR MAGNETS

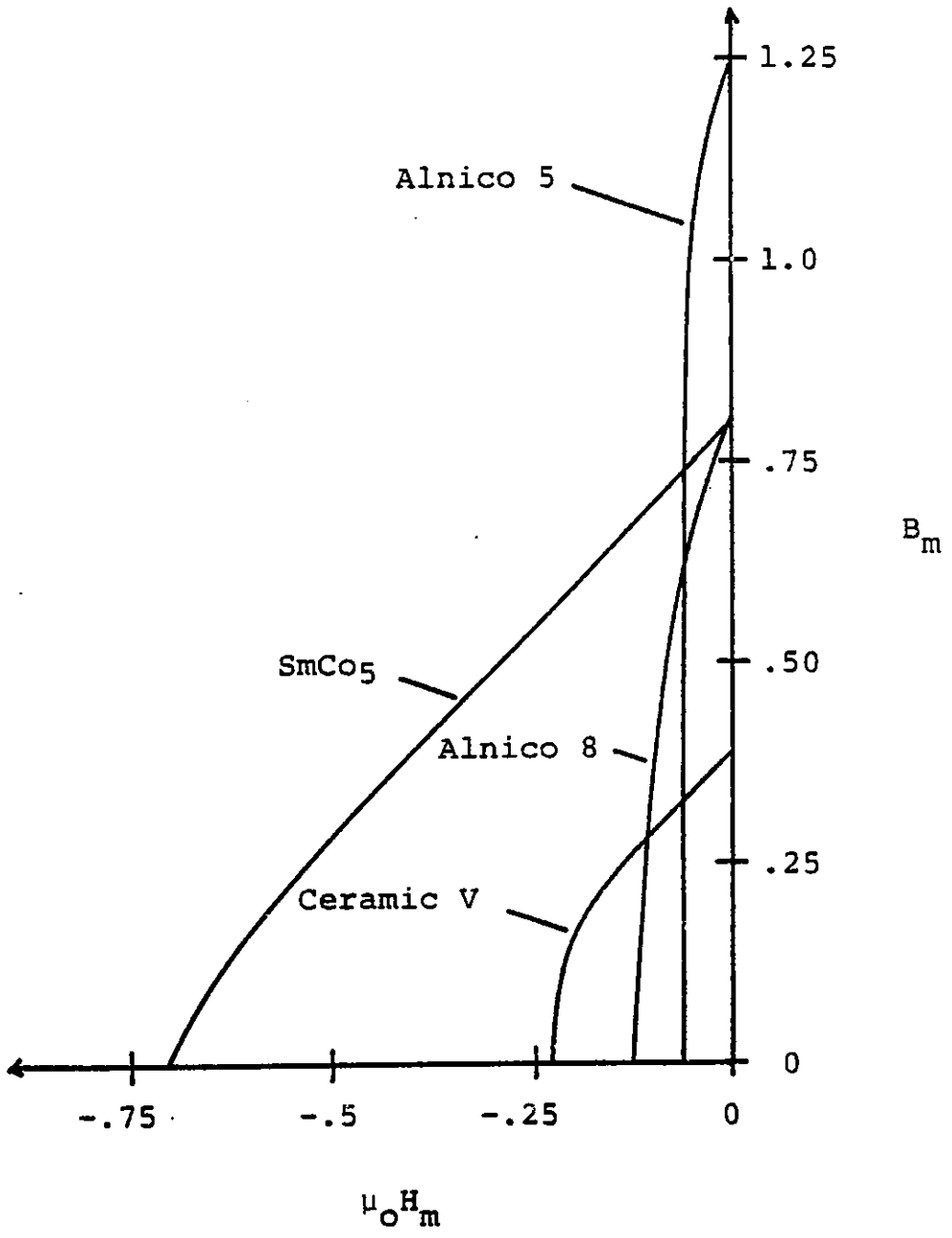

Figure 3.2

SOURCE REPRESENTATIONS FOR MAGNETS

All magnetizable materials can be described by a constitutive relation $\bar{B}=\mu_0(\bar{H}+\bar{M})$, where in general M is not constant. If $\bar{M}$ is uniform and known, then the magnet can be replaced by equivalent sources:

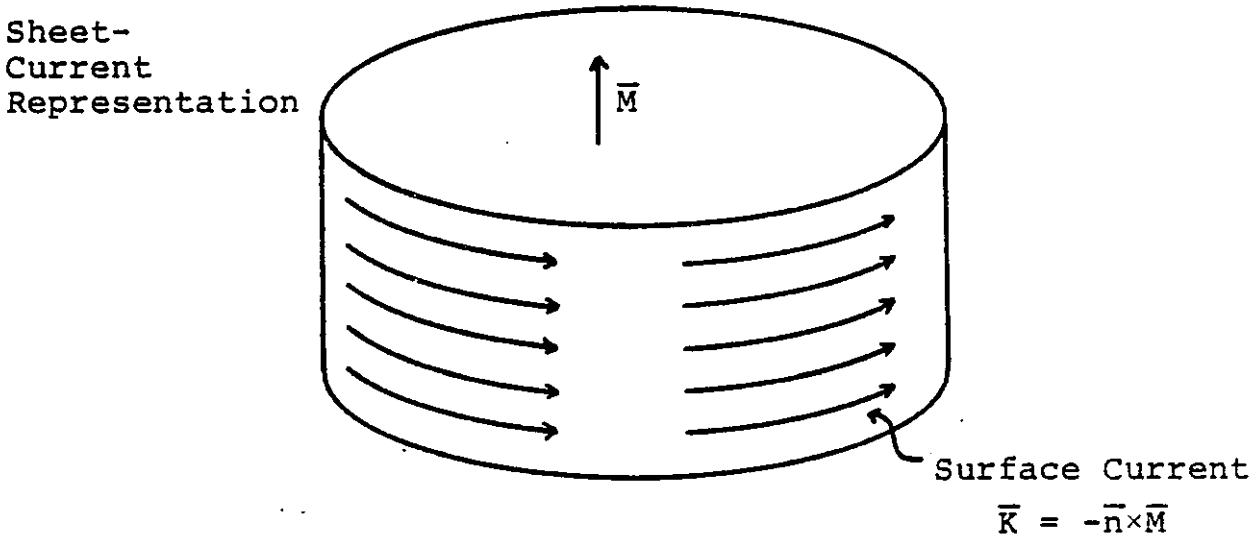

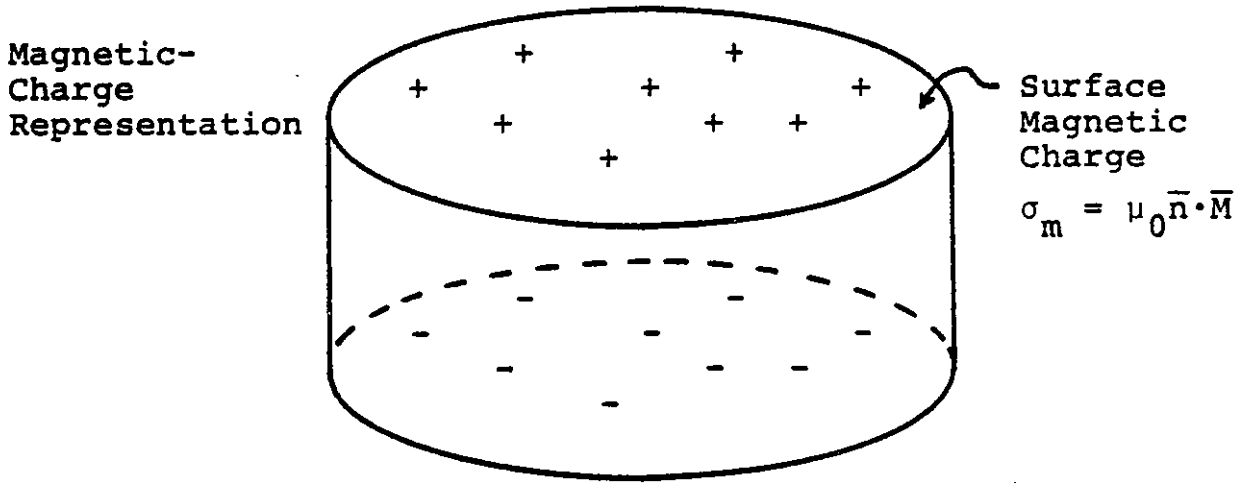

Figure 3.3

RECOIL OPERATION OF PERMANENT MAGNETS

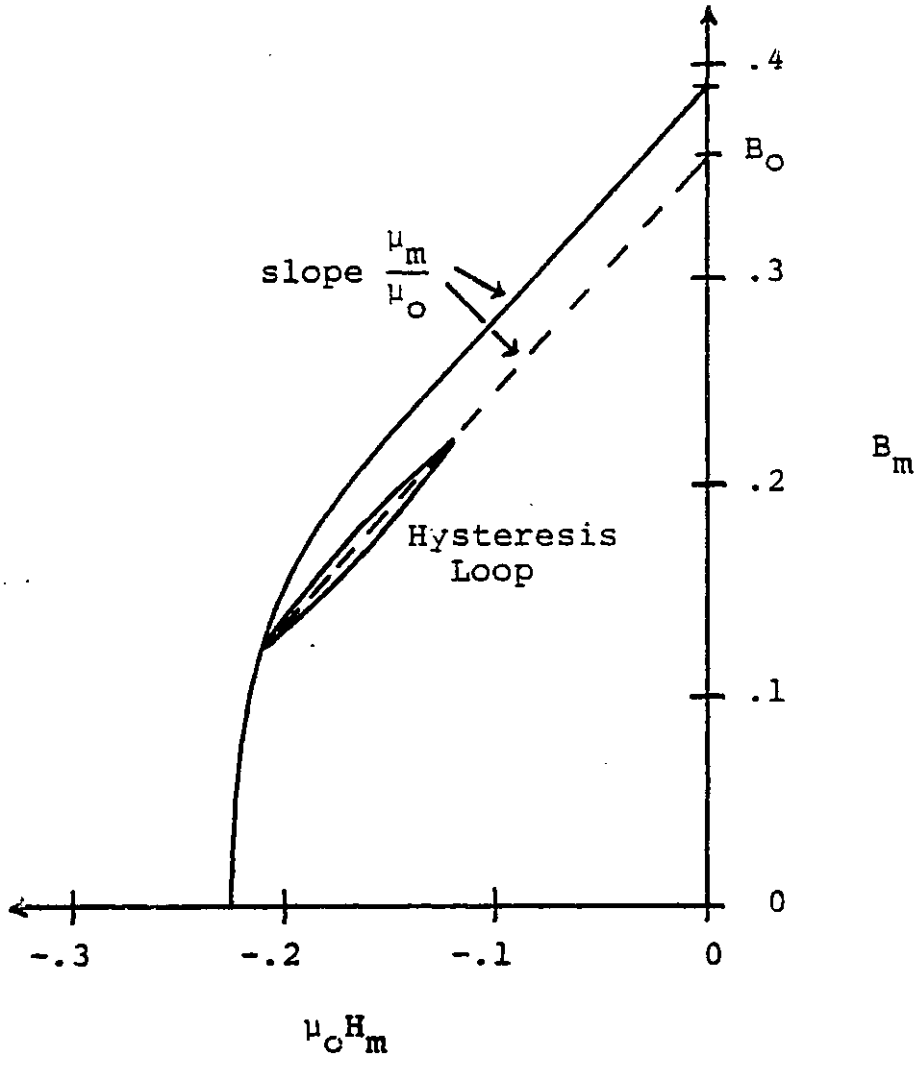

$$B_m = B_o + \mu_m H_m \qquad (3.1)$$

This form allows several important simplifications, and will be used for the remainder of this presentation.

Several properties besides the permanent magnetization are important parameters in magnet design. Among these are mechanical properties and temperature effects. These factors will be investigated for the two materials of greatest interest, ceramics and rare-earth cobalt compounds.

Ceramic magnets come in several forms, but the compound $BaO \cdot 6Fe_2O_3$ generally gives the best results. When heated to over 1000°C, this material forms a ferrimagnetic hexagonal crystal with uniaxial magnetic properties. An isotropic magnet can be produced by grinding the material to a powder, pressing, and heating; but the resulting permanent magnetization is expectedly lower. The firing process causes a marked shrinkage in ceramic materials, making it difficult to control final dimensions to better than 2%. Critical surfaces can be ground to tolerance after cooling.

Ceramic magnets are much more susceptible to temperature variations than other materials. The magnetization decreases with increasing temperature at the rate of .2%/°C. In the anisotropic material, the coercive force decreases in magnitude with decreasing temperature, reducing to about 90% of its nominal value at -20°C. Ceramics are limited on the high end of temperature range by their low Curie point at 450°C.

As long as temperatures are not extreme, ceramics do have some distinct advantages. Primarily, they are the lowest-cost magnets available. But also they are free from problems of oxidation and corrosion, and have very high resistivity. If operated in their linear B-H regime, ceramic magnets will retain over 99.9% of their magnetization for many years.

Several rare earths form hexagonal compounds with cobalt. The most effective magnetic combination is with samarium in the proportions $SmCo_5$. The forming process is similar to ceramics except that an argon-helium atmosphere is required due to the highly reactive nature of the elements. $SmCo_5$ has the distinct advantage of having a very high remanent magnetization coupled with very high coercivity.

Some of $SmCo_5$'s disadvantages are high cost and susceptability to corrosion. Corrosion can severely limit the long-term stability of the magnetization. The material is also very brittle with low tensile strength. Another problem arises from the need for extremely high fields for magnetizing the material. Often the magnets must be shipped and installed pre-magnetized. A table listing important parameters for a variety of magnetic materials is shown in figure 3.4.

B. Circuit Analog with Permanent Magnets

The controlling field laws for quasi-static magnetic systems (where charge relaxation times and wave propogation times are much shorter than times of interest) have as

Figure 3.4

PERMANENT MAGNET PARAMETERS

Material	B_r (T)	$\mu_o H_c$ (T)	$(BH)_m$ (kJ)	At $(BH)_{max}$ B_o (T)	p	$\frac{\mu_m}{\mu_o}$	Magnetizing Field (kA/m)	Temp. Coef. (%/°C)	Max. Temp. (°C)	Density ρ (kg/m^3)	Approx. cost ($/kg)	Energy cost (kJ/$)
$SmCo_5$	.8	.70	120	.80	1	1.05	6000	-.04	200	8200	110	1.1
Ceramic V	.39	.24	26	.39	2	1.05	1000	-.19	350	4900	4	6.5
Alnico 5	1.26	.07	43	1.15	17	3.1	160	-.02	500	7400	44	1.0
Alnico 8	.90	.16	44	.85	8	2.4	400	-.02	500	7400	50	.9

Parameters from J. Gould, "Permanent Magnets," Proceedings of IEEE (November 1978)

Pricing from F. Dempsey, Arnold Engineering Company

integral forms:

$$\oint_C \bar{H}\cdot d\bar{l} = \int_S \bar{J}\cdot d\bar{S}$$
$$\oint_S \bar{B}\cdot d\bar{S} = 0 \qquad (3.2)$$

The controlling field laws for circuits are the integral forms of Kirchoff's laws:

$$\oint_C \bar{E}\cdot d\bar{l} = 0$$
$$\text{Circuit Laws} \qquad (3.3)$$
$$\oint_S \bar{J}\cdot d\bar{S} = 0$$

In either situation, the contour integrals can be divided into n segments:

$$\sum_{i=1}^{n} \int_{C_i} \bar{H}\cdot d\bar{l} = \int_S \bar{J}\cdot d\bar{S} \qquad \sum_{i=1}^{n} \int_{C_i} \bar{E}\cdot d\bar{l} = 0 \qquad (3.4)$$

The terms on the left are recognized as being the magnetic and electric potential differences across each segment. Identify

$$\Psi_i = -\int_{C_i} \bar{H}\cdot d\bar{l} \qquad V_i = -\int_{C_i} \bar{E}\cdot d\bar{l} \qquad (3.5)$$

so that

$$\sum_{i=1}^{n} \Psi_i = -\int_S \bar{J}\cdot d\bar{S} \qquad \sum_{i=1}^{n} V_i = 0 \qquad (3.6)$$

Let one of the segments in Ampere's law be selected so that it makes a negligible contribution to the sum. That is, select a portion of the contour where H is finite and let the length of

that segment approach zero. Label this special segment as contour C_n. Then

$$\lim_{|C_n|\to 0} \sum_{i=1}^{n} \int_{C_i} \bar{H}\cdot d\bar{l} = \sum_{i=1}^{n-1} \int_{C_i} \bar{H}\cdot d\bar{l} \qquad (3.7)$$

or

$$\sum_{i=1}^{n-1} \Psi_i + \int_S \bar{J}\cdot d\bar{S} = 0 \qquad (3.8)$$

If the current integral is itself identified as a magnetic potential difference, then it may be thought of as occupying the small gap in the contour created by the removal of the integral over C_n. Thus

$$\Psi_n = \int_S \bar{J}\cdot d\bar{S} \qquad (3.9)$$

and the loop equations become analogous:

$$\sum_{i=1}^{n} \Psi_i = 0 \qquad \sum_{i=1}^{n} V_i = 0 \qquad (3.10)$$

In a similar fashion, the closed surfaces can be divided into n regions:

$$\oint_S \bar{B}\cdot d\bar{S} = \sum_{i=1}^{n} \int_{S_i} \bar{B}\cdot d\bar{S} \qquad \oint_{S_i} \bar{J}\cdot d\bar{S} = \sum_{i=1}^{n} \int_{S_i} \bar{J}\cdot d\bar{S} \qquad (3.11)$$

By making the identifications

$$\int_{S_i} \bar{B}\cdot d\bar{S} = \Phi_i \qquad \int_{S_i} \bar{J}\cdot d\bar{S} = I_i \qquad (3.12)$$

the usual continuity equations result:

$$\sum_{i=1}^{n} \Phi_i = 0 \qquad \sum_{i=1}^{n} I_i = 0 \qquad (3.13)$$

The analogy that $\Psi\to V$, $\Phi\to I$ where Ψ represents both field drops

as well as NI current drives has long been established. The important point is that no volume in space is associated with the current drives in the circuit analogy picture.

If equipotential surfaces can be identified in the magnetic system, then a magnetic Ohm's law follows,

$$\Psi_i = \Phi_i R$$

where

$$\Psi_i = -\int_a^b \bar{H}\cdot d\bar{l} \text{ is constant over two "terminal" surfaces} \qquad (3.15)$$
$$\Phi_i = -\int_s \bar{B}\cdot d\bar{S} \text{ is constant between the two terminal surfaces}$$

R is the reluctance, which is analogous to resistance, and is defined entirely by Ohm's magnetic equation, above.

Based on these results, permanent magnets with constitutive relations given by equation 3.1 have circuit-analog terminal relations given by

$$\Psi_m = \Psi_o + \Phi_m R_m \qquad (3.16)$$

which corresponds to a voltage source in series with a resistance. Expressions for the reluctance and Ψ_o values associated with three important geometries are given in figure 3.5.

C. Field Energy from Terminal Quantities

The basis for electromagnetic energy storage of any kind

Figure 3.5

CIRCUIT-ANALOG VALUES FOR IMPORTANT GEOMETRIES

Ψ_0 values apply only for magnetic materials

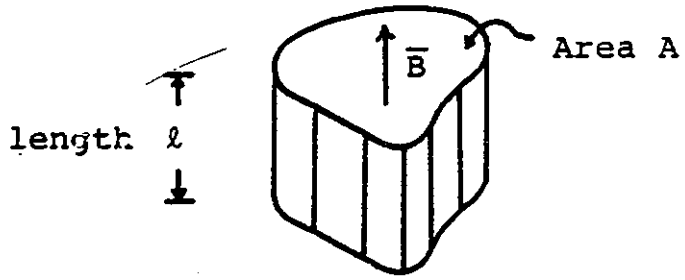

Uniform Cross-Section
Longitudinal Field

$$R = \frac{\ell}{\mu A}$$

$$\Psi_0 = \frac{B_0 \ell}{\mu}$$

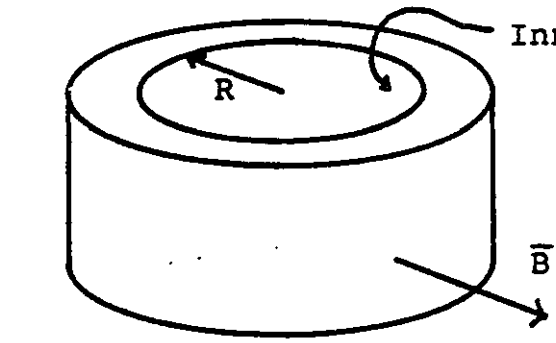

Axisymmetric
Radial Field

$$R = \frac{R \ln\left(\frac{R+\ell}{R}\right)}{\mu A}$$

$$\Psi_0 = \frac{B_0 R \ln\left(\frac{R+\ell}{R}\right)}{\mu} \quad ; B_0 \text{ referenced to inner surface}$$

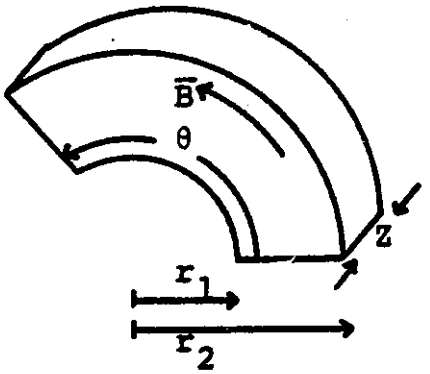

Azimuthal Field

$$R = \frac{\theta}{\mu z \ln(r_2/r_1)}$$

$$\Psi_0 = \frac{B_0 r_1 \theta}{\mu} \quad ; B_0 \text{ referenced to inner surface}$$

is the potential energy of charges in an electric field. Any increase in energy requires the movement of charge. Because moving charges interact through magnetic fields, those fields are evidence of the energy associated with that charge, and it is permissible to think of the energy as actually being stored in the fields themselves. The following derivation begins by following Melcher [47], but extends to incorporate magnetic terminal quantities.

Let a system of charges evolve in a frame of fixed material parameters for a time δt. The increase in the stored energy is

$$\delta W = -\bar{f}\cdot d\bar{x} = -q\bar{E}\cdot d\bar{x} \tag{3.17}$$

Consider only an element of volume δV, which may contain charges of both species. Let the positive charge be represented by $q_+=\rho_+\delta V$ and the negative charge by $q_-=-\rho_-\delta V$. In the time interval δt, the positive charges move a distance $v_+\delta t$ while the negative charges move $v_-\delta t$.

$$\delta W = -(\rho_+\bar{v}_+ - \rho_-\bar{v}_-)\cdot\bar{E}\ \delta V\delta t \tag{3.18}$$

But $\bar{J}=\rho_+v_+-\rho_-v_-$ so

$$\delta W = -\bar{J}\cdot\bar{E}\ \delta V\delta t \tag{3.19}$$

The energy increase for all space is thus

$$\delta W = -\int_{\text{All Space}} \bar{J}\cdot\bar{E}\ dV\ \delta t \tag{3.20}$$

By taking Ampere's and Faraday's laws in point form and dotting them with $\overline{E}$ and $\overline{H}$, respectively, then subtracting one from the other:

$$\nabla\cdot(\overline{E}\times\overline{H}) = \overline{J}\cdot\overline{E} + \overline{H}\cdot\partial\overline{B}/\partial t \tag{3.21}$$

where the displacement-current term is neglected for magnetic systems. Integrating this expression over all space yields

$$\int_{\text{All Space}} \overline{J}\cdot\overline{E}\ dV = -\int_{\text{All Space}} \overline{H}\cdot\frac{\partial\overline{B}}{\partial t}\ dV \tag{3.22}$$

Thus the energy increase can be written as

$$\delta W = \int_{\text{All Space}} \overline{H}\cdot\frac{\partial\overline{B}}{\partial t}\ dV\ \delta t = \int_{\text{All Space}} \overline{H}\cdot\delta\overline{B} \tag{3.23}$$

Divide all space into n convenient regions:

$$\delta W = \sum_{i=1}^{n} \delta W_i \qquad \delta W_i = \int_{V_i} \overline{H}\cdot\delta\overline{B}\ dV \tag{3.24}$$

Consider now only those regions which contain no free current. This does not exclude regions where the effect of currents is incorporated through a constitutive relation. Then $\nabla\times H=0$ and $\overline{H}=-\nabla\psi$ so that

$$\delta W_i = -\int_{V_i} \nabla\psi\cdot\delta\overline{B}\ dV \tag{3.25}$$

The vector identity $\nabla\psi\cdot\delta\overline{B}=\nabla\cdot\psi\delta\overline{B}-\psi\nabla\cdot\delta\overline{B}$ is combined with the fact that $\nabla\cdot\delta\overline{B}=0$ to yield:

$$\delta W_i = -\int_{V_i} \nabla\cdot\psi\delta\overline{B}\ dV \tag{3.26}$$

Utilizing the divergence theorem,

$$\delta W_i = -\oint_{S_i} \psi \delta \bar{B} \cdot d\bar{S} \tag{3.27}$$

For cases of interest, there are only two non-zero contributions to this integral, occurring at two equipotential magnetic "terminals", across which all of the flux flows. Label these terminals "a" and "b". Then

$$\delta W_i = -\psi_a \int_{S_a} \delta \bar{B} \cdot d\bar{S} - \psi_b \int_{S_b} \delta \bar{B} \cdot d\bar{S} \tag{3.28}$$

If the flux enters at terminal "a", and $\Psi_i = \psi_a - \psi_b$:

$$\delta W_i = \Psi_i \delta \Phi_i \tag{3.29}$$

It is important to remember that only energy stored in reversible electrical forces has been included in this derivation. This includes effects of both magnetization and externally injected currents. What has not been included in equation 3.29 is energy "stored" in the fields contained in regions where current actually flows. For many magnetic systems interesting for magnetic levitation, however, this contribution is negligible. The total field energy thus included becomes

$$\delta W = \sum_{i=1}^{n} \Psi_i \delta \Phi_i \tag{3.30}$$

If there were no other mechanisms for energy storage, the energy for all space would be

$$\delta W_{TOT} = \sum_{i=1}^{n} \psi_i \delta \Phi_i = 0 \tag{3.31}$$

which is a necessary result of conservation of energy. Such a situation has no practical applications, however, and other factors, especially mechanical interactions, need to be added to the description.

D. Energy Method for Force

Under consideration is a magnetic system which can be divided into two regions with these restrictions:

1. Neither region contains any free currents.
2. The two regions are joined by equipotential magnetic terminals, such that all of the flux which transfers out of one region enters the other across these terminals.
3. Any magnetic field energy not contained in regions 1 or 2 is negligible.

Initially, the flux circuit is broken, and the ends are brought out and treated as terminals for the entire system. Such a situation is portrayed in figure 3.6. As described, all of the magnetic fields associated with the system are contained in one of the two regions. Thus the field energy due to electrical forces is given by equation 3.30,

$$\delta W = \Psi_T \delta\Phi_T = \Psi_1 \delta\Phi + \Psi_2 \delta\Phi \qquad (3.32)$$

Additional energy can be extracted in mechanical form from region 2. Thus the total field energy in the system is given by

Figure 3.6

MAGNETIC SYSTEM PORTRAYAL FOR FORCE DETERMINATION

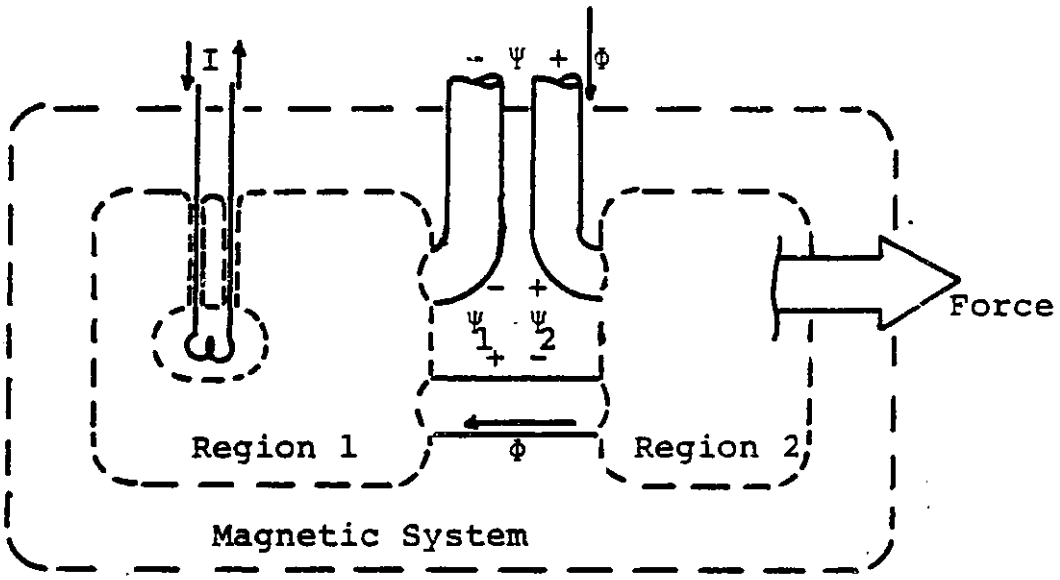

$$\delta W_f = \Psi_T \delta\Phi - \bar{f}\cdot d\bar{r} \tag{3.33}$$

where $d\bar{r}$ represents an incremental change in LaGrangian position coordinates. Selecting as independent variables Φ and $\bar{r}$, the increment in the field energy can be expanded by partial derivatives as

$$\delta W_f = \left.\frac{\partial W_f}{\partial \Phi}\right|_{\bar{r}} \delta\Phi + \left.\frac{\partial W_f}{\partial \bar{r}}\right|_{\Phi} \delta\bar{r} \tag{3.34}$$

Subtracting equation 3.34 from 3.33 and realizing that $\delta\Phi$ and $\delta\bar{r}$ are arbitrary yield

$$\Psi_T = \left.\frac{\partial W_f}{\partial \Phi}\right|_{\bar{r}} \qquad f_i = \left.\frac{\partial W_f}{\partial x_i}\right|_{\Phi} \tag{3.35}$$

so that if an expression for the total field energy in the variables Φ and $\bar{r}$ is known, then the force can be determined.

As is generally done to find such an expression, the system is assumed to be conservative [47,76]. All dissipative elements are considered to be located outside of the system. In a conservative system, W_f is a function of state, and any path may be taken in achieving that state. Consider, then, the following process of assembling the magnetic system of figure 3.6:

1. The flux terminals are left open circuited, so that Φ=0. Under these conditions system 2 can be mechanically assembled with all forces equal to zero.

2. The two flux terminals are gradually brought together until the flux circuit is completed.

This process is represented by the following integral form of equation 3.33.

$$\int \delta W_f = \int_o^{\Phi} \Psi_T \delta\Phi' - \int_{\infty}^{\bar{r}} \bar{f}\cdot d\bar{r} \qquad (3.36)$$

Letting W_o be the field energy in the system prior to assembly, then

$$W_f = W_o + \int_o^{\Phi} \Psi_T \delta\Phi' \qquad (3.37)$$

With this formula, the field energy of various segments of a magnetic system can be represented in terms of their circuit-analog quantities:

1. For a passive linear segment; $W_f = \frac{1}{2}\Phi^2 R$
2. For a permanent magnet; $W_f = \frac{1}{2}\Phi^2 R_m + \Psi_o \Phi$ (3.38)
3. For a current coil; $W_f = 0$

No field energy is associated with a current coil in a magnetic circuit context because it is presumed to occupy no volume in space, as pointed out in section 3B.

The general expression for the force becomes

$$f_i = -\frac{\partial}{\partial x_i}\int_o^{\Phi} \Psi_T \delta\Phi \Big|_{\Phi \text{ constant}} \qquad (3.39)$$

Breaking up the integral into the two regions,

$$f_i = - \frac{\partial}{\partial x_i} \int_o^{\Phi} \Psi_1 \delta\Phi' \Big|_{\Phi \text{ const.}} - \frac{\partial}{\partial x_i} \int_o^{\Phi} \Psi_2 \delta\Phi' \Big|_{\Phi \text{ const.}} \tag{3.40}$$

But the integral in region 1 is independent of $\bar{r}$, for constant flux, so that

$$f_i = - \frac{\partial}{\partial x_i} \int_o^{\Phi} \Psi_2 \delta\Phi' \Big|_{\Phi \text{ constant}} \tag{3.41}$$

In general, region 2 is selected to encompass the magnetic gap, since that is where the force originates in most systems. For a gap with reluctance R_g,

$$f_i = - \frac{\partial}{\partial x_i} (\tfrac{1}{2} \Phi_g^2 R_g) \Big|_{\Phi_g \text{ constant}} = -\tfrac{1}{2} \Phi_g^2 \frac{\partial R_g}{\partial x_i} \tag{3.42}$$

This amazingly simple and useful result is in agreement with the intuitive notion that the force at the gap should depend only on gap parameters, and that it shouldn't matter how the flux got there. This is reinforced by agreement with the concept of the Maxwell stress tensor, which states that the force is entirely due to the fields surrounding the movable object. To illustrate the usefulness of this result a problem has been worked using this and more conventional approaches in appendix 2.

E. Circuit Representations for Levitation Systems

The force has been shown to depend on the flux traversing

the gap. This flux must come from magnets or currents, so a practical topology is to direct as much of the available flux as possible from the sources to the gap. A circuit which accomplishes this, with allowance for flux-reducing mechanisms, is shown in figure 3.7a. Locating the leakage losses closer to the magnet and the iron losses closer to the gap has been found to be slightly more accurate than the reversed situation, though the difference is small. The current source has been located in series with the magnet for convenience.

As indicated in section 3A, many magnets have good linear circuit equivalents. Furthermore, the iron loss can be replaced by a reluctance, though the value of the reluctance will be a function of flux and may require iteration. The resulting linear circuit is shown in figure 3.7b, along with expressions for the gap and magnet flux.

For a well-designed system, $R_\ell >> R_m$ and $R_i << R_g$. Furthermore, it is often the flux through R_g which is of interest. Consequently, it can be helpful to use the simplified circuit shown in figure 3.8a. All of the flux losses are grouped into the modified source, which represents the Thevenin equivalent seen by R_g. Similarly, if the magnet is under scrutiny, the circuit of figure 3.8b may be useful.

In order to apply these circuit analogs to actual magnetic systems, methods for determining the various circuit element values are required. The reluctance of the gap can be complicated to predict for practical levitation schemes, so

Figure 3.7

a. NON-LINERAR CIRCUIT ANALOG
For Permanent-Magnet Levitation Systems

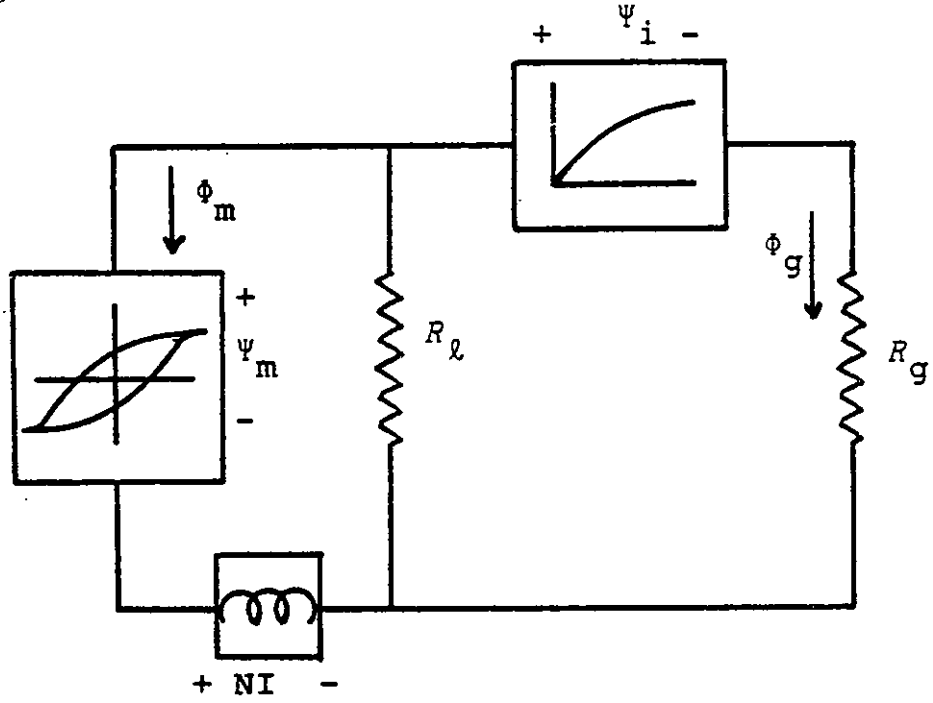

b. LINEARIZED CIRCUIT

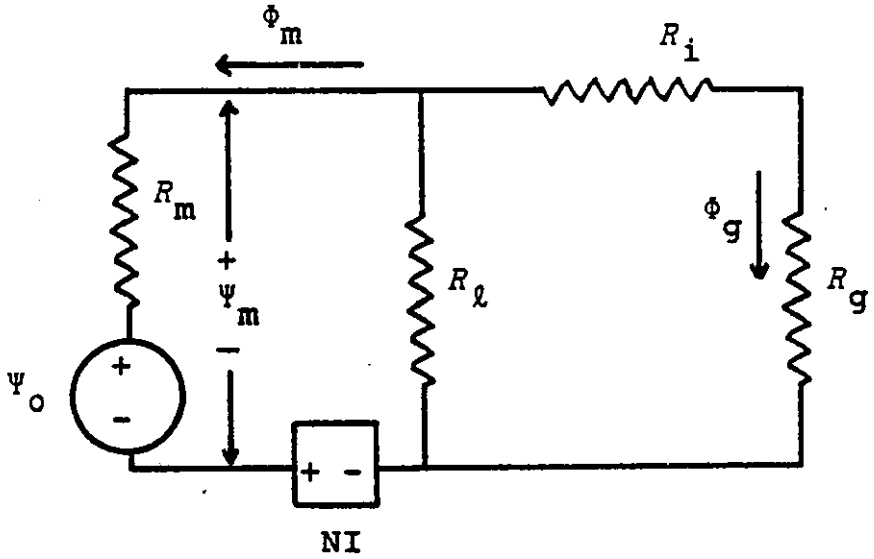

Figure 3.8

SIMPLIFIED LINEAR CIRCUITS

a. Effective-Source Form

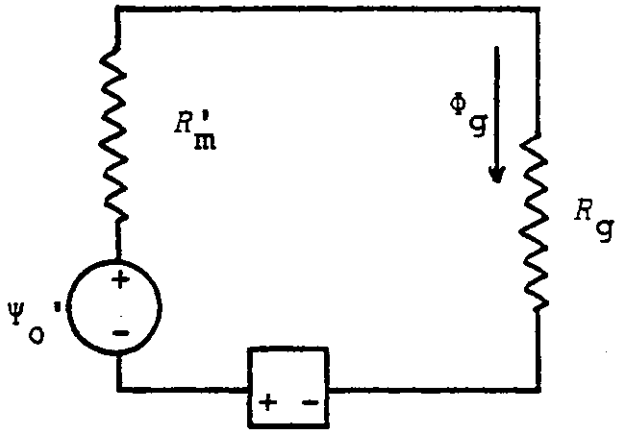

$$R'_m = R_m \| R_\ell + R_i \qquad N' = \frac{R_\ell}{R_\ell + R_m} N$$

$$\Psi'_o = \frac{R_\ell}{R_\ell + R_m} \Psi_o$$

b. Equivalent-Load Form

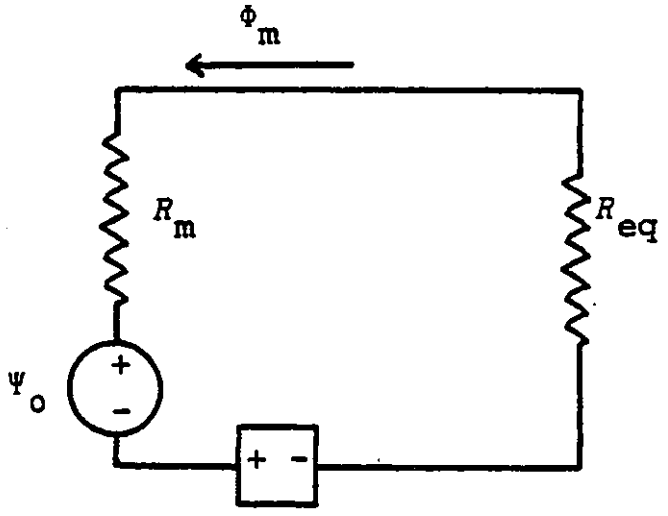

$$R_{eq} = R_\ell \| (R_i + R_g)$$

this matter is deferred until the next section. Values for the remaining elements can be estimated with adequate accuracy using fairly simple techniques.

Any real system has a large number of interacting iron-loss and flux-leakage paths. Successive reductions of the circuit show that to first order in the influence of the losses, most circuits can be reduced to the standard form. This same result can be realized in a much simpler fashion through two steps:

1. Ignoring iron losses, find the net reluctance through leakage paths in going from one pole of the magnet to the other.
2. Ignoring leakage, find the total reluctance of the iron in going from one pole to the other.

Estimating leakage reluctance can be performed with reasonable accuracy using a graphical arcs-and-lines technique. The essence of the method is to sketch approximate leakage flux paths using sections of circles and parallel lines. The reluctance of each section can be calculated using one of the expressions shown in figure 3.5. The necessary series and parallel combinations can then be taken to yield the total leakage reluctance.

Calculating the iron reluctance is complicated by the non-linear behavior of the material. Shown in figure 3.9 are some typical B-H curves for silicon steels [19]. For the task at hand, the plot of effective permeability is the most useful form. The flux density can be first estimated by assuming no

Figure 3.9

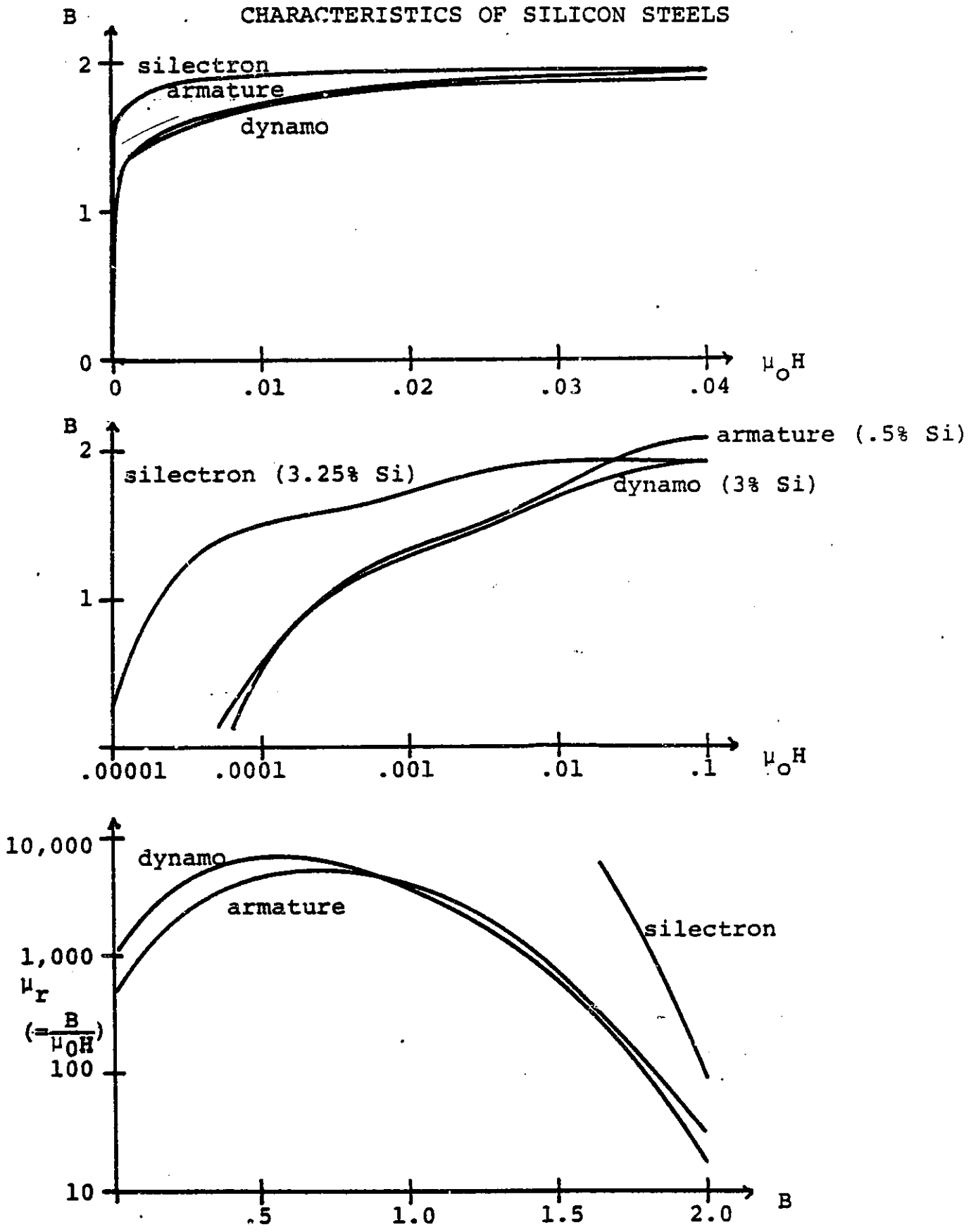

Data From Allegheny Ludlum Steel Corporation

iron or leakage losses in the system. The flux density is then found for each section in the flux path, the appropriate permeability determined, and the reluctance calculated as for a linear material. If introducing this reluctance significantly alters the total flux, then the process can be repeated using the new flux value. More than one repetition exceeds the accuracy of the model. Example calculations of both leakage and iron reluctance for a sample magnetic system are given in appendix 1.

The reluctance of the magnet can be evaluated through the use of equations 3.14 and 3.15 or from figure 3.5. In similar fashion, Ψ_o can be found if the value of B_o is known. But the value of B_o generally depends upon the magnet's operating point. This operating point, plus other useful information about the magnet, can be determined from the circuit-analog parameters.

The operating point for a magnet is determined just as for non-linear circuit elements by drawing a load line on the magnet's B-H curve and noting the point of intersection. The magnitude of the ratio of B to $\mu_o H$ at the operating point is referred to as the "permeance ratio" [56]. The operating point can be placed in the linear portion of the B-H curve (as is often desirable) by specifying a minimum value for the permeance ratio.

The B-H curve can be mapped into a Φ_m-Ψ_m curve through the relations

$$\Phi_m = B_m A_m \qquad \Psi_m = H_m \ell_m \tag{3.43}$$

if the magnet is uniformly magnetized. The permeance ratio can thus be expressed as

$$P = -\frac{B_m}{\mu_o H_m} = -\frac{\Phi_m}{\Psi_m}\frac{\ell_m}{\mu_o A_m} = -\frac{\Phi_m}{\Psi_m}\frac{\mu_m}{\mu_o} R_m \tag{3.44}$$

But the relationship of Ψ_m to Φ_m is independently established by the remainder of the magnetic circuit. For the case of no current,

$$\Psi_m = -\Phi_m R_{eq} \tag{3.45}$$

where R_{eq} is the equivalent reluctance seen by the terminals of the magnet, as defined in figure 3.8. Therefore, the permeance ratio can be written as

$$P = \frac{\mu_m}{\mu_o}\frac{R_m}{R_{eq}} \tag{3.46}$$

Since $\mu_m \approx \mu_o$, define a modified permeance ratio for convenience as

$$p = R_m / R_{eq} \tag{3.47}$$

Based on this parameter, some useful relationships are possible:

$$B_m = \frac{p}{p+1} B_o \qquad H_m = \frac{-1}{p+1}\frac{B_o}{\mu_m} \tag{3.48}$$

Another useful value is the volume of the magnet in terms of circuit and magnet parameters,

$$\frac{\Psi_o^2}{R_m} = \frac{B_o^2 \ell_m^2}{\mu_m^2} \cdot \frac{\mu_m A_m}{\ell_m} = \frac{B_o^2}{\mu_m} V_m \tag{3.49}$$

or also,

$$\Psi_m \Phi_m = H_m \ell_m \cdot B_m A_m = B_m H_m \cdot V_m \tag{3.50}$$

F. Force

From the results of section 3D, the force is given by

$$f_i = -\tfrac{1}{2} \Phi_g^2 \frac{\partial R_g}{\partial x_i} \tag{3.51}$$

The gap flux can be determined using the modified circuit parameters given in figure 3.8a,

$$f_i = -\frac{\tfrac{1}{2}(\Psi_o' + N'I)^2}{(R_m' + R_g)^2} \frac{\partial R_g}{\partial x_i} \tag{3.52}$$

By simple analogy, the torque on the system can be found to be

$$\tau_i = \frac{\tfrac{1}{2}(\Psi_o' + N'I)^2}{(R_m' + R_g)^2} \frac{\partial R_g}{\partial x_i} \tag{3.53}$$

Only systems with no steady-state current will be considered further.

There are several ways of expressing the force which emphasize its dependence on various aspects of the magnetic

circuit. Of primary concern are how the different parameters influence the relationship of the force to the cost-generating aspects of the system. There are three main cost-producing elements in magnetic bearing systems:

1. The volume of magnet required.
2. The area of magnetic gap required.
3. The volume of iron required.

The first two have very explicit solutions in terms of the circuit parameters. The iron considerations will require several approximations.

For consideration of the volume of magnets required, the flux is first given in terms of the equivalent reluctance seen by the magnet:

$$\Phi_m = \frac{-\Psi_o}{(R_m + R_{eq})} \tag{3.54}$$

so that

$$\Phi_g = \frac{\Psi_o \quad R_{eq}}{(R_m + R_{eq})\ (R_i + R_g)} \tag{3.55}$$

Thus the force is

$$f_i = \frac{-\frac{1}{2}\ \Psi_o^2\ R_{eq}^2}{(R_m + R_{eq})^2 (R_i + R_g)^2} \frac{\partial R_g}{\partial x_i} \tag{3.56}$$

The volume is extracted by creating the term Ψ_o^2/R_m, as discussed in the last section.

$$\frac{f_i}{V_m} = - \frac{B_o^2}{2\mu_m} \frac{R_m R_{eq}^2}{(R_m + R_{eq})^2 (R_i + R_g)^2} \frac{\partial R_g}{\partial x_i} \tag{3.57}$$

R_m can be expressed in terms of R_{eq} by using the modified permeance ratio, p;

$$\frac{f_i}{V_m} = - \frac{B_o^2}{2\mu_m} \frac{p}{(p+1)^2} \frac{R_{eq}}{(R_i+R_g)^2} \frac{\partial R_g}{\partial x_i} \tag{3.58}$$

The gap derivative can be expressed as a normalized, dimensionless number by introducing the distance g as being the shortest path-length across any one gap. This value is limited to some minimum value by mechanical tolerances.

$$\frac{f_i}{V_m} = - \frac{B_o^2}{2\mu_m g} \frac{p}{(p+1)^2} \frac{R_{eq} R_g}{(R_i+R_g)^2} \left\{ \frac{g}{R_g} \frac{\partial R_g}{\partial x_i} \right\} \tag{3.59}$$

The term with R_{eq} and R_g can be written as

$$\frac{R_{eq} R_g}{(R_i+R_g)^2} = \frac{1}{(1 + R_i/R_\ell + R_g/R_\ell)(1 + R_i/R_g)} \tag{3.60}$$

which for small losses can be approximated as

$$\frac{R_{eq} R_g}{(R_i+R_g)^2} \simeq 1 - R_i/R_g - R_g/R_\ell \tag{3.61}$$

This factor, which represents the effect of the losses on the force, will be labeled as the efficiency, η. Although R_g appears in this expression, it is only in a perturbational capacity, and it will be assumed that η is a constant for a

given system. Then the force can be written

$$\frac{f_i}{V_m} = -\eta \frac{B_o^2}{2\mu_m g} \frac{p}{(p+1)^2} \left\{ \frac{g}{R_g} \frac{\partial R_g}{\partial x_i} \right\} \tag{3.62}$$

Thus the entire effect of the shape of the gap is included in a single dimensionless term. Label this term as f_{1i};

$$f_{1i} = \left\{ - \frac{g}{R_g} \frac{\partial R_g}{x_i} \right\} \tag{3.63}$$

For levitation systems it is the force in the z direction (that of gravity) which is most often of interest, so the absence of a direction subscript will imply the z-direction. Therefore,

$$\frac{f_z}{V_m} = \eta \frac{B_o^2}{2\mu_m g} \frac{p}{(p+1)^2} f_1 \tag{3.64}$$

There are limits to how large f_1 can be for a given levitation scheme, and under no circumstances can its value exceed unity.

The portion of this expression,

$$\frac{B_o^2}{\mu_m} \frac{p}{(p+1)^2}$$

is also equal to $B_m H_m$. This is significant in that there is a certain operating point for each magnet type for which $(BH)_m$ reaches a maximum. In some cases, the maximum BH product is limited by other factors as well. For example, in ceramic the operating point is usually set near p=2 due to its

tendency to demagnetize at low temperatures, even though this does not correspond to its highest BH energy product. The maximum BH products for various magnet materials were given in figure 3.4. The force equation thus assumes its final volume-dependent form:

$$\frac{f_i}{V_m} = \eta \frac{(BH)_m}{2g} f_{1i} \tag{3.65}$$

For considerations of gap area, it is first necessary to examine the nature of the magnetic gap. In general, the gap spacing can vary significantly over the area of the gap. In fact this is necessary in practical gap structures. The value "g" has already been introduced as the narrowest gap dimension. Let A_g represent the total cross-sectional area of a particular gap. Then the reluctance of that gap can be written as

$$R_g = \frac{C\,g}{\mu_o A_g} \tag{3.66}$$

The combination Cg thus represents an effective width for the gap, and A_g is considered to be a constant with respect to displacements.

Levitation schemes require there be two gaps in series. In general they will have the same areas, A_g, and effective gaps, Cg. This can present a considerable source of confusion. For consistency, all gap parameters will refer to one gap only (C, g, A_g, B_g), while circuit-analog values (B_g,

Ψ_g, Φ_g) will refer to two gaps in series. The total gap reluctance thus becomes

$$R_g = \frac{2\ Cg}{\mu_o A_g} \tag{3.67}$$

Under these conditions, the gap derivative is

$$\frac{\partial R_g}{\partial x_i} = \frac{2}{\mu_o A_g} \frac{\partial (Cg)}{\partial x_i} \tag{3.68}$$

and the gap-influence factor for magnet-volume analysis can be written

$$f_{1i} = \left\{ - \frac{g}{R_g} \frac{\partial R_g}{\partial x_i} \right\} = \left\{ - \frac{1}{C} \frac{\partial (Cg)}{\partial x_i} \right\} \tag{3.69}$$

To evaluate the effect of gap area, start with the fundamental force equation:

$$f_i = -\tfrac{1}{2}\ \Phi_g^2 \frac{\partial R_g}{\partial x_i} \tag{3.70}$$

The flux is expressed in terms of the potential across the gap,

$$f_i = -\tfrac{1}{2} \frac{\Psi_g^2}{R_g^2} \frac{\partial R_g}{\partial x_i} \tag{3.71}$$

The effective-gap form is used for the reluctance;

$$f_i = - \frac{\tfrac{1}{2}\ \Psi_g^2}{\dfrac{4C^2 g^2}{\mu_o^2 A_g^2}} \frac{2}{\mu_o A_g} \frac{\partial (Cg)}{\partial x_i} \tag{3.72}$$

The factor $\mu_o \Psi_g / 2g$ is the highest flux density present in the gap, as it represents the full potential dropped over the shortest distance. Label this value as B_g.

$$\frac{f_i}{A_g} = \frac{B_g^2}{\mu_o} \left\{ \frac{-1}{C^2} \frac{\partial (Cg)}{\partial x_i} \right\} \tag{3.73}$$

The bracketed term includes the effect of gap topology on the utilization of gap area. The flux density term is limited by the saturation characteristic of the iron near the gap. Clearly it is advantageous to maximize this quantity, so it is assumed that other segments of the magnetic circuit do not limit the flux to a lesser value. The normalized, non-dimensional term is labeled f_{2i}, and is seen to equal f_{1i}/C.

$$f_{2i} = \left\{ - \frac{1}{C^2} \frac{\partial (Cg)}{\partial x_i} \right\} \tag{3.74}$$

The final force-area form is thus

$$\frac{f_i}{A_g} = \frac{B_g^2}{\mu_o} f_{2i} \tag{3.75}$$

The volume of iron required depends on many aspects of the specific geometry chosen, but for axisymmetric geometries where the magnet dominates the situation, it can be approximated as follows:

1. The iron must cover all of both sides of the magnet, either in direct contact or across the gap

on the rotor. Thus in two dimensions the iron has an extent of roughly $2A_m$.

2. The iron must have a thickness h so that the total magnet flux can be carried at a suitable flux density, B_i. The area of cross-section for the flux is roughly $2\pi Rh$ where R is the radius of the gap structure.

Utilyzing equation 3.48, the volume of the iron is approximately

$$V_i \simeq \frac{2A_m \Phi_m}{2\pi R B_i} = \frac{A_m^2 B_o p}{\pi R B_i (p+1)} \tag{3.76}$$

so that the goal is to determine the area of the magnet.

The area of the gap has just been shown to be

$$A_g = \frac{\mu_o f_z}{f_2 B_g^2} \tag{3.77}$$

This is related to the area of the magnet through the modified permeance ratio,

$$R_m = p\, R_{eq} \tag{3.78}$$

The effects of R_ℓ and R_i tend to cancel one another such that

$$R_{eq} \simeq R_g \tag{3.79}$$

so that

$$\frac{\ell_m}{\mu_m A_m} = p\,\frac{2\,Cg}{\mu_o A_g} \tag{3.80}$$

In addition, the volume of the magnet from equation 3.64 is

$$V_m = \frac{2\mu_m\, g\, f_z (p+1)^2}{\eta\, B_o^2\, f_1\, p} \tag{3.81}$$

Solving this for ℓ_m and inserting into equation 3.80 yields

$$\frac{\eta\, B_o^2\, f_1\, p\, A_m^2}{2\mu_m\, g\, f_z (p+1)^2} = \frac{A_g}{p\ 2\ Cg} \tag{3.82}$$

or

$$A_m^2 = \frac{\mu_m\, f_z (p+1)^2}{B_o^2\, f_1\, C\, p^2\, \eta}\, A_g \tag{3.83}$$

Inserting the formula for A_g and recognizing that $f_2 C = f_1$;

$$A_m^2 = \frac{\mu_m \mu_o\, f_z^2 (p+1)^2}{B_o^2\, f_1^2\, B_g^2\, p^2\, \eta} \tag{3.84}$$

Finally the volume of iron can be expressed as

$$V_i \tilde{=} \frac{\mu_o \mu_m\, f_z^2 (p+1)}{\pi R\, B_o B_i B_g^2 f_1^2\, p\, \eta} \tag{3.85}$$

Just as in minimizing the magnet volume, it is desirable to have a large B_o and f_1. Unlike the magnet case, the iron volume is not minimized for p=1. The most that can be gained by raising p, however, is to cut the amount of iron in half.

Thus for expensive magnets like $SmCo_5$, p=1 is still best. For ceramic magnets p is set at two anyway, and little more is gained by further increasing this value. The inverse dependence on B_g is consistent with the earlier result for minimizing the area of the gap.

Some additional design information is made available by this expression. The square-law dependence on lift force means that it is favorable to divide the load among more than one flux loop. As the number of flux paths increases, however, the percentage of the flux lost to leakage increases. Consequently, the size of the individual flux loops should be kept large enough to retain a clearly defined flux path.

G. Stiffness

The general definition for stiffness involves the changes in all forces and torques due to an incremental translation or rotation about the center of mass of the levitated object [67]. Thus the total stiffness is actually a thirty-six element matrix:

$$S_{ij} = - \frac{df_i}{dx_j} = \Phi_g \frac{\partial \Phi_g}{\partial x_j} \frac{\partial R_g}{\partial x_i} + \tfrac{1}{2} \Phi_g^2 \frac{\partial^2 R_g}{\partial x_i \partial x_j} \qquad (3.86)$$

where it is to be understood that i and j run over six dimensions, the last three corresponding to rotation about the three primary axes. If more than one magnetic system is involved, then the stiffnesses are additive.

The flux can be represented in terms of circuit parameters as it was for the force:

$$\Phi_g = \frac{(\Psi_o' + N'I)}{(R_m' + R_g)} \tag{3.87}$$

In this form, only R_g and I are functions of x_j. Therefore,

$$\frac{\partial \Phi_g}{\partial x_j} = - \frac{(\Psi_o' + N'I)}{(R_m' + R_g)^2} \frac{\partial R_g}{\partial x_j} + \frac{N'}{(R_m' + R_g)} \frac{\partial I}{\partial x_j} \tag{3.88}$$

The total stiffness becomes

$$S_{ij} = - \frac{(\Psi_o' + N'I)^2}{(R_m' + R_g)^3} \frac{\partial R_g}{\partial x_i} \frac{\partial R_g}{\partial x_j} + \frac{(\Psi_o' + N'I)N'}{(R_m' + R_g)^2} \frac{\partial R_g}{\partial x_i} \frac{\partial I}{\partial x_j} + \tfrac{1}{2} \frac{(\Psi_o' + N'I)^2}{(R_m' + R_g)^2} \frac{\partial^2 R_g}{\partial x_i \partial x_j} \tag{3.89}$$

The primary reason for wanting to know the stiffness lies in determining the stability of the system. But only the diagonal terms in the matrix affect stability, so these become the values of interest:

$$S_i = - \frac{df_i}{dx_i} = - \frac{(\Psi_o' + N'I)^2}{(R_m' + R_g)^3} \left[\frac{\partial R_g}{\partial x_i}\right]^2 + \tfrac{1}{2} \frac{(\Psi_o' + N'I)^2}{(R_m' + R_g)^2} \frac{\partial^2 R_g}{\partial x_i^2} + \frac{(\Psi_o' + N'I)}{(R_m' + R_g)^2} \frac{\partial R_g}{\partial x_i} \frac{\partial I}{\partial x_i} \tag{3.90}$$

Positive stiffness corresponds to stability for motion about

an equilibrium in the specified direction. Complete stability requires all diagonal stiffness terms to be positive.

The last term, which represents current feedback, can be considered separately and added back later as needed. The remaining two terms will be identified as the "magnetic stiffness", S_i^m. This stiffness can be written in terms of the flux as

$$S_i^m = \tfrac{1}{2}\,\Phi_g^2\left\{\frac{\partial^2 R_g}{\partial x_i^2} - \frac{2}{(R_m' + R_g)}\left(\frac{\partial R_g}{\partial x_i}\right)^2\right\} \tag{3.91}$$

or in terms of the force as

$$S_i^m = \tfrac{1}{2}\,\Phi_g^2\,\frac{\partial^2 R_g}{\partial x_i} - \frac{2f_i}{(R_m' + R_g)}\,\frac{\partial R_g}{\partial x_i} \tag{3.92}$$

If the system does have an equilibrium position in a z-directed gravitational field, then at equilibrium all torques and forces in directions other than z are zero. For these directions,

$$S_i^m = \tfrac{1}{2}\,\Phi_g^2\,\frac{\partial^2 R_g}{\partial x_i^2}\;; \qquad x_i \neq z \tag{3.93}$$

This expression is valuable in that it allows symmetry to be used to determine whether the equilibrium is a stable one for many modes of motion.

The stiffness can be related to the magnet volume and gap area following very similar steps to those used for the force. In fact the only difference is to replace

$$\frac{\partial R_g}{\partial x_i} \rightarrow \left\{ \frac{\partial^2 R_g}{\partial x_i^2} - \frac{2}{R_m' + R_g} \left[\frac{\partial R_g}{\partial x_i} \right]^2 \right\} \tag{3.94}$$

The effects of R_ℓ and R_i tend to cancel, making $R_m' \simeq R_m$. This allows the substitution to be written in the more circuit-independent form

$$\frac{\partial R_g}{\partial x_i} \rightarrow \left\{ \frac{\partial^2 R_g}{\partial x_i^2} - \frac{2}{(p+1) R_g} \left[\frac{\partial R_g}{\partial x_i} \right]^2 \right\} \tag{3.95}$$

Making this substitution results in the necessary formula:

$$\frac{S_i}{V_m} = \eta \frac{B_o^2}{2\mu_m g^2} \frac{p}{(p+1)^2} \left\{ \frac{g^2}{R_g} \frac{\partial^2 R_g}{\partial x_i^2} - \frac{2}{(p+1)} \left[\frac{g}{R_g} \frac{\partial R_g}{\partial x_i} \right]^2 \right\} \tag{3.96}$$

or

$$\frac{S_i}{V_m} = \eta \frac{(BH)_m}{2g^2} \left\{ \frac{g}{C} \frac{\partial^2 (Cg)}{\partial x_i} - \frac{2}{(p+1)} \left[\frac{1}{C} \frac{\partial (gC)}{\partial x_i} \right]^2 \right\} \tag{3.97}$$

The last bracketed expression is labeled f_3^p, where the superscript designates the value of p used in the evaluation.

$$\frac{S_i}{V_m} = \eta \frac{(BH)_m}{2g^2} f_{3i}^p \tag{3.98}$$

Finally, defining $f_4^p = f_3^p / C$ in a manner similar to the force expression,

$$\frac{S_i}{A_g} = \frac{B_g^2}{\mu_o g} f_{4i}^p \tag{3.99}$$

H. Toothed-Gap Reluctance

Magnetic bearings based on attraction between ferromagnetic surfaces require air gaps which have a toothed structure similar to those shown in figure 3.10. For axial-gap bearings the teeth are needed to provide radial stiffness. In this case the teeth remain aligned. For radial-gap bearings the teeth are necessary to obtain the primary lift force. The teeth attempt to align themselves, but the load always forces the rotor teeth to sag below their stator counterparts.

The geometry to be evaluated is that of figure 3.10a. The results are presumed to be approximately true for the situation of figure 3.10b as well. The flanging of the teeth allows a higher flux level at the gap to be realized, but has little effect on the active region near the faces of the teeth. Without the flanging, saturation would occur first at the base of the teeth. The opposing teeth will be presumed to be equipotential surfaces. Some saturation certainly will occur at the corners of the teeth, but this effect is not expected to be large. These assumptions will be checked by comparison of predictions based on this theory to experimental data published by J. Walowit.

The goal is to evaluate the functions f_1 through f_4 for different ratios of λ/g, t/λ, and δ/λ so that an optimum topology can be selected and maximum values of the f

Figure 3.10

TOOTHED GAPS IN MAGNETIC BEARINGS

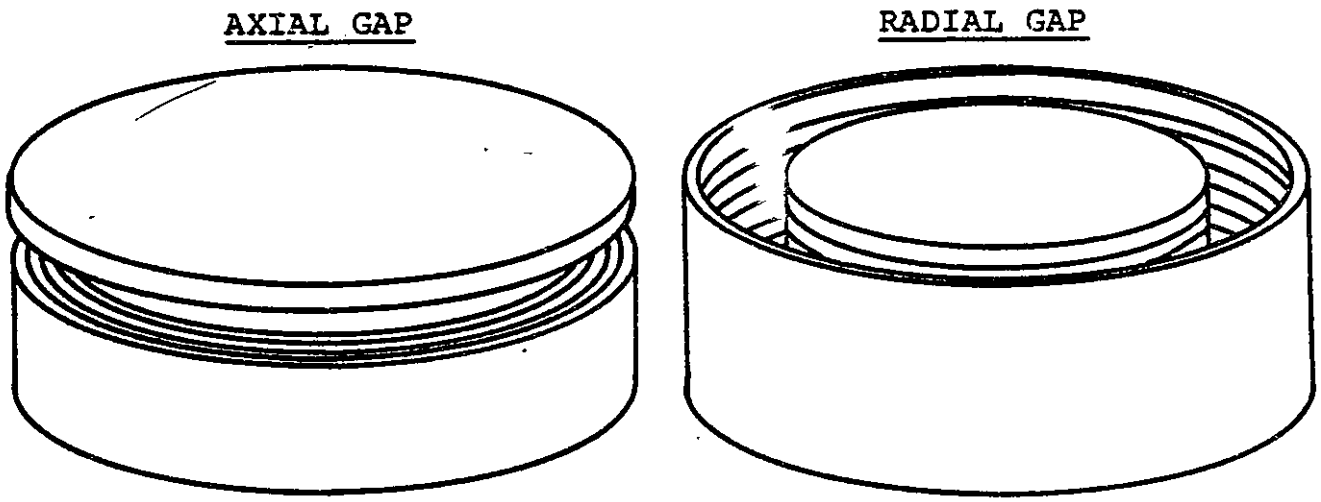

Stripes indicate toothed structure

TOOTH STRUCTURE

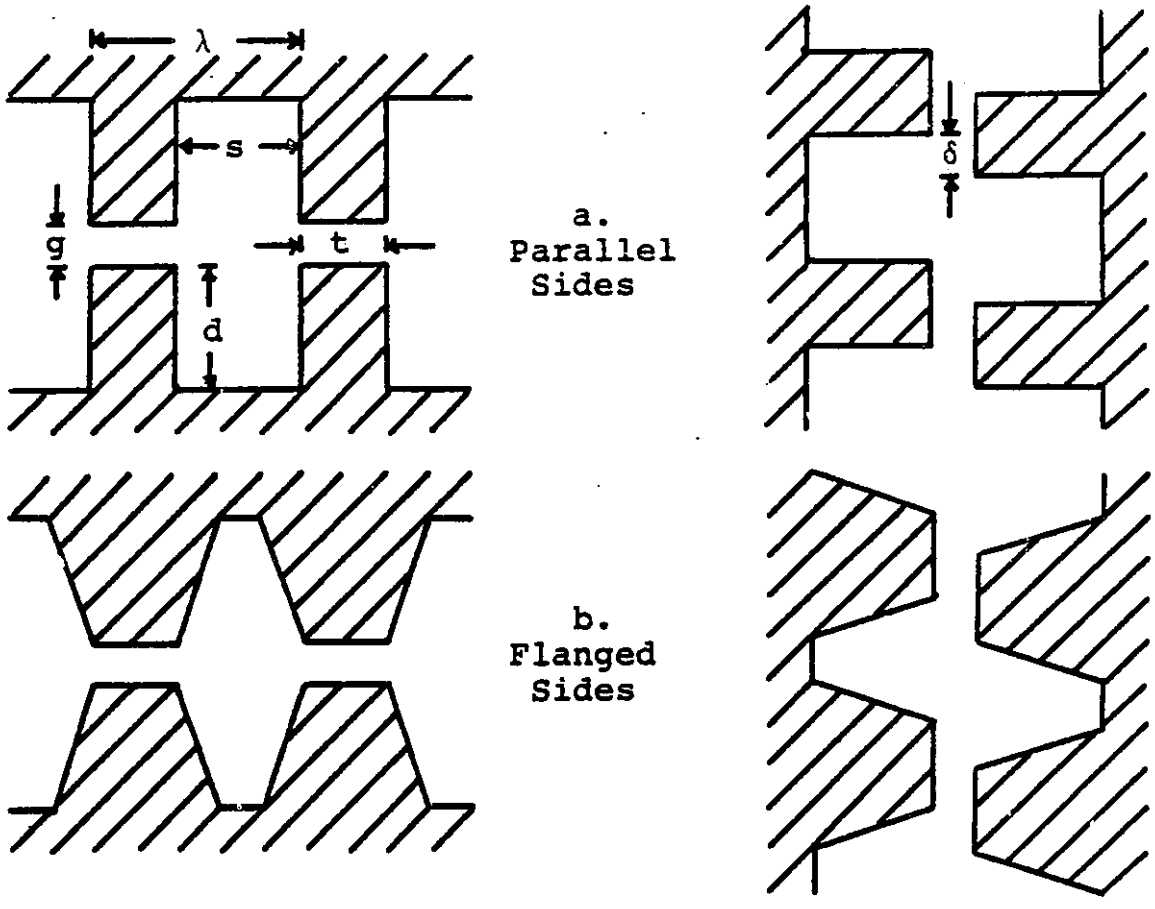

parameters determined. At the heart of this is the evaluation of C and its derivatives.

a. Normal Force

For the axial-gap topology the teeth are aligned so that $\delta/\lambda=0$. Furthermore it is the force in the "normal" direction which is of primary concern. If the slots between teeth are at least as deep as they are wide (d>s), and the teeth are at least as broad as the gap (t>g), then the problem is well described by the geometry shown in figure 3.11. The field solution for this situation can be obtained by conformal transformation, as was first done by F.W. Carter in the early 1900's [10]. From this method the effective gap coefficient, C, can be obtained. When applied to slotted structures such as these, the coefficient C is referred to as "Carter's coefficient" in recognition of his pioneering work in the area. The resulting formula, for aligned teeth, is

$$C = \frac{1}{1 - \zeta(s/\lambda)} \tag{3.100}$$

where

$$\zeta = \frac{2}{\pi}\left\{\tan^{-1}(s/g) - \frac{g}{2s}\ln[1 + (s/g)^2]\right\} \tag{3.101}$$

The first derivative becomes

Figure 3.11

CONFORMAL MAPPING OF TOOTHED AIR-GAP FIELDS

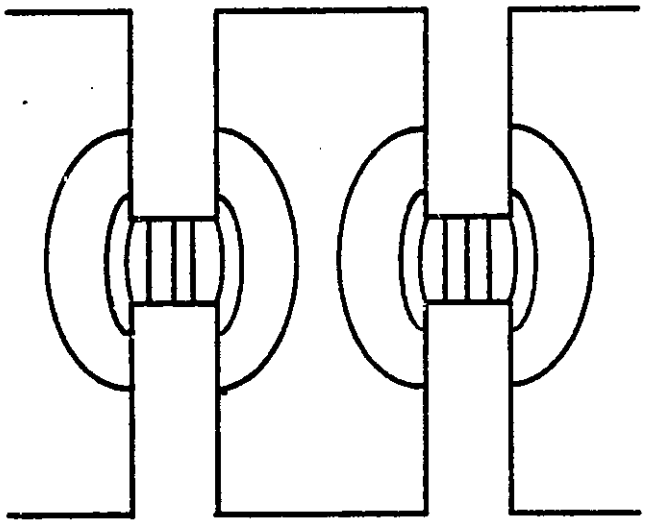

Toothed Structure
And Approximate
Field Lines

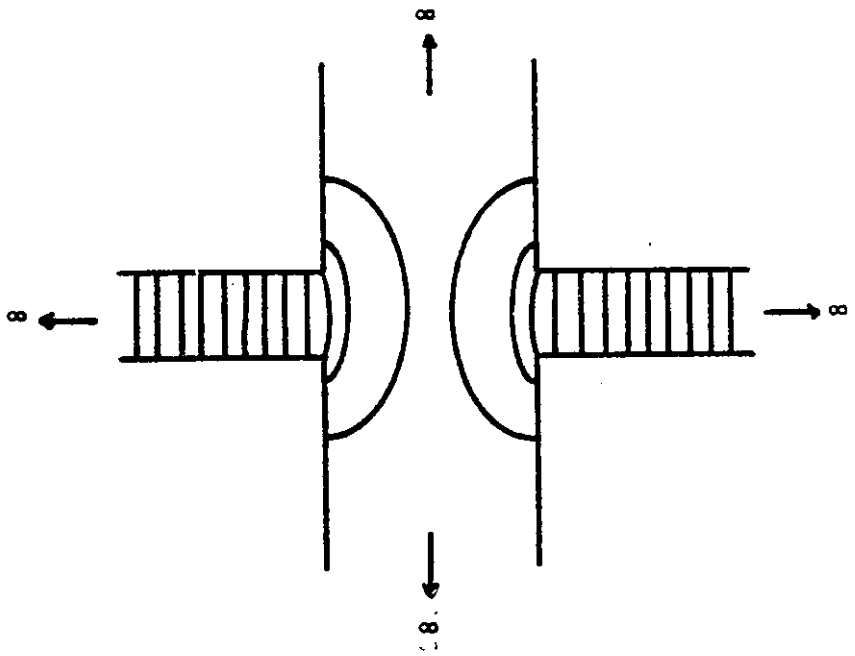

Configuration Used
By Carter In
Transformation

$$\frac{\partial(gC)}{\partial x_n} = C\{1 - \frac{2}{\pi}(s/\lambda)C \frac{g}{2s} \ln[1 + (s/g)^2] \frac{\partial g}{\partial x_n} \qquad (3.102)$$

where the "n" emphasizes that this is for displacements normal to the interface. This expression allows the evaluation of the the lift force in an axial magnetic bearing. Specifically,

$$f_{ln} = 1 - (C/\pi)(g/\lambda) \ln[1 + (s/g)^2] \qquad (3.103)$$

b. Transverse Motion - Cosine Model

Carter solved another problem using a conformal transformation in 1941. This problem dealt with the case of teeth exactly centered over the opposing slots. That is, for teeth exactly mis-aligned. The solution included elliptic integrals which required numerical integration, and as a result the work was never published until 1971, when Mukherji and Neville put a computer to the task [52]. Their results along with a similar graphical portrayal of the aligned-teeth situation, are shown in figures 3.12 and 3.13.

The beauty of this work is that a reasonable approximation to the value of C as a function of transverse displacement can be obtained. This is done by assuming a cosinusoidal dependence between the known maximum and minimum values:

Figure 3.12

EFFECTIVE-GAP COEFFICIENT

Mis-Aligned Teeth

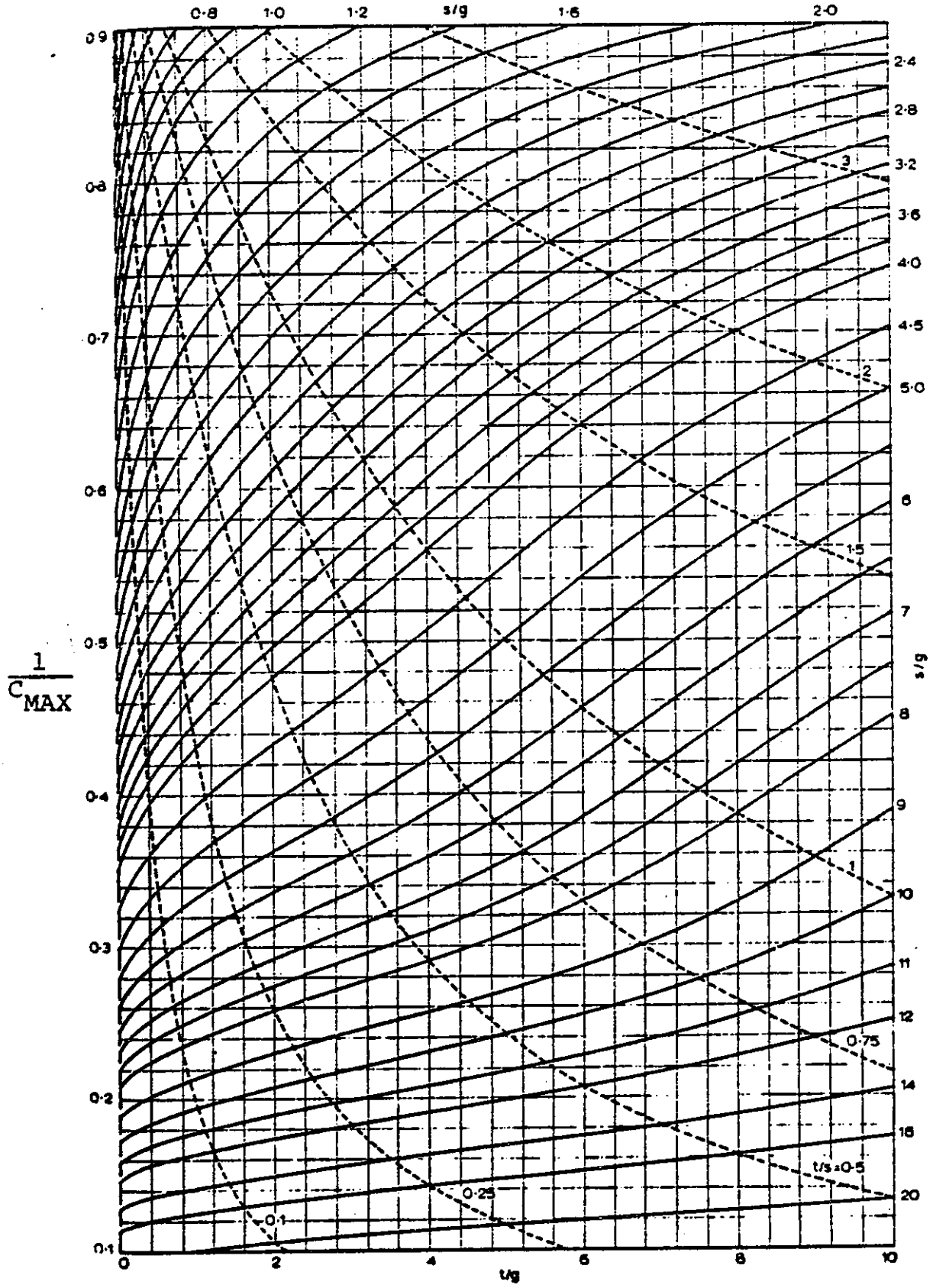

From Mukherji and Neville, Proc. of IEE 118, 9

Figure 3.13

EFFECTIVE-GAP COEFFICIENT

Aligned Teeth

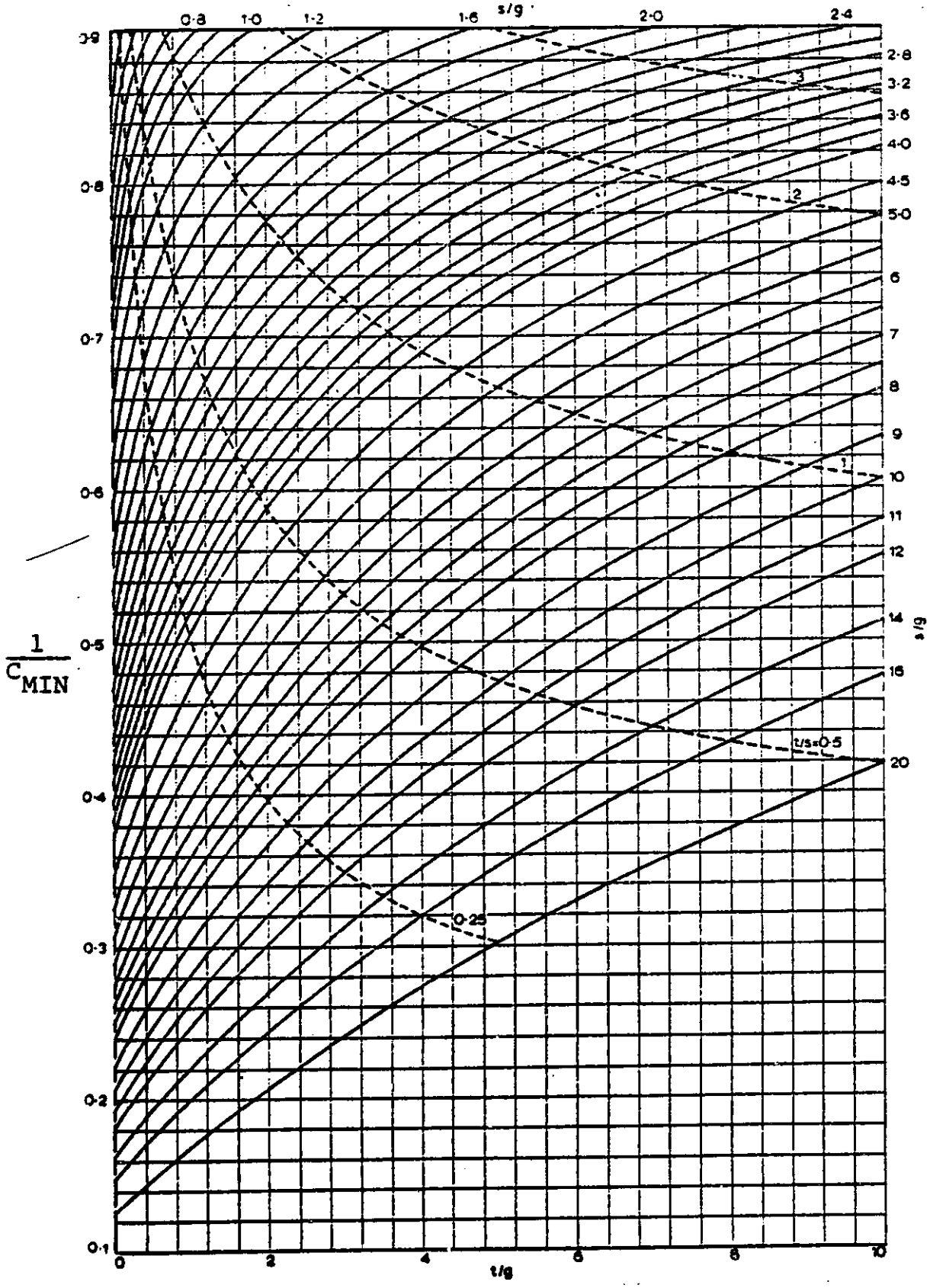

From Mukherji and Neville, Proc. of IEE 118, 9

$$C = \frac{C_{MIN} + C_{MAX}}{2} - \frac{C_{MAX} - C_{MIN}}{2} \cos[2\pi(\delta/\lambda)] \qquad (3.104)$$

where C_{MIN} corresponds to aligned teeth ($\delta/\lambda=0$) and C_{MAX} to exactly mis-aligned teeth ($\delta/\lambda=.5$). For transverse displacements, g is constant so that the derivatives can be written as

$$g \frac{\partial C}{\partial x_T} = \frac{\pi(C_{MAX} - C_{MIN})}{(\lambda/g)} \sin[2\pi(\delta/\lambda)] \qquad (3.105)$$

$$g^2 \frac{\partial^2 C}{\partial x_T^2} = \frac{2\pi^2(C_{MAX} - C_{MIN})}{(\lambda/g)^2} \cos[2\pi(\delta/\lambda)] \qquad (3.106)$$

where the "T" emphasizes that these expressions apply to transverse displacements only.

For transverse displacements there are thus three independent parameters: λ/g, t/λ, and δ/λ. From the first two of these values C_{MIN} and C_{MAX} can be found. In order to use Mukherji and Neville's graphs to do this, it is necessary to transpose the parameters to the proper form,

$$t/g = t/\lambda \cdot \lambda/g \,, \qquad s/g = (\lambda/g)(1 - t/\lambda) \qquad (3.107)$$

Once the derivatives are found, the four gap-influence factors (f) can be calculated.

The principle goal of this treatment of gap reluctance is to find maximum values for the f coefficients. But finding optimum parameters in a three dimensional space can be quite

difficult. Fortunately, several simplifications are possible. First of all, it is apparent from equations 3.105 and 3.106 and the expressions for the gap-influence factors that f_{1T} and f_{2T}, which are based on transverse force, will have maximum values near $\delta/\lambda=.25$ because of their sinusoidal dependence. f_{3T} and f_{4T}, on the other hand, are based on stiffness and will have maximum values near $\delta/\lambda=0$. This adds an additional simplification, since at $\delta/\lambda=0$ f_{3T} and f_{4T} are independent of the value of p. Thus the δ/λ dimension is reduced to two initial points of interest.

Over one hundred combinations of λ/g and t/λ ranging from $\lambda/g=2$ and $t/\lambda=.1$ to $\lambda/g=20$ and $t/\lambda=.5$ were read into a computer and values of the gap-influence coefficients determined for $\delta/\lambda=0$ or .25 as appropriate. Remarkably, the factors based on magnet volume, f_{1T} and f_{3T}, always peaked close to $t/\lambda=.25$. The factors based on area, f_{2T} and f_{4T}, had peaks in t/λ which shifted for different λ/g. However, the peaks were such that assuming the maximum to occur at $t/\lambda=.42$ never resulted in more than a 10% error. Consequently the t/λ dependence can also be reduced to only two points.

Shown in figure 3.14 are the calculated dependence on λ/g for the gap-influence coefficients with the appropriate selection of t/λ and δ/λ. The accuracy of the cosine model is expected to be very good for small values of λ/g where the variations in C are small. For large values of λ/g, say greater than 10, the model is almost certainly in error. Taking this into consideration, five interesting pairs of λ/g

Figure 3.14

GAP-INFLUENCE COEFFICIENTS

Cosine Model

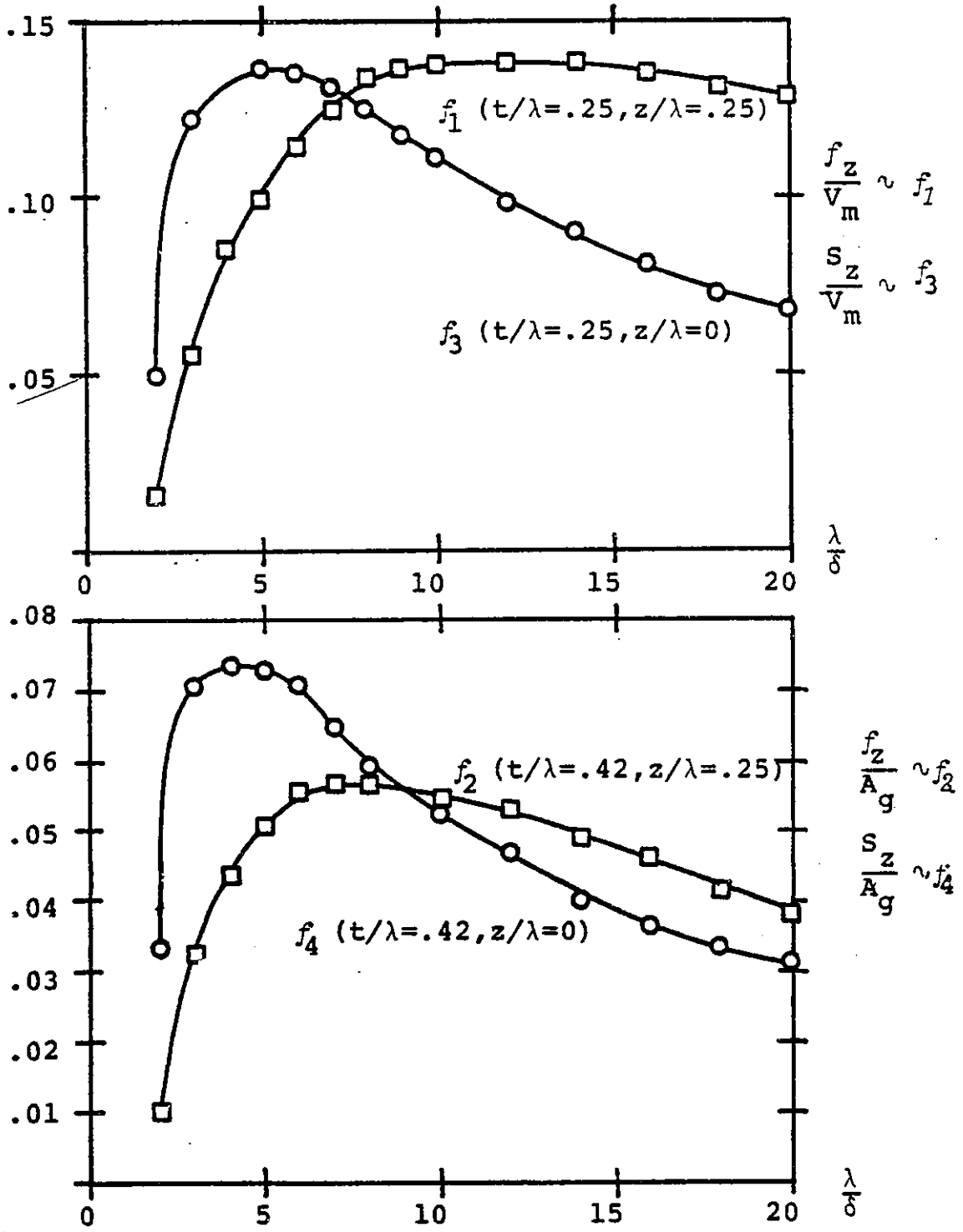

and t/λ were selected for more thorough study:

1. $\lambda/g = 4$, $t/\lambda = .25$
2. $\lambda/g = 10$, $t/\lambda = .25$
3. $\lambda/g = 20$, $t/\lambda = .25$
4. $\lambda/g = 10$, $t/\lambda = .42$
5. $\lambda/g = 20$, $t/\lambda = .42$

c. Transverse Motion - Computer Field Solution

A computer program which solves spatially periodic LaPlacian problems with opposing equipotential surfaces was written. PL/1 was used to maximize execution efficiency. Unfortunately, the method of solution was the square-array relaxation technique, which proved to require excessive time to converge. The results shown in this section required a total of 8 hours of CPU time on MIT's Honeywell 6180 Multics system. Future work in this area should first optimize the field solution routine.

The geometries of each of the five selected pairs of λ/g and t/λ were solved on the computer. For each configuration, the teeth were displaced in steps from $\delta/\lambda=0$ to $\delta/\lambda=.5$, and the magnetic potential field solved for each situation. In each case, the depth of the slot was set equal to the slot width. This kept the region of field solution to a minimum.

Once the field solution was available for each situation, it was necessary to calculate a value of C. This was done by finding the total flux for a given potential difference across the gap. The flux was determined by "integrating" numerically the flux density along the midplane of the gap, where the

intensity of the field was taken to be the difference in adjacent potential values divided by their separation.

The accuracy with which the second derivative of C with respect to the transverse displacement could be determined was found to be quite poor. It is possible, however, to determine the first derivative of C directly from the potential field, and the slope of this curve can be reliably determined. To find the first derivative from the potential, the transverse force was computed directly using the method of the Maxwell stress tensor. It was found that greatest accuracy is obtained by taking the surface for evaluation at the midplane of the gap, as far from the material interfaces as possible.

Shown in figure 3.15 are the computer-generated values of C as a function of displacement for the five test configurations. Also shown is the curve corresponding to the cosine model, using tabulated values from Mukherji and Neville to set C_{MIN} and C_{MAX}. Thus the values of C_{MIN} and C_{MAX} serve as checks on the accuracy of the computer solution, while the computer results allow evaluation of the cosine approximation. Shown in figure 3.16 are the first derivatives calculated using the Maxwell stress tensor. Again the derivatives predicted by the cosine model are shown for comparison. The computer solution appears to be very accurate for all but the value of C in the $\lambda/g=4$ configuration. Fortunately, the weakest area of computer solution is the strongest area for the cosine model. Together they allow an accurate view of the entire range. Notice that even for large λ/g the cosine model

Figure 3.15

C VERSUS DISPLACEMENT $(\frac{\delta}{\lambda})$

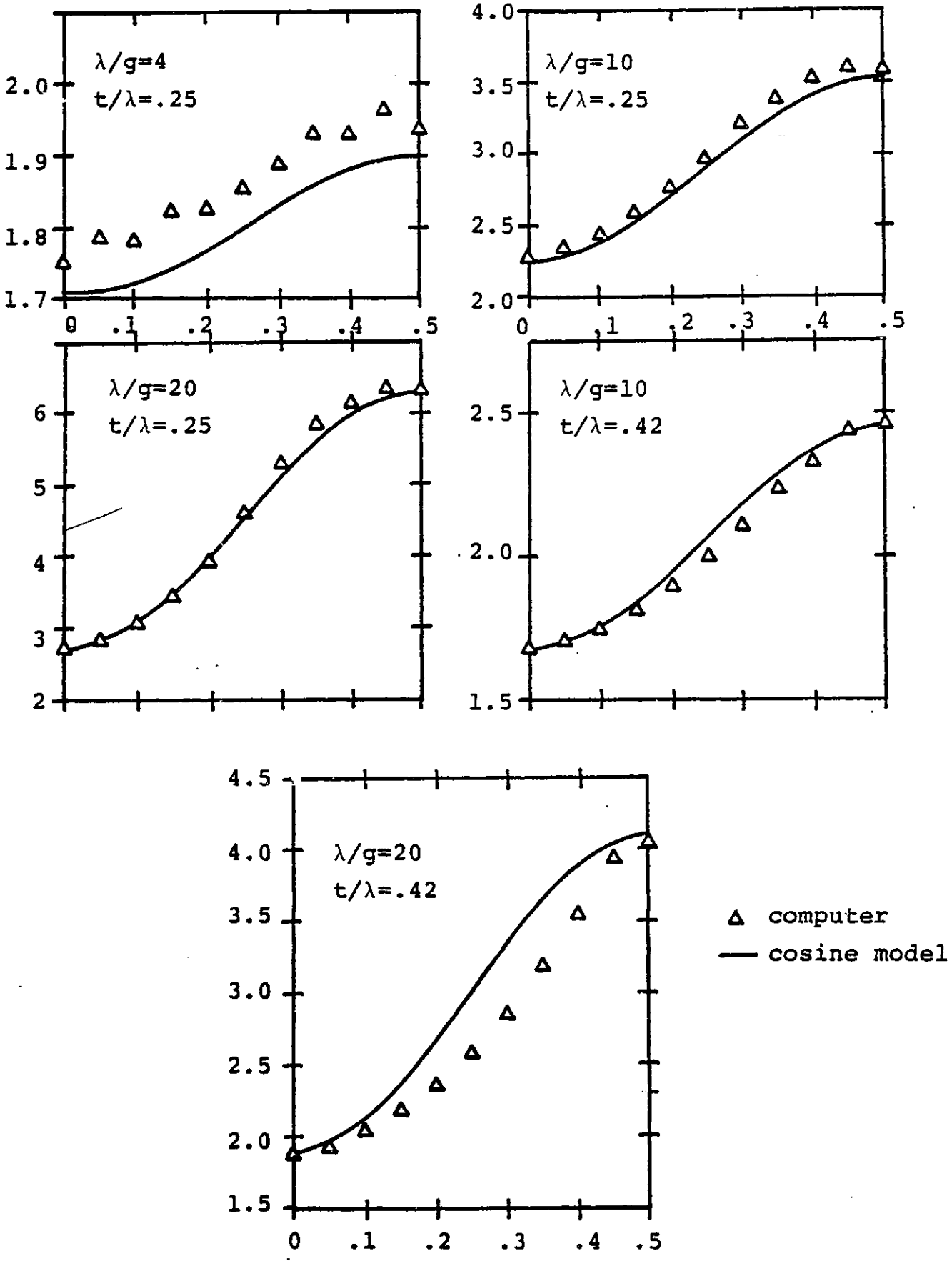

Figure 3.16

$g\frac{\partial C}{\partial z}$ VERSUS DISPLACEMENT $(\frac{\delta}{\lambda})$

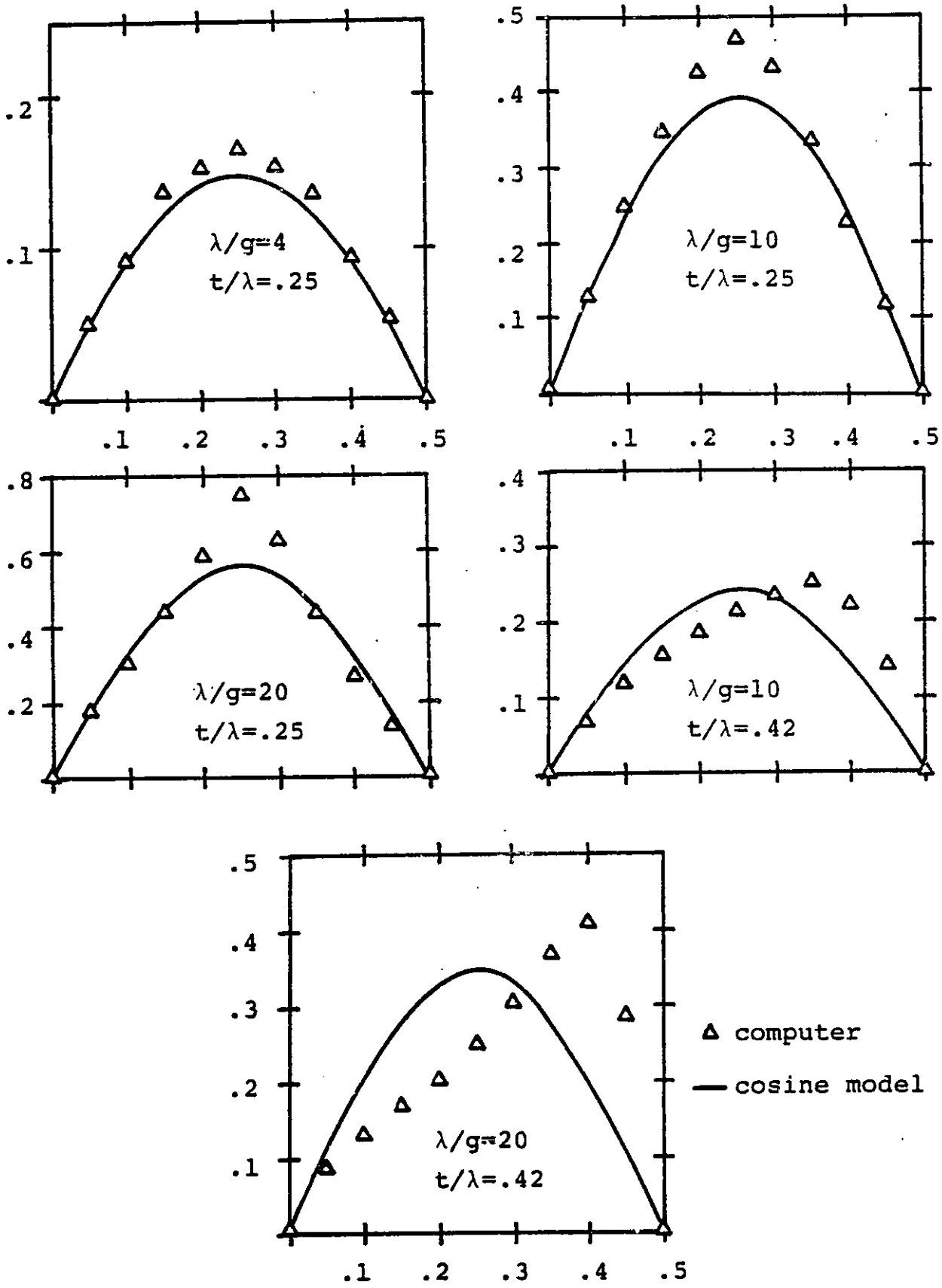

is fairly accurate for the cases with $t/\lambda=.25$, but gives erroneous results for the first derivative in the $t/\lambda=.42$ cases.

Plots for the four gap-influence coefficients are shown in figure 3.17 for all five configurations as a function of displacement, δ/λ. Note that in the range of δ/λ where f_{1T} and f_{2T} are reaching their maximum, the stiffness is approaching zero. In order to insure stability even in the presence of disturbances, some positive stiffness margin is required. The resulting trade-off of force and stiffness is illustrated in figure 3.18, where f_{1T} is plotted against f_{3T}. The trade-off between volume of magnet and gap area is illustrated by figure 3.19.

From these results, it appears that an optimum topology for an axial-gap device is near $\lambda/g=4$, $t/\lambda=.25$, where $C=1.70$, $f_{1n}=.69$, $f_{2n}=.40$, $f_{3T}=.14$, and $f_{4T}=.08$. For a radial-gap device, the best is near $\lambda/g=10$, $t/\lambda=.25$, $\delta/\lambda=.2$, where $C=2.75$, $f_{1T}=.16$, $f_{2T}=.056$, $f_{3T}^2=.03$, and $f_{4T}^2=.01$.

d. MTI Data Comparison

J. Walowit and others at Mechanical Technology, Inc. performed experiments using the magnetic system shown in figure 3.20 [72]. The apparatus allowed variable values of λ/g and δ/λ, but had a fixed t/λ of .33. A great deal of experimental data was generated, but three experiments are of particular interest:

Figure 3.17a

FORCE-MAGNET VOLUME GAP-INFLUENCE FACTOR

For Transverse Displacements

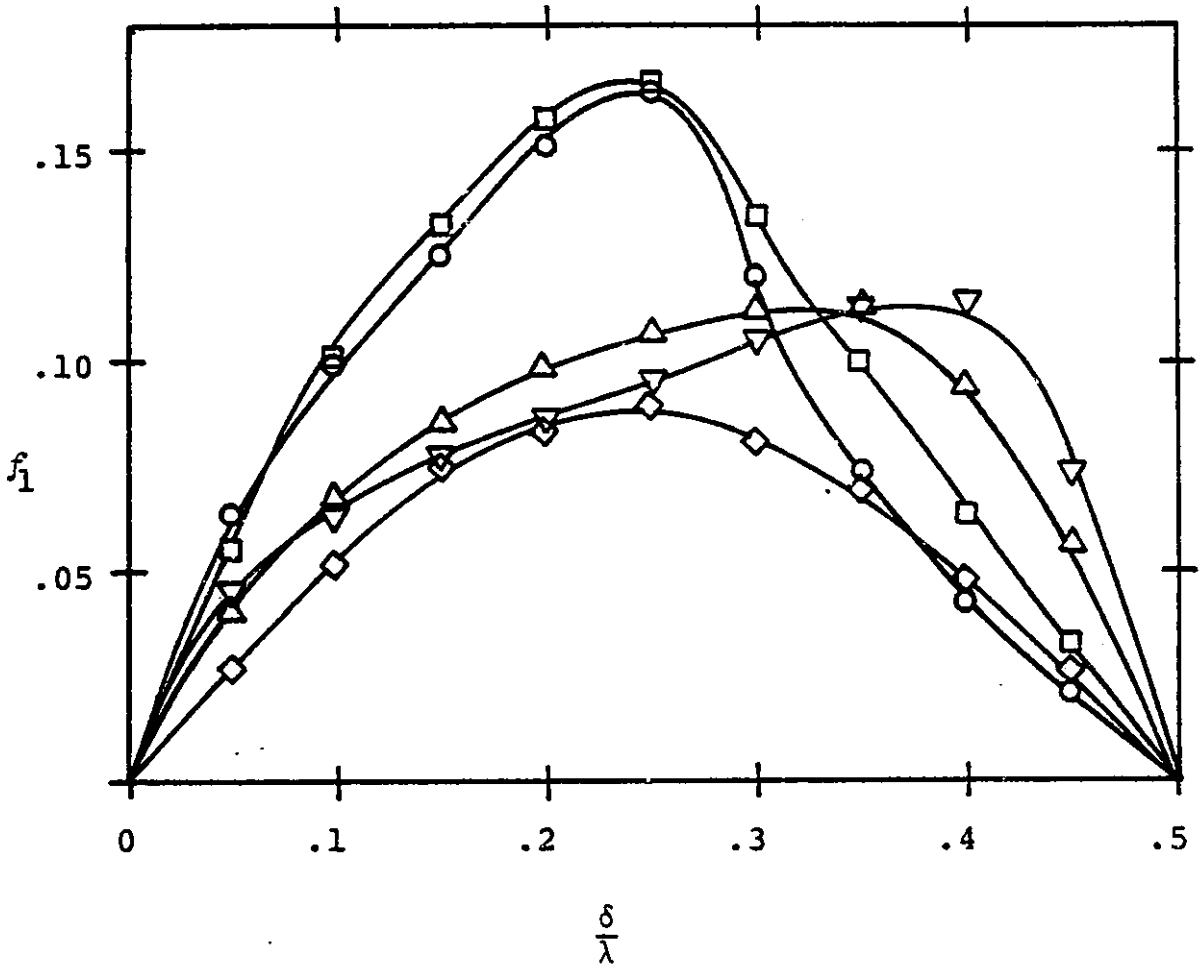

◇ λ/g=4, t/λ=.25
□ λ/g=10, t/λ=.25
○ λ/g=20, t/λ=.25
△ λ/g=10, t/λ=.42
▽ λ/g=20, t/λ=.42

Figure 3.17b
FORCE-AREA GAP-INFLUENCE FACTOR
For Transverse Displacements

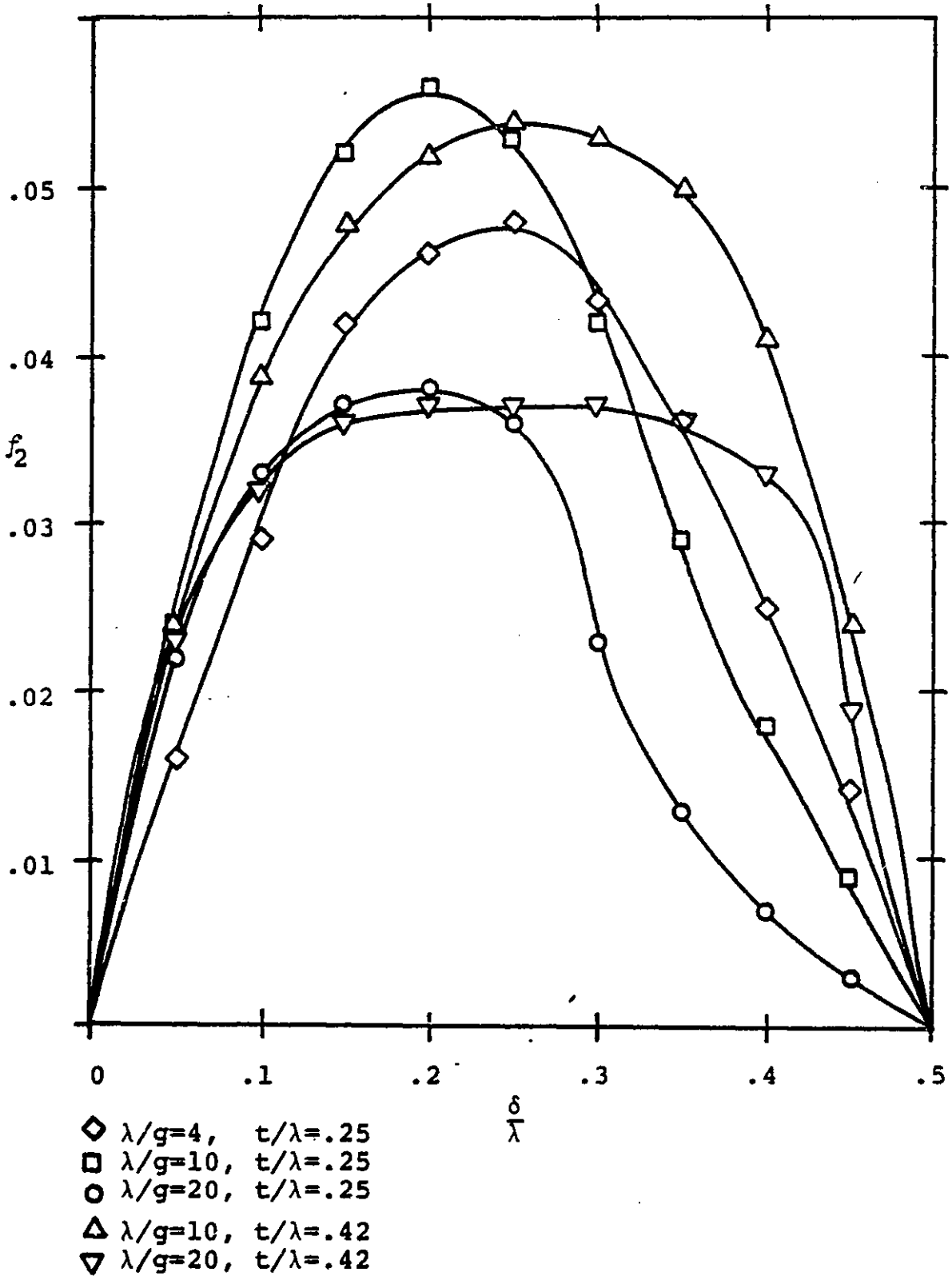

Figure 3.17c

STIFFNESS-MAGNET VOLUME GAP-INFLUENCE FACTOR

For Transverse Displacements

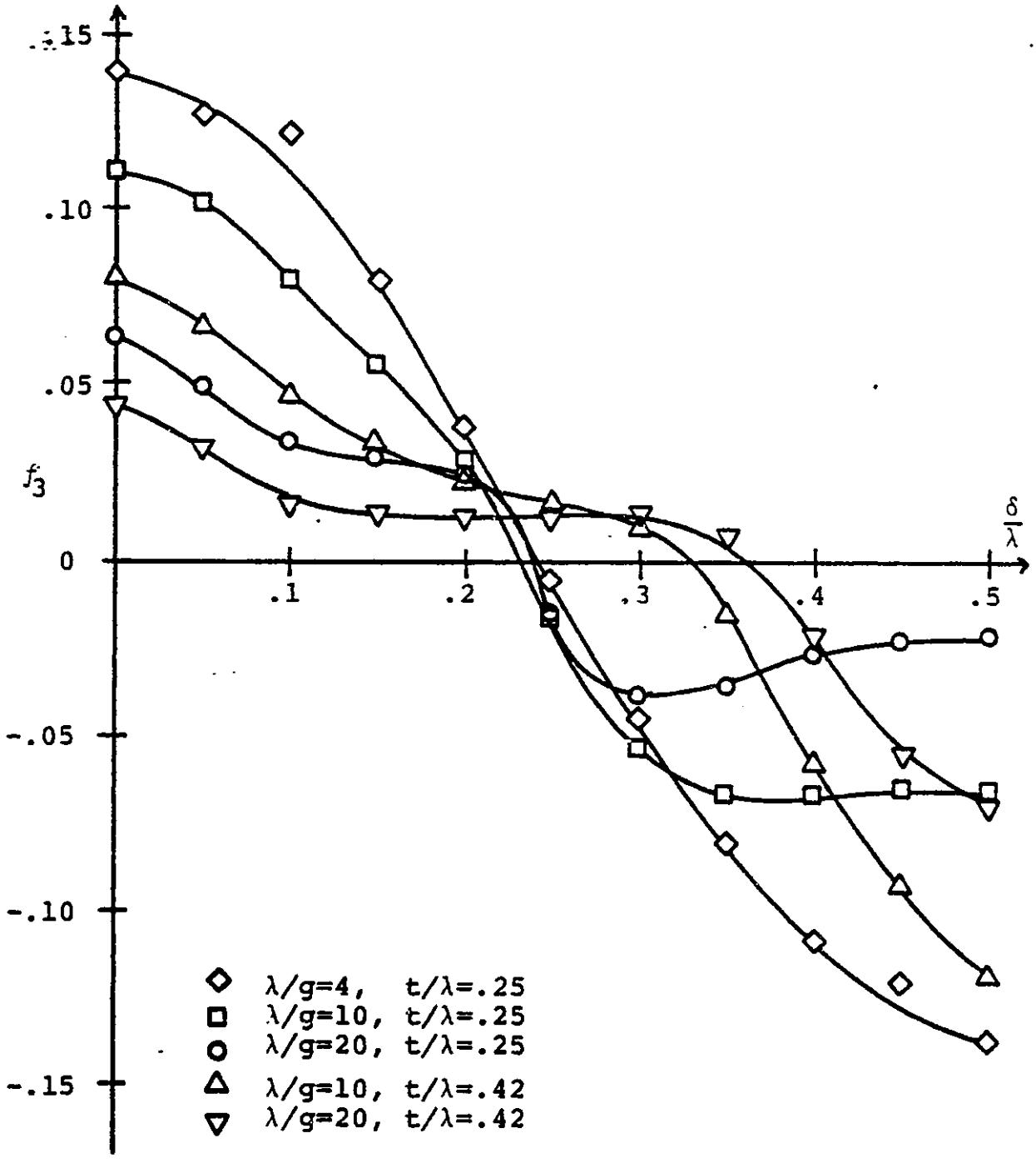

with p = 2 (Values at $\frac{z}{\lambda} = 0$ are independent of p)

Figure 3.17d

STIFFNESS-AREA GAP-INFLUENCE FACTOR

For Transverse Displacements

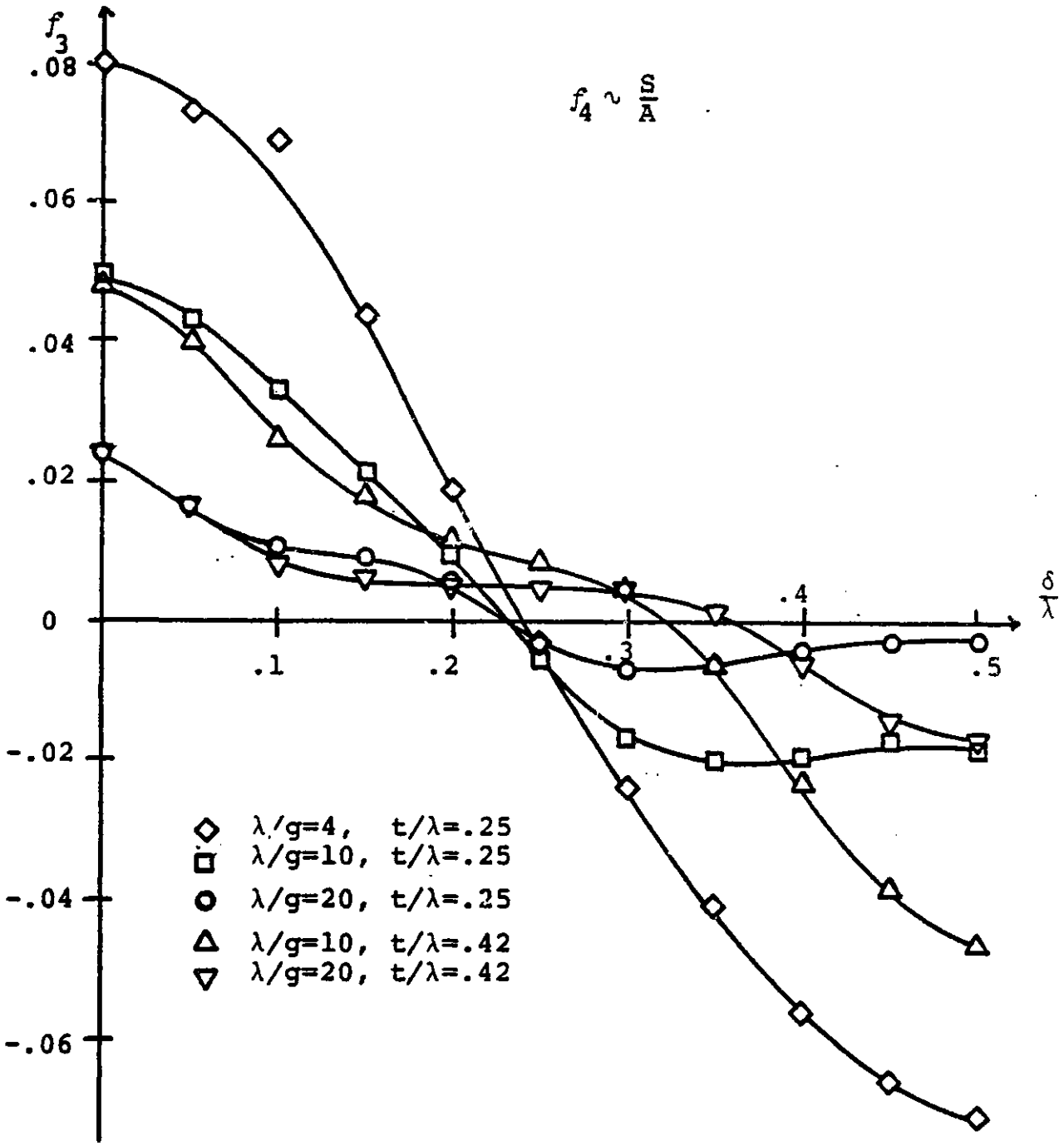

with p = 2 (Values at $\frac{z}{\lambda} = 0$ are independent of p)

Figure 3.18

FORCE VERSUS STIFFNESS

(In Terms Of Dimensionless Gap-Influence Coefficients)

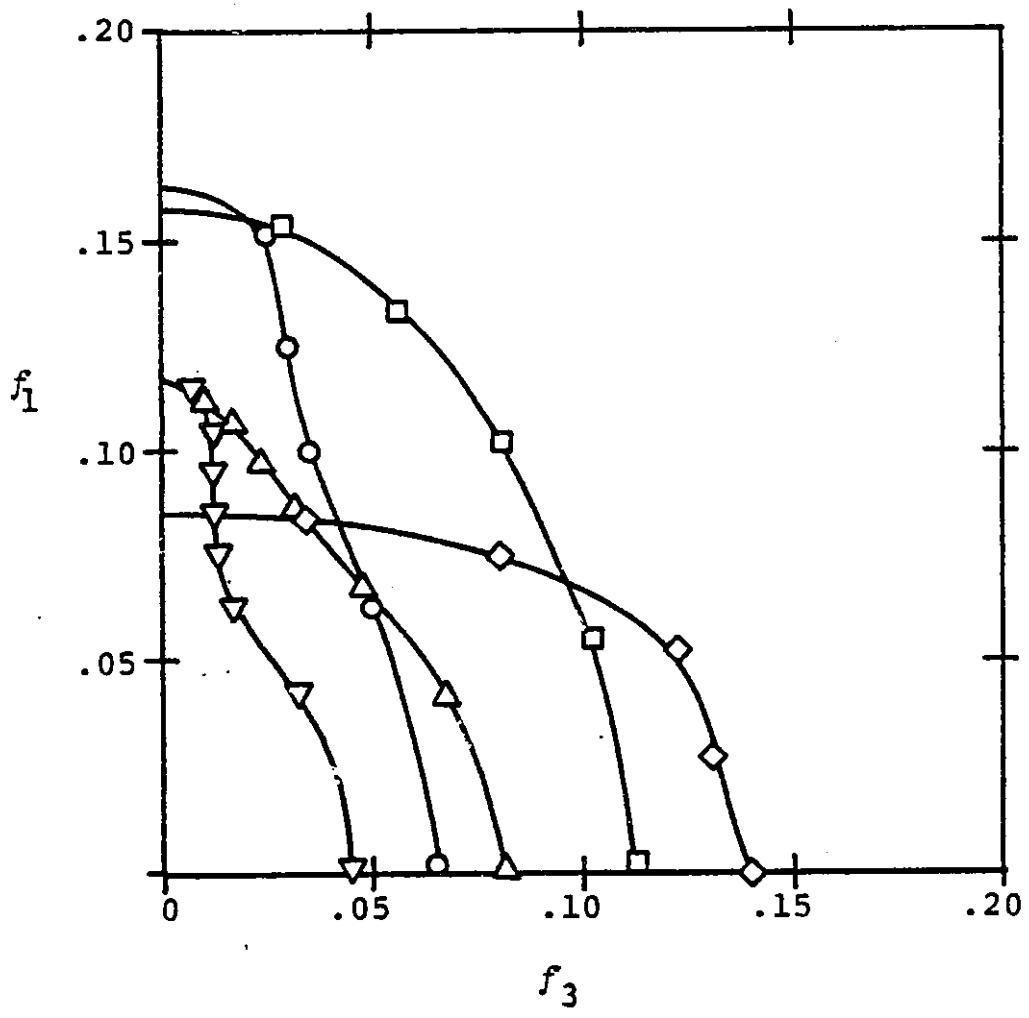

Figure 3.19

MAGNET VOLUME VERSUS GAP AREA

(In Terms Of Non-Dimensional Gap-Influence Coefficients)

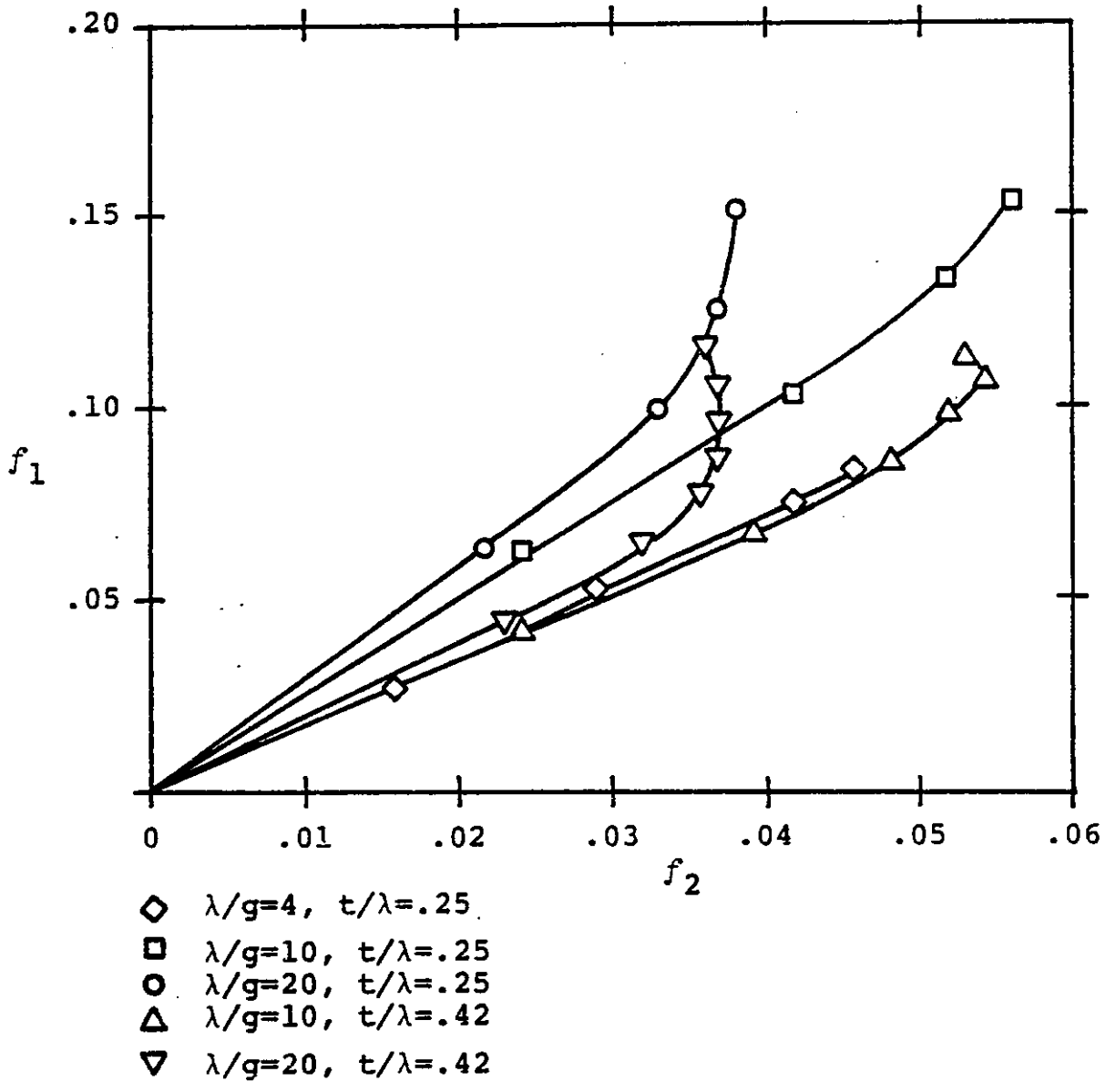

Figure 3.20

MTI* TEST CONFIGURATION

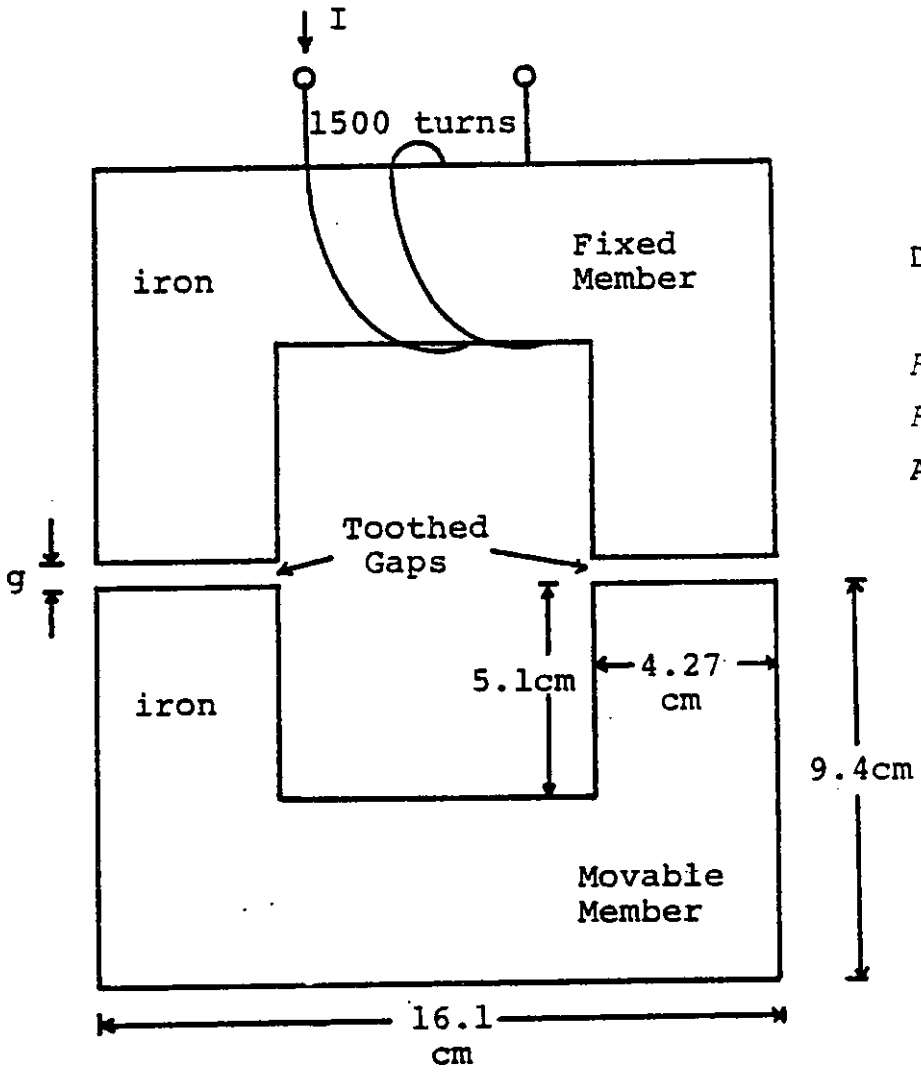

Depth into Page
6.35cm

$R_i \simeq 3 \cdot 10^4$ A/WB

$R_\ell \simeq 2 \cdot 10^6$ A/WB

$A_g = 2.7 \cdot 10^{-3}$ m^2

DETAIL OF TOOTH STRUCTURE

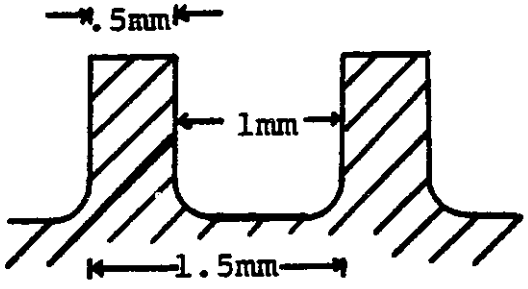

$\frac{t}{\lambda} = .33$

*J. Walowit, Mechanical Technology Inc.

1. Flux versus gap width for fixed input current. This data can be reduced to yield a plot of C versus λ/g for aligned teeth.

2. Normal force versus gap width for various input currents. This can be restated in terms of the normal derivative and compared to the value predicted in section 3Ha.

3. Tangential force versus tangential displacement for various gap widths with constant current. This plot can be reduced to a graph of $g\ \partial C/\partial x_T$ versus δ/λ for various values of λ/g.

The necessary conversions from the published raw data into useful non-dimensional quantities were made as follows:

1. The effective-gap coefficient is determined according to

$$C = \frac{N\Gamma}{\Phi} \frac{\mu_o A g}{2g} \tag{3.107}$$

2. The normal derivative is found in accordance with

$$\frac{\partial (gC)}{\partial x_n} = \frac{\mu_o f_n A g}{\Phi^2} \tag{3.108}$$

where Φ is determined for the given current from the previous graph.

3. The tangential derivative is determined using

$$g \frac{C_{MIN}^{2}}{C^2} \frac{\partial C}{\partial x_T} = \frac{\mu_o f_T A_g}{\Phi_o^2} \qquad (3.109)$$

where Φ_o is given as the flux when the teeth are aligned.

Graphs displaying these comparisons are shown in figures 3.21, 3.22, and 3.23. As is apparent, the agreement is quite good and it would appear that both the force derivation given earlier and the cosine model just presented are valid design tools.

Figure 3.21

MTI* FLUX-CURRENT DATA: ALIGNED TEETH

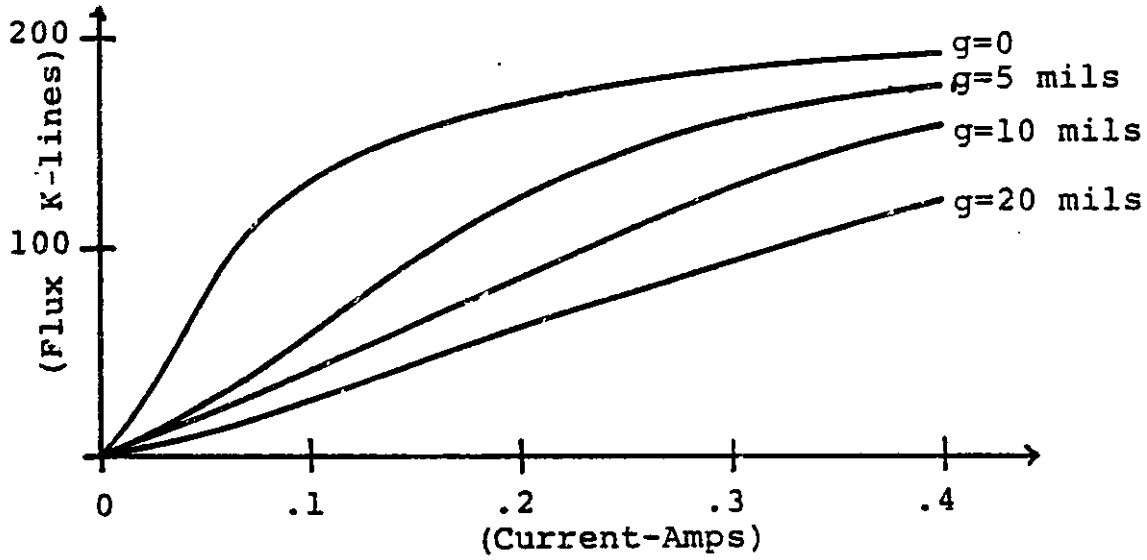

The potential drop across the iron, indicated by the g = 0 line, is subtracted from the other curves, yielding

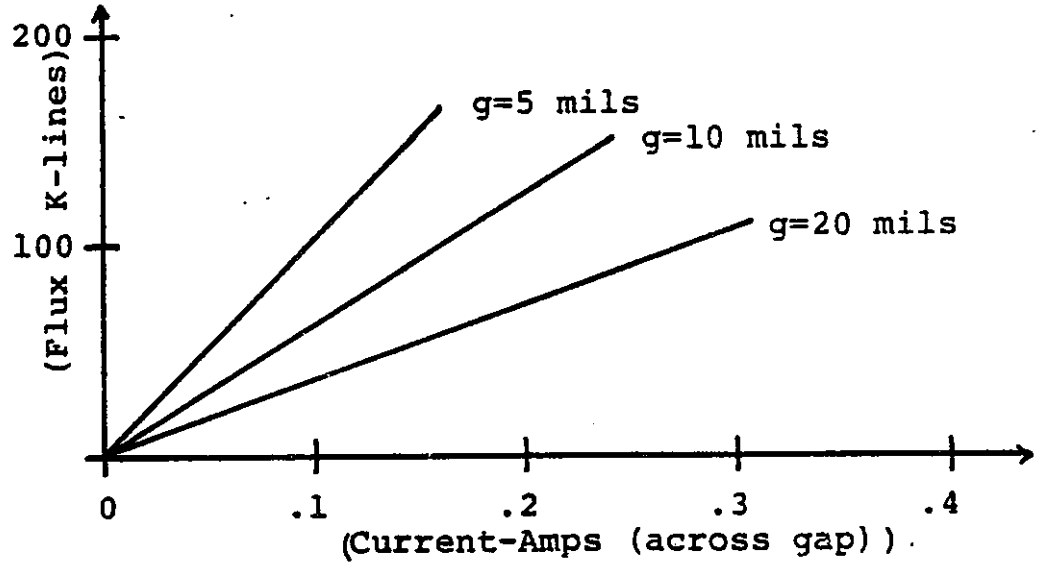

From these linear curves, values of the gap reluctance, and hence C, can be determined:

g mils	g mm	$\frac{\lambda}{g}$	R_g from data	C_{MTI}	$C_{calculated}$	error, %
5	.13	12	$1.45 \cdot 10^5$	1.89	2.01	6
10	.25	6	$2.40 \cdot 10^5$	1.63	1.70	4
20	.51	3	$4.13 \cdot 10^5$	1.37	1.43	4

* J. Walowit, Mechanical Technology, Inc.

Figure 3.22

MTI* NORMAL FORCE DATA

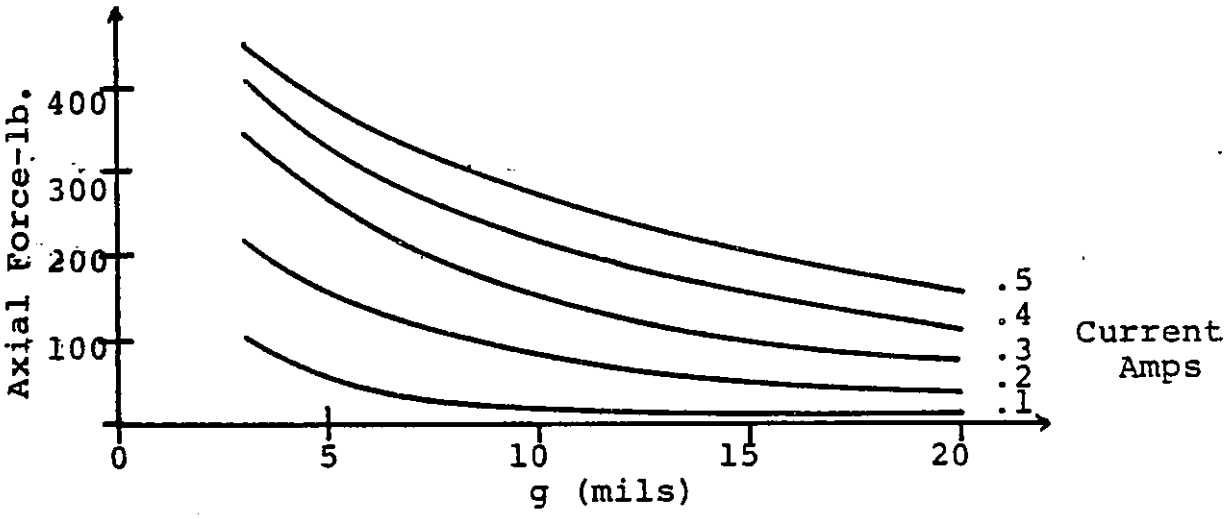

This data can be used with the graph of figure 3.21 to obtain force versus flux for assorted gaps. A square-law abscissa is used to obtain linear plots.

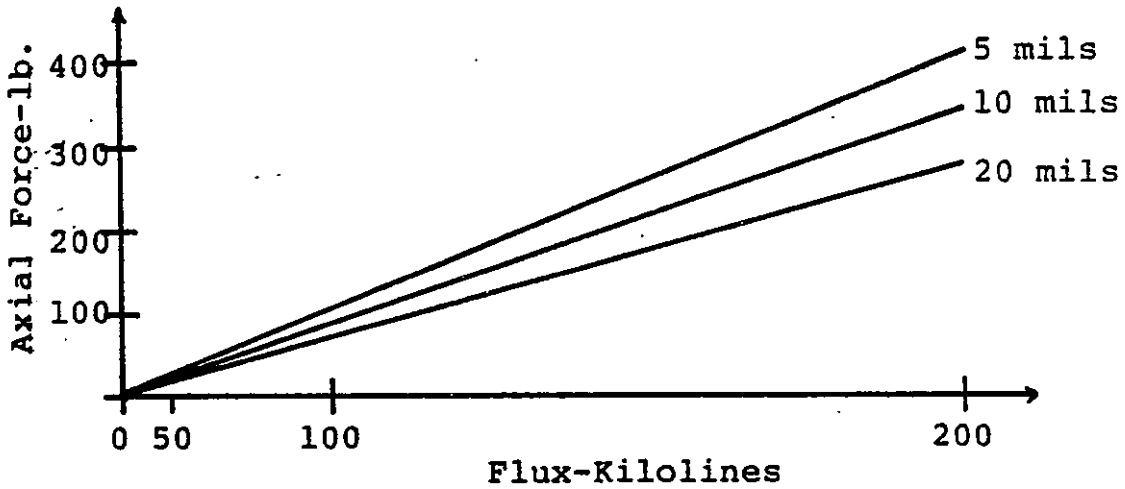

Gap g mils	Gap g mm	$\frac{\lambda}{g}$	force at 200 Kilolines lbs	force at 200 Kilolines N.	$\frac{\partial(gC)}{\partial x_n}$ MTI	$\frac{\partial(gC)}{\partial x_n}$ calculated	error %
5	.13	12	405	1800	1.53	1.56	2
10	.25	6	340	1510	1.28	1.27	1
20	.51	3	275	1220	1.03	1.08	5

* J. Walowit, Mechanical Technology, Inc.

Figure 3.23

MTI* TANGENTIAL FORCE DATA

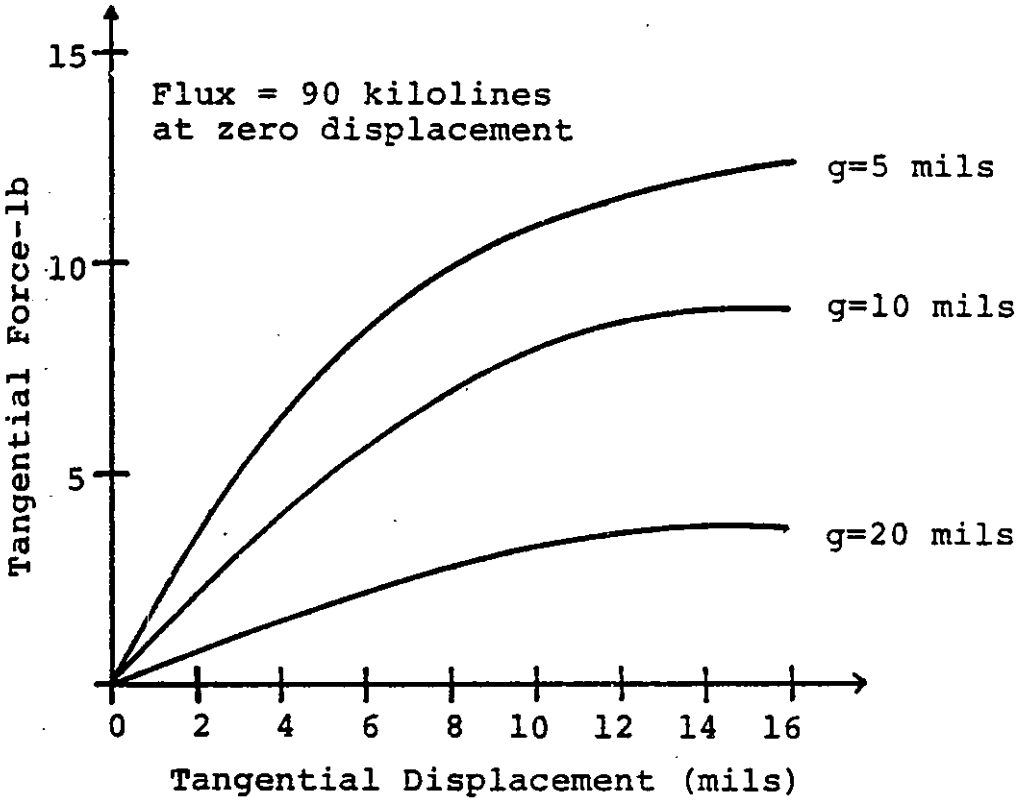

These plots can be converted to dimensionless form, and compared to predictions of the cosine model.

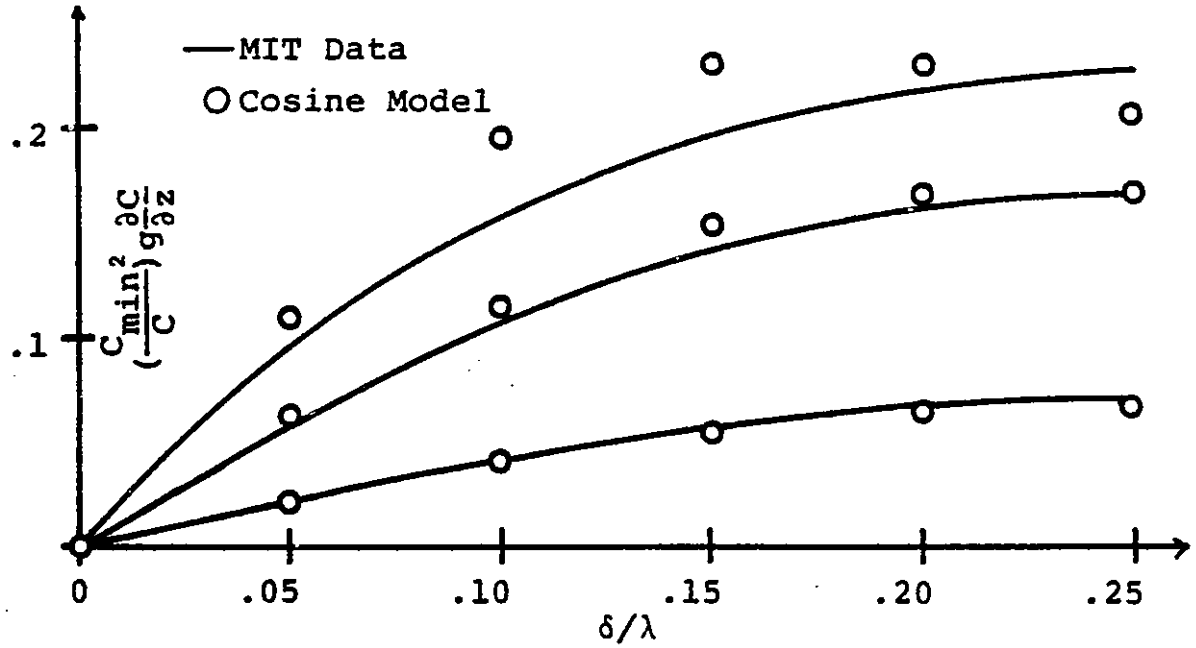

As expected, the cosine model is most accurate for small values of λ/g.

* J. Walowit, Mechanical Technology, Inc.

IV. PASSIVE STABILIZATION

No magnetic levitation system can have a stable equilibrium position without some form of current feedback [7,18]. Traditional methods for achieving this were discussed in the introductory chapter. Of concern in this chapter are techniques for providing the current feedback through proper placement of conductors in the existing levitation field. Since these methods require no external circuitry, and operate with essentially total reliability, they are referred to here as passive stabilization mechanisms.

After briefly examining several concepts for providing passive stabilization, most were discarded as introducing excessive power dissipation. One of these options, which might find some future application, is the null-flux system described in section 4E. In an effort to find a topology with low power dissipation, a scheme referred to here as homopolar stabilization emerged as a very promising alternative.

The basic concept of the homopolar design is that conductors placed on the rotor will see a constant magnetic field as long as the rotor is centered. This situation is pictured in figure 4.1a. No current flows and no power is dissipated. As soon as the rotor is displaced from center, the situation of figure 4.1b arises. The magnetic field is stronger on the side of the gap where the rotor is closest to the stator, and weaker where the gap has widened. The

Figure 4.1

a. CENTERED HOMOPOLAR ROTOR

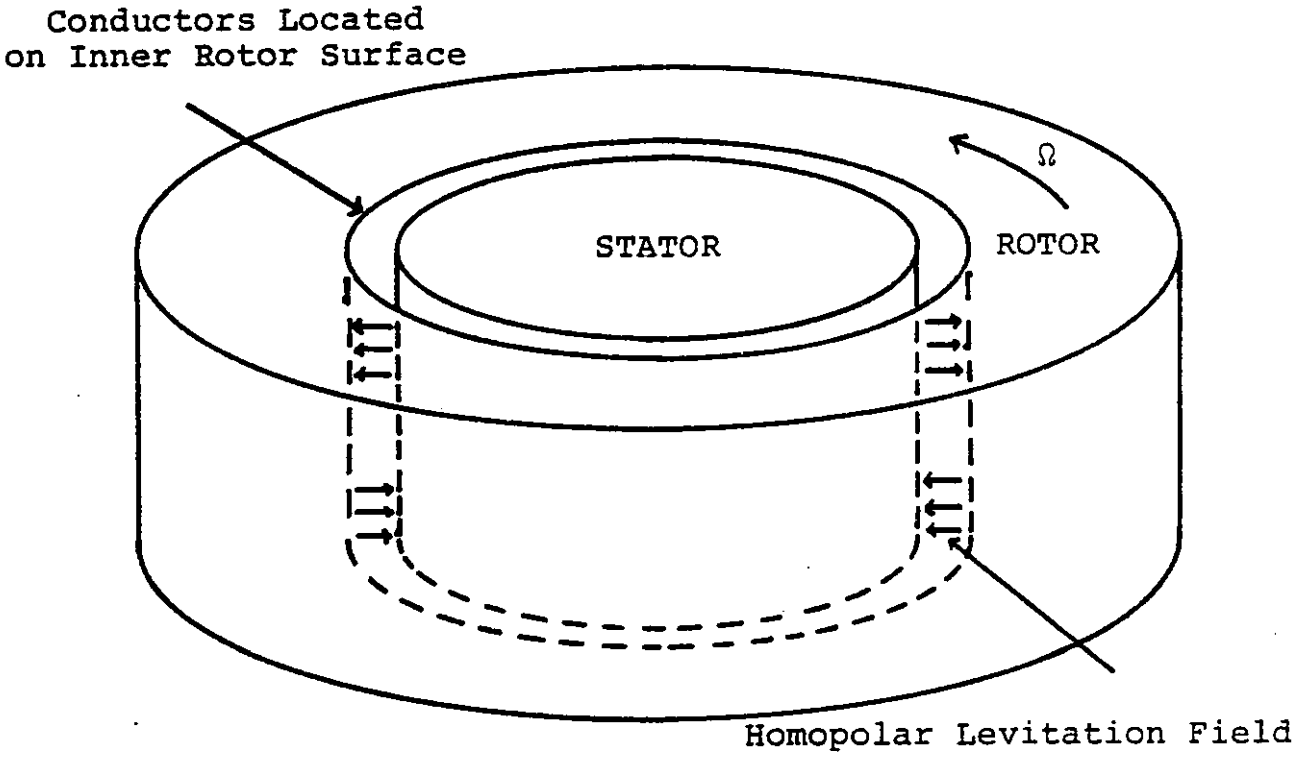

b. DISPLACED HOMOPOLAR ROTOR

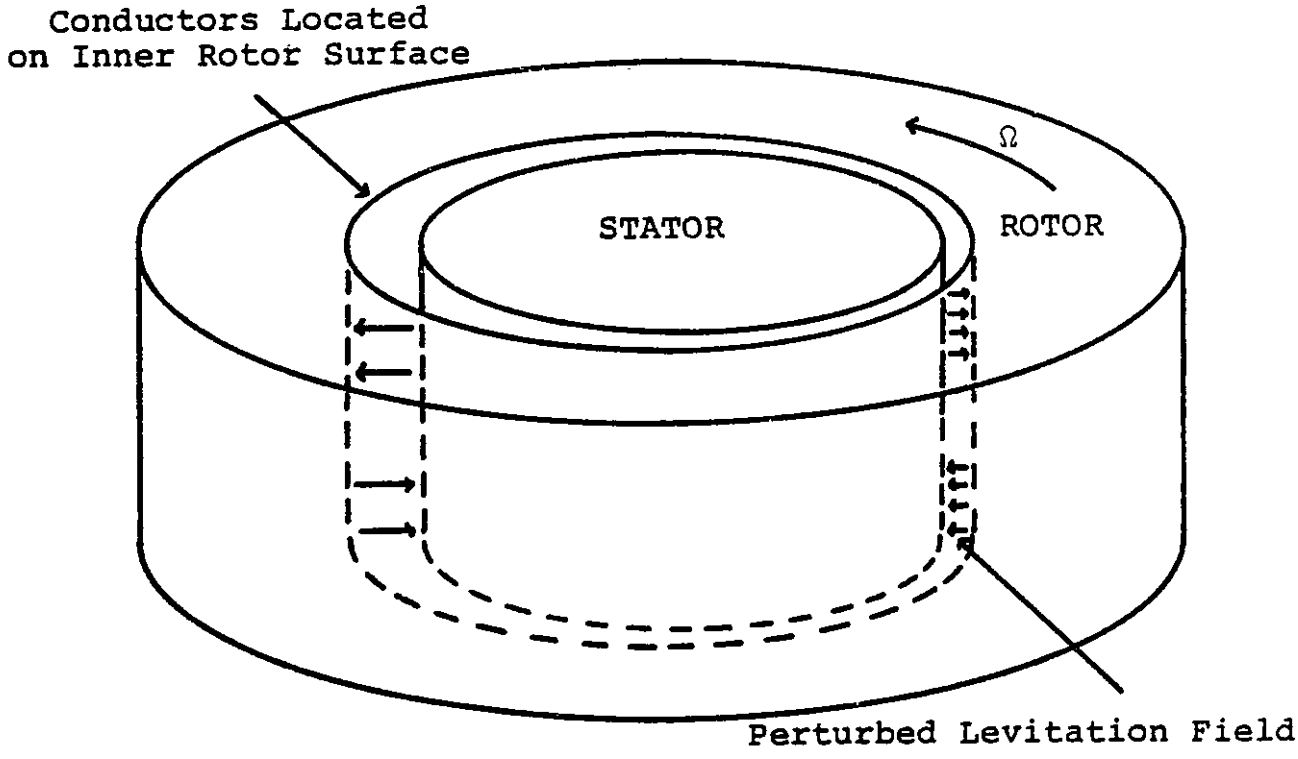

conductors spinning around with the rotor see this variation in field. The alternating flux induces current to flow in the conductors, which then reacts back on the field to create forces which cause a return to the equilibrium position. Above some critical speed, then, the system is self-stabilizing.

Three different approaches to solving for the important parameters of such a system are presented in sections B, C, and D. Each one adds new information to aid in estimating the characteristics of complicated homopolar stabilization geometries. Effects of conductor thickness, finite iron permeability, toothed gap structure, and discrete conductors are all considered using appropriate models.

A. Solution Techniques

Magnetic field problems in passive stabilization situations are complicated by the fact that it is the induced currents which are entirely responsible for the forces in the system. As a result, many simplifying assumptions cannot be used because they eliminate the primary values of interest. In order to avoid unnecessary confusion in the solution of these problems, some techniques which simplify the process have been used. These methods are described in detail by Melcher [47], but the essential aspects will be presented in this section.

a. Transfer Relations

Many electromagnetic field problems involve regions of uniform properties pieced together in simple geometries for which analytical field solutions are possible. Once the correct field solution is identified, the problem reduces to a matter of matching appropriate boundary conditions. Because of this, it is possible to solve a few simple field problems, express the results in terms of the boundary parameters, and in the future use these relationships directly. Since these equations will relate boundary values on one side of a region with those on another, they are referred to as transfer relations, and are conveniently presented in matrix form.

The first step in obtaining the transfer relations for a particular geometry is to solve the governing differential equation for the fields. For quasi-static magnetic systems, these are Faraday's law, Ohm's law, and Amperes's law with the displacement-current term removed:

$$\nabla \times \overline{E} = -\frac{\partial \overline{B}}{\partial t} \qquad \overline{J} = \sigma(\overline{E} + \overline{v} \times B) \qquad \nabla \times \overline{H} = \overline{J} \tag{4.1}$$

For regions of uniform permeability and conductivity, these equations can be combined to yield

$$\frac{1}{\mu\sigma} \nabla \times (\nabla \times \overline{B}) = -\frac{\partial \overline{B}}{\partial t} + \nabla \times (\overline{v} \times \overline{B}) \tag{4.2}$$

A vector identity allows simplification of the left side,

$$\frac{1}{\mu\sigma}\nabla^2\bar{B} = \frac{\partial\bar{B}}{\partial t} - \nabla \times (\bar{v} \times \bar{B}) \qquad (4.3)$$

Defining a vector magnetic potential,

$$\bar{B} = \nabla \times \bar{A} \qquad (4.4)$$

this equation can also be written as

$$\frac{1}{\mu\sigma}\nabla^2\bar{A} = \frac{\partial\bar{A}}{\partial t} - \bar{v} \times (\nabla \times \bar{A}) \qquad (4.5)$$

Two geometries which are of particular interest are the planar layer and the cylindrical annulus shown in figures 4.2 and 4.3. Both are two dimensional in that the same cross-section is presumed to exist for long distances in the third dimension. For these two configurations, the vector magnetic potential has only one component, in the z direction. The governing differential equation is thus reduced to only one component;

$$\frac{1}{\mu\sigma}\nabla^2 A = \frac{\partial A}{\partial t} - \left[\bar{v} \times (\nabla \times A\bar{a}_z)\right]_z \qquad (4.6)$$

For a static system or for $\sigma=0$, this expression reduces to the familiar LaPlace's equation.

For the planar layer, $v=U\bar{a}_y$, so that equation 4.6 becomes

$$\frac{1}{\mu\sigma}\nabla^2 A = \frac{\partial A}{\partial t} + U\frac{\partial A}{\partial y} \qquad (4.7)$$

Assigning phasor notation to A,

$$A = \mathrm{Re}\{\hat{A}(x)\ e^{j(\omega t - ky)}\} \qquad (4.8)$$

the expression takes the standard hyperbolic form:

Figure 4.2

Planar Layer Transfer Relations

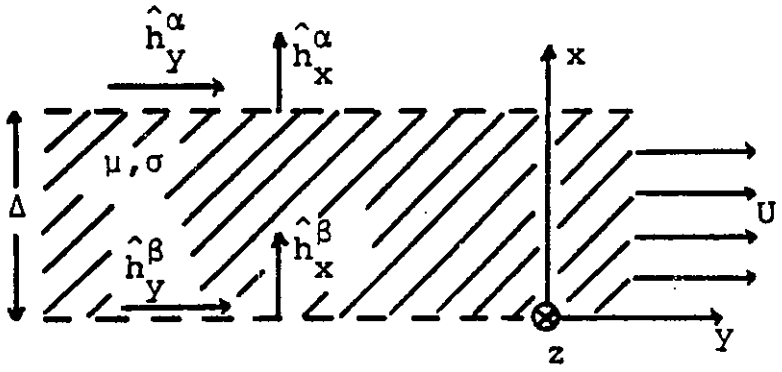

$$h=\mathrm{Re}\{\hat{h}e^{j(\omega t-ky)}\}$$

$$\begin{bmatrix}\hat{h}_y^\alpha\\ \hat{h}_y^\beta\end{bmatrix} = j\frac{\gamma}{k}\begin{bmatrix}-f & g\\ -g & f\end{bmatrix}\begin{bmatrix}\hat{h}_x^\alpha\\ \hat{h}_x^\beta\end{bmatrix}$$

$$\begin{bmatrix}\hat{h}_x^\alpha\\ \hat{h}_x^\beta\end{bmatrix} = j\frac{\gamma}{k}\begin{bmatrix}-f & g\\ -g & f\end{bmatrix}\begin{bmatrix}\hat{h}_y^\alpha\\ \hat{h}_y^\beta\end{bmatrix}$$

$$\gamma^2 = k^2 + j\mu\sigma(\omega-kU)$$

$$f = \coth(\gamma\Delta) \qquad g = \mathrm{csch}(\gamma\Delta)$$

Adapted from Melcher, Continuum Electromechanics

Figure 4.3

Rotating Annulus Transfer Relations

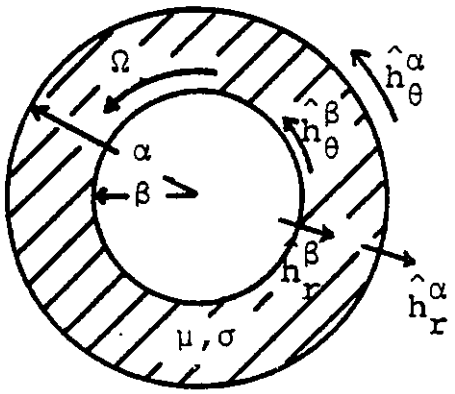

$$h = \mathrm{Re}\{\hat{h}\, e^{j(\omega t - m\theta)}\}$$

$$\gamma^2 = j\mu\sigma(\omega - m\Omega)$$

$$\begin{bmatrix} \alpha\hat{h}_r^\alpha \\ \beta\hat{h}_r^\beta \end{bmatrix} = -j\begin{bmatrix} -f & g \\ -g & f \end{bmatrix}\begin{bmatrix} \alpha\hat{h}_\theta^\alpha \\ \beta\hat{h}_\theta^\beta \end{bmatrix} \qquad \begin{bmatrix} \hat{h}_r^\beta \\ \hat{h}_r^\beta \end{bmatrix} = \begin{bmatrix} f_m(\beta,\alpha) & g_m(\alpha,\beta) \\ g_m(\beta,\alpha) & f_m(\alpha,\beta) \end{bmatrix}\begin{bmatrix} \hat{h}_\theta^\alpha \\ \hat{h}_\theta^\beta \end{bmatrix}$$

For $\gamma=0$, $m=0$;

$$f=g=\frac{1}{\ln(\alpha/\beta)}$$

For $\gamma=0$, $m\neq 0$;

$$f=\frac{(\alpha/\beta)^m + (\beta/\alpha)^m}{(\alpha/\beta)^m - (\beta/\alpha)^m} \qquad g=\frac{2}{(\alpha/\beta)^m - (\beta/\alpha)^m}$$

For $\gamma\neq 0$;

$$f_m(x,y)=\frac{\gamma y[H_m(j\gamma x)J_m'(j\gamma y) - J_m(j\gamma x)H_m'(j\gamma y)]}{m[H_m(j\gamma x)J_m(j\gamma y) - J_m(j\gamma x)H_m(j\gamma y)]}$$

$$g_m(x,y)=\frac{-2(y/x)}{m\pi[H_m(j\gamma x)J_m(j\gamma y) - J_m(j\gamma x)H_m(j\gamma y)]}$$

where primes denote derivatives with respect to $(j\gamma r)$

Adapted from Melcher, Continuum Electromechanics

$$\frac{\partial^2 \hat{A}}{\partial x^2} - \gamma^2 \hat{A} = 0; \qquad \gamma^2 = k^2 + j\mu\sigma(\omega - kU) \quad (4.9)$$

A solution which meets the boundary conditions at x=α and β is

$$\hat{A}(x) = \hat{A}^{\beta} \frac{\sinh[\gamma x]}{\sinh[\gamma \Delta]} - \hat{A}^{\alpha} \frac{\sinh[\gamma(x-\Delta)]}{\sinh \gamma\Delta} \quad (4.10)$$

A is related to B by equation 4.4,

$$\hat{B}_x = -jk\hat{A} \qquad \hat{B}_y = -\frac{\partial \hat{A}}{\partial x} \quad (4.11)$$

so that

$$\hat{B}_x = -jk\hat{A}^{\alpha} \frac{\sinh[\gamma x]}{\sinh[\gamma \Delta]} + jk\hat{A}^{\beta} \frac{\sinh[\gamma(x-\Delta)]}{\sinh[\gamma \Delta]}$$

$$\hat{B}_y = -\hat{A}^{\alpha}\gamma \frac{\cosh[\gamma x]}{\sinh[\gamma \Delta]} + \hat{A}^{\beta}\gamma \frac{\cosh[\gamma(x-\Delta)]}{\sinh[\gamma \Delta]} \quad (4.12)$$

Evaluating these expression at the two boundaries yields

$$\hat{B}_x^{\alpha} = -jk\hat{A}^{\alpha} \qquad \hat{B}_y^{\alpha} = -\gamma\hat{A}^{\alpha} \coth(\gamma\Delta) + \gamma\hat{A}^{\beta} \operatorname{csch}(\gamma\Delta)$$

$$\hat{B}_x^{\beta} = -jk\hat{A}^{\beta} \qquad \hat{B}_y^{\beta} = -\gamma\hat{A}^{\alpha} \operatorname{csch}(\gamma\Delta) + \gamma\hat{A}^{\beta} \coth(\gamma\Delta) \quad (4.13)$$

By eliminating $\hat{A}$, a relationship is drawn between the field component values at the boundaries:

$$\hat{B}_y^{\alpha} = -j\,\frac{\gamma}{k}\coth(\gamma\Delta)\hat{B}_x^{\alpha} + j\,\frac{\gamma}{k}\operatorname{csch}(\gamma\Delta)\hat{B}_x^{\beta}$$

$$\hat{B}_y^{\beta} = -j\,\frac{\gamma}{k}\operatorname{csch}(\gamma\Delta)\hat{B}_x^{\alpha} + j\,\frac{\gamma}{k}\coth(\gamma\Delta)\hat{B}_x^{\beta} \qquad (4.14)$$

These equations, written in terms of H, as well as their inverse, are given in figure 4.2.

For the rotating annulus, $\bar{v}=\Omega r\bar{a}_\theta$ so that equation 4.6 becomes

$$\frac{1}{\mu\sigma}\nabla^2 A = \frac{\partial A}{\partial t} + \Omega\,\frac{\partial A}{\partial \theta} \qquad (4.15)$$

Again using phasor notation,

$$A = \mathrm{Re}\{\hat{A}(r)\ e^{j(\omega t - m\theta)}\} \qquad (4.16)$$

this time the expression reduces to the modified Bessel's equation:

$$\frac{d^2\hat{A}}{dr^2} + \frac{1}{r}\frac{d\hat{A}}{dr} - \left[\gamma^2 + \frac{m^2}{r^2}\right]\hat{A} = 0; \qquad \gamma^2 = j\mu\sigma(\omega - m\Omega) \qquad (4.17)$$

Solutions take the form

$$\hat{A} = c_1\,J_m(j\gamma r) + c_2\,H_m(j\gamma r); \qquad \gamma \neq 0 \qquad (4.18)$$

where $H_m(x)$ is Hankel's function of the first kind. For the situations where $\gamma=0$ there are two domains. If $m=0$ then solutions take the form

$$A = c_1 \ln r + c_2; \qquad \gamma = 0,\ m = 0 \qquad (4.19)$$

while for $m \neq 0$, a different solution is required,

$$\hat{A} = c_1 r^m + c_2 r^{-m}; \qquad \gamma = 0,\ m \neq 0 \qquad (4.20)$$

Transfer relations for each of these three cases can be derived using the same procedure as before, namely:

1. $\hat{A}$ is expressed in terms of its boundary values.
2. The two field components are expressed in terms of $\hat{A}$.
3. The fields are evaluated at the boundaries.
4. $\hat{A}$ is eliminated to yield relations between the boundary field values.

The resulting transfer relations are given in figure 4.3.

b. Stress Tensor

The concept of the Maxwell stress tensor was briefly introduced in chapter 3. As it will play an essential role in the evaluation of proposed stabilizing schemes, a brief review of its origins will be presented. Only the case of linear, homogeneous regions will be considered here, although the approach can be generalized to include more complex situations [47]. The force density in such a region is

$$\overline{F} = \overline{J} \times \overline{B} \qquad (4.21)$$

Ampere's law can be used to express this entirely in terms of the fields;

$$\bar{F} = (\nabla \times \bar{H}) \times \bar{B} = \mu(\nabla \times \bar{H}) \times \bar{H} \qquad (4.22)$$

A vector identity allows this to be expressed alternatively as

$$\bar{F} = \mu(\bar{H}\cdot\nabla)\bar{H} - \tfrac{1}{2}\,\mu\nabla(\bar{H}\cdot\bar{H}) \qquad (4.23)$$

It is permissible to add $\nabla\cdot\bar{H}$ to the equation, since it equals zero;

$$\bar{F} = \mu[(\bar{H}\cdot\nabla)\bar{H} + (\nabla\cdot\bar{H})\bar{H}] - \tfrac{1}{2}\,\mu\nabla(\bar{H}\cdot\bar{H}) \qquad (4.24)$$

These two terms can both be written as a tensor divergence,

$$\bar{F} = \mu\bar{\bar{\nabla}}\cdot(\bar{H}\cdot\bar{H}) - \tfrac{1}{2}\,\mu\bar{\bar{\nabla}}\cdot(\bar{H}\cdot\bar{H})\bar{\bar{I}} \qquad (4.25)$$

where $\bar{\bar{I}}$ is the unity diagonal matrix. Grouping terms;

$$\bar{F} = \bar{\bar{\nabla}}\cdot\{\mu\bar{H}\,\bar{H} - \tfrac{1}{2}\,\mu(\bar{H}\cdot\bar{H})\bar{\bar{I}}\} \qquad (4.26)$$

This tensor in brackets is the Maxwell stress tensor for quasi-static magnetic systems under the restrictions cited [76]. Summarizing,

$$\bar{F} = \bar{\bar{\nabla}}\cdot\bar{\bar{T}} \qquad (4.27)$$

$$\bar{\bar{T}} = \mu\bar{H}\,\bar{H} - \tfrac{1}{2}\,\mu(\bar{H}\cdot\bar{H})\bar{\bar{I}} \qquad (4.28)$$

In index summation convention,

$$F_i = \frac{\partial T_{ij}}{\partial x_j} \qquad (4.29)$$

and

$$T_{ij} = \mu H_i H_j - \tfrac{1}{2} \mu \delta_{ij} H_k H_k \qquad (4.30)$$

The total force on an object due to magnetic fields is

$$\bar{f} = \int_v \bar{F}\, dV = \int_v \bar{\bar{\nabla}} \cdot \bar{\bar{T}}\, dV \qquad (4.31)$$

The divergence theorem allows this to be expressed as

$$\bar{f} = \oint_s \bar{\bar{T}} \cdot \bar{n}\, dS \qquad (4.32)$$

or in index notation,

$$f_i = \oint_s T_{ij}\, n_j\, dS \qquad (4.33)$$

c. Force and Power from Radial Fields

The dominant concern in the stabilization of radial-gap levitation schemes is the translational force and stiffness of the system. The magnetic fields are generally solved in cylindrical coordinates, however, so some manipulation of the stress tensor integral, equation 4.32, is necessary. A simple formula will be derived expressing the force directly in terms of the radial fields.

The system is assumed to have a dominant homopolar field whose magnitude at radius r_o is H_o. Perturbations in that field which lead to a net translational force will take the space-phasor form;

$$h = \mathrm{Re}\{\tilde{h}\ e^{-j\theta}\} \tag{4.34}$$

Therefore the total field can be written,

$$H_r = H_c + \mathrm{Re}\{\tilde{h}_r\ e^{-j\theta}\} = H_o + \mathrm{Re}\{\tilde{h}_r\}\cos(\theta) + \mathrm{Im}\{\tilde{h}_r\}\sin(\theta)$$
$$H_\theta = \mathrm{Re}\{\tilde{h}_\theta\ e^{-j\theta}\} = \mathrm{Re}\{\tilde{h}_\theta\}\cos(\theta) + \mathrm{Im}\{\tilde{h}_\theta\}\sin(\theta) \tag{4.35}$$

These fields can be projected onto cartesian coordinate axes,

$$H_x = H_r \cos(\theta) - H_\theta \sin(\theta)$$
$$H_y = H_r \sin(\theta) - H_\theta \cos(\theta) \tag{4.36}$$

so that

$$H_x = H_o \cos(\theta) + \mathrm{Re}\{\tilde{h}_r\}\cos^2(\theta) + \mathrm{Im}\{\tilde{h}_r\}\cos(\theta)\sin(\theta)$$
$$-\mathrm{Re}\{\tilde{h}_\theta\}\cos(\theta)\sin(\theta) - \mathrm{Im}\{\tilde{h}_\theta\}\sin^2(\theta) \tag{4.37}$$

$$H_y = H_o \sin(\theta) + \mathrm{Re}\{\tilde{h}_r\}\cos(\theta)\sin(\theta) + \mathrm{Im}\{\tilde{h}_r\}\sin^2(\theta)$$
$$+ \mathrm{Re}\{\tilde{h}_\theta\}\cos^2(\theta) + \mathrm{Im}\{\tilde{h}_\theta\}\cos(\theta)\sin(\theta)$$

From the stress tensor, equation 4.33,

$$f_x = \oint_s T_{xj}\ n_j\ dS \tag{4.38}$$

Select as the surface of integration a cylinder of radius r_o, extending the length of the system, Z, and located in the air

gap.

$$f_x = r_o Z \int_0^{2\pi} [T_{xx} \cos(\theta) + T_{xy} \sin(\theta)]d\theta \quad (4.39)$$

where

$$\begin{aligned} T_{xx} &= \mu_o H_x H_x - \tfrac{1}{2} \mu_o (H_x H_x + H_y H_y) \\ &= \tfrac{1}{2} \mu_o (H_x H_x - H_y H_y) \\ T_{xy} &= \mu_o H_x H_y \end{aligned} \quad (4.40)$$

The expansions for H_x and H_y, equations 4.37a and 4.37b, are substituted in these expressions. Only first order terms in the perturbation fields are retained, and all terms with the forms

$$\cos^2(\theta)\sin(\theta),\ \sin^2(\theta)\cos(\theta),\ \cos^3(\theta),\ \sin^3(\theta),\ \cos(\theta)\sin(\theta)$$

are neglected, since they will produce no effect upon integration over 2π. The remaining terms in the integrand are

$$\mu_o H_o [\mathrm{Re}\{\tilde{h}_r\}\cos^4(\theta) - \mathrm{Im}\{\tilde{h}_\theta\}\cos^2(\theta)\sin^2(\theta)$$

$$+ \mathrm{Re}\{\tilde{h}_r\}\cos^2(\theta)\sin^2(\theta) - \mathrm{Im}\{\tilde{h}_\theta\}\sin^4\theta]$$

Each $\cos^4\theta$ and $\sin^4\theta$ term will contribute a factor of $3\pi/4$ to the integral, while each $\cos^2\theta\sin^2\theta$ will yield a factor of $\pi/4$. Finally,

$$f_x = \pi \mu_o r_o Z H_o [\mathrm{Re}\{\tilde{h}_r\} - \mathrm{Im}\{\tilde{h}_\theta\}] \quad (4.41)$$

Another important parameter of a stabilization system is

the power dissipated in the conductors. This can be obtained by integrating $\bar{J}\cdot\bar{E}$ throughout the conductor volume. A simpler method in many cases is to find the loss directly from the fields. To do this, the torque on the rotor is found using the stress tensor method. This torque is multiplied by the rotational velocity to get the power lost from the rotor due to dissipation.

Again the system is presumed to have a dominant homopolar field of magnitude H_o at radius r_o, and perturbations such that the total fields are

$$\begin{aligned} H_r &= H_o + \mathrm{Re}\{\tilde{h}_r\}\cos(\theta) + \mathrm{Im}\{\tilde{h}_r\}\sin(\theta) \\ H_\theta &= \mathrm{Re}\{\tilde{h}_\theta\}\cos(\theta) + \mathrm{Im}\{\tilde{h}_\theta\}\sin(\theta) \end{aligned} \qquad (4.42)$$

For a symmetric stress tensor, as is here the case, the torque is

$$\bar{\tau} = \int_V \bar{r}\times\bar{F}\,dV = \oint_S \bar{r}\times(\bar{\bar{T}}\cdot\bar{n})\,dS \qquad (4.43)$$

which can be proven by expansion in cartesian coordinates. For the surface, once again choose a cylindrical one in the gap;

$$\tau = r_o \oint \bar{\bar{T}}\cdot\bar{n}\,dS = r_o^2\, Z \int_o^{2\pi} T_{\theta r}\,d\theta \qquad (4.44)$$

where $T_{\theta r}=\mu_o H_r H_\theta$. The expansions for H_r and H_θ are used in this expression, but terms of the form

$$\cos(\theta), \quad \sin(\theta), \quad \sin(\theta)\cos(\theta)$$

are dropped as they form no contribution to the integral. The remaining terms in the integrand are

$$\mu_o[\mathrm{Re}\{\tilde{h}_r\}\mathrm{Re}\{\tilde{h}_\theta\}\cos^2(\theta) + \mathrm{Im}\{\tilde{h}_r\}\,\mathrm{Im}\{\tilde{h}_\theta\}\sin^2(\theta)]$$

Integration yields

$$\tau = \pi\mu_o r_o^2 Z\, \mathrm{Re}\{\tilde{h}_r\tilde{h}_\theta^*\} \tag{4.45}$$

Thus the power dissipation is

$$P_D = \tau\Omega = \pi\mu_o r_o^2 Z\, \Omega\, \mathrm{Re}\{\tilde{h}_r\tilde{h}_\theta^*\} \tag{4.46}$$

B. Homopolar - Thin Sheet Approximation

The homopolar stabilization scheme will be solved first in the axisymmetric configuration shown in figure 4.4. The thin sheet at radius R_3 is considered to be the only conductive material in the problem. The finite permeability of the iron plays an important role in the solution, so it is retained. A dominant homopolar field is present in the gap, with a magnitude H_0 at radius R_2.

In order to evaluate the effects of translational motion of the rotor with respect to the stator, a displacement ξ_o will be introduced. For convenience, the frame of reference will remain fixed to the centroid of the rotor, so that it is the stator surface at R_2 which appears to move. Only first order terms in the resulting perturbations will be retained.

Figure 4.4

HOMOPOLAR THIN-SHEET MODEL

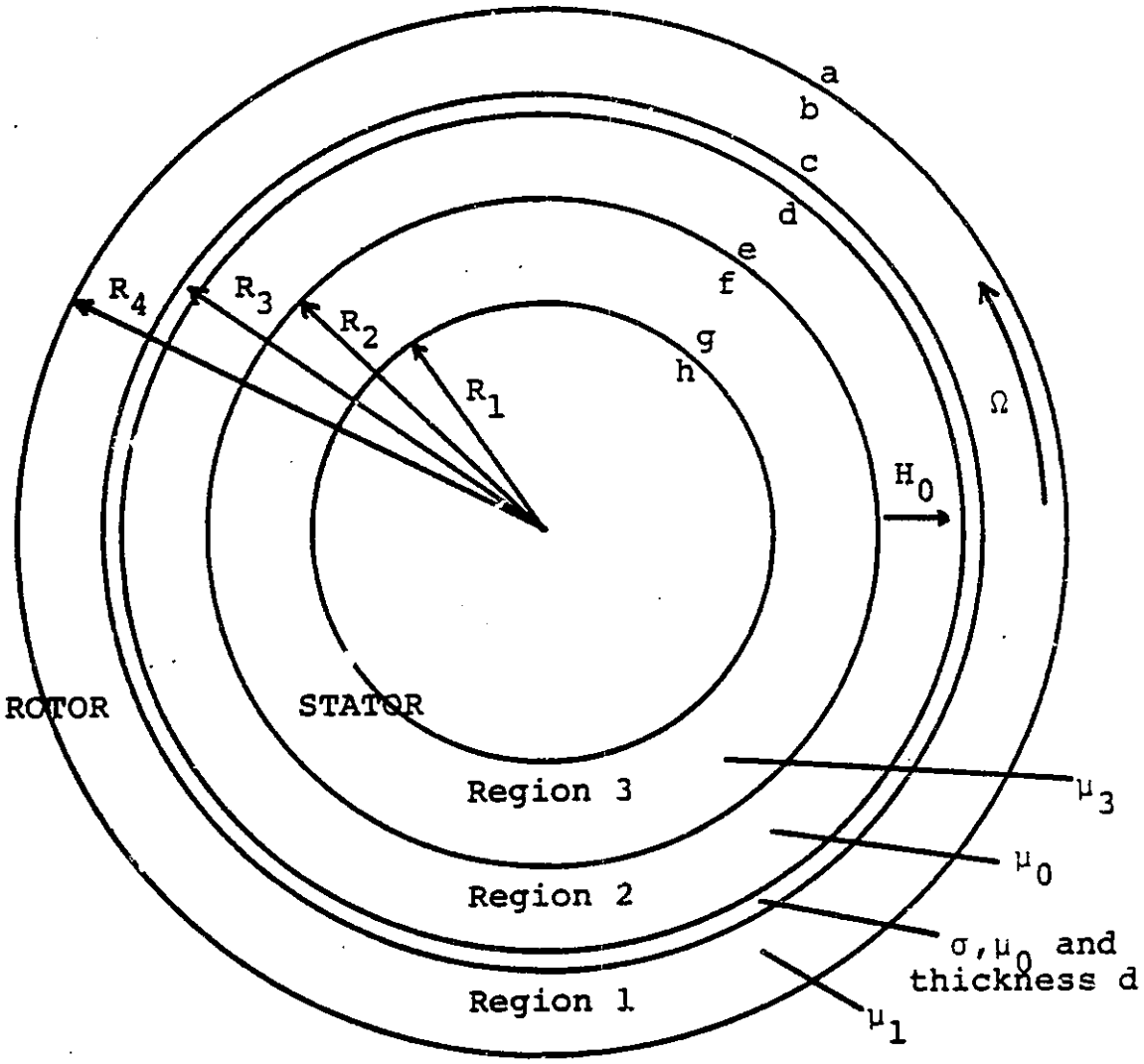

a. Stator Boundary Condition

Initially in the gap there is the homopolar field

$$\bar{H} = \frac{H_o R_2}{r} \bar{a}_r \tag{4.47}$$

The stator surface is translated an incremental amount ξ_o in the x direction. In terms of the coordinates fixed to the rotor, the stator surface is described by

$$R_2' = R_2 + \xi_o \cos(\theta) \tag{4.48}$$

The magnetic field will be perturbed by this motion, so that the total field will become

$$\bar{H}' = \frac{H_o R_2}{r} \bar{a}_r + h_r \bar{a}_r + h_\theta \bar{a}_\theta \tag{4.49}$$

At the displaced interface, Ampere's law holds so that

$$\bar{n}' \times [\bar{H}^{e'} - \bar{H}^{f'}] = 0 \tag{4.50}$$

where $\bar{n}'$ is the normal unit vector for the perturbed surface. To first order this vector is

$$\bar{n}' = \bar{a}_r - \frac{1}{R_2} \frac{\partial R_2'}{\partial \theta} \bar{a}_\theta \tag{4.51}$$

Evaluating the cross-product yields

$$h_\theta^e - h_\theta^f = - \frac{1}{R_2} \frac{\partial R_2'}{\partial \theta} H_o (1 - \mu_o/\mu_3) \tag{4.52}$$

Introduce space-phasor notation,

$$h = \mathrm{Re}\{\tilde{h}\, e^{-j\theta}\} \tag{4.53}$$

and let

$$R_2' = R_2 + \mathrm{Re}\{\tilde{\xi}_o\, e^{-j\theta}\} \tag{4.54}$$

so that the boundary condition at the e-f surface is

$$\tilde{h}_\theta^e - \tilde{h}_\theta^f = j\,\frac{\tilde{\xi}_o}{R_2}\,H_o\left(1 - \frac{\mu_o}{\mu_3}\right) \tag{4.55}$$

b. Thin-Sheet Model

The conducting sheet at radius R_3 is presumed to be sufficiently thin that currents induced in it are uniform over its cross-section. The range of validity for this assumption will be treated in section 4C. Starting with Ampere's, Faraday's, and Ohm's laws, appropriate substitutions similar to those in section 4Aa yield

$$\nabla \times \bar{J} = -\sigma\,\frac{\partial \bar{B}}{\partial t} + \sigma\nabla \times (\bar{v} \times \bar{B}) \tag{4.56}$$

Let $v=\Omega r\bar{a}_\theta$ and consider only the r component of the equation;

$$\frac{1}{r}\,\frac{\partial J_z}{\partial \theta} = -\sigma\left(\frac{\partial}{\partial t} + \Omega\,\frac{\partial}{\partial \theta}\right)B_r \tag{4.57}$$

Since current is uniform over the conductor thickness, multiplication by d yields

$$\frac{1}{R_3}\,\frac{\partial K_z}{\partial \theta} = -\sigma d\left(\frac{\partial}{\partial t} + \Omega\,\frac{\partial}{\partial \theta}\right)B_r \tag{4.58}$$

But K_z relates the jump in the tangential H field across the width of the conductor, so

$$\frac{1}{R_3}\frac{\partial}{\partial\theta}(H_\theta^c - H_\theta^d) = -\sigma d\mu_o\left(\frac{\partial}{\partial t} + \Omega\frac{\partial}{\partial\theta}\right)H_r^d \qquad (4.59)$$

In space-phasor notation and under steady-state conditions,

$$\tilde{h}_\theta^c - \tilde{h}_\theta^d = -\mu_o\sigma\, dR_3\, \Omega\, \tilde{h}_r^d \qquad (4.60)$$

Define $S=\mu_o\sigma dR_3\Omega$ as a non-dimensional speed term, so that

$$\tilde{h}_\theta^c - \tilde{h}_\theta^d = -S\, \tilde{h}_r^d \qquad (4.61)$$

is the form of the boundary condition for the thin sheet in cylindrical rotation.

c. Field Solution

To obtain field solutions for the axisymmetric thin-sheet representation, start with the transfer relations for regions 1, 2, and 3, as given in figure 4.3. The problem will be worked in steady state, so space-phasor notation is used;

$$h = \mathrm{Re}\{\tilde{h}\, e^{-j\theta}\} \qquad (4.62)$$

The appropriate transfer relations are:

$$\begin{bmatrix} R_4\,\tilde{h}_r^b \\ R_3\,\tilde{h}_r^c \end{bmatrix} = -j\begin{bmatrix} -f_1 & g_1 \\ -g_1 & f_1 \end{bmatrix}\begin{bmatrix} R_4\,\tilde{h}_\theta^b \\ R_3\,\tilde{h}_\theta^c \end{bmatrix} \quad \text{Region 1} \qquad (4.63)$$

$$\begin{bmatrix} R_2\,\tilde{h}_r^d \\ R_2\,\tilde{h}_r^e \end{bmatrix} = -j\begin{bmatrix} -f_2 & g_2 \\ -g_2 & f_2 \end{bmatrix}\begin{bmatrix} R_3\,\tilde{h}_\theta^d \\ R_2\,\tilde{h}_\theta^e \end{bmatrix} \quad \text{Region 2} \qquad (4.64)$$

$$\begin{bmatrix} R_2\,\tilde{h}_r^f \\ R_1\,\tilde{h}_r^3 \end{bmatrix} = -j \begin{bmatrix} -f_3 & g_3 \\ -g_3 & f_3 \end{bmatrix} \begin{bmatrix} R_2\,\tilde{h}_\theta^f \\ R_1\,\tilde{h}_\theta^3 \end{bmatrix} \quad \text{Region 3} \qquad (4.65)$$

where the f and g functions for the three regions are:

$$f_1 = \frac{R_4/R_3 + R_3/R_4}{R_4/R_3 - R_3/R_4} \qquad g = \frac{2}{R_4/R_3 - R_3/R_4} \qquad (4.66)$$

$$f_2 = \frac{R_3/R_2 + R_2/R_3}{R_3/R_2 - R_2/R_3} \qquad g = \frac{2}{R_3/R_2 - R_2/R_3} \qquad (4.67)$$

$$f_3 = \frac{R_2/R_1 + R_1/R_2}{R_2/R_1 - R_1/R_2} \qquad g = \frac{2}{R_2/R_1 - R_1/R_2} \qquad (4.68)$$

The transfer relations for the one-sided regions bounded by surfaces a and h are found by letting the opposite boundary radius go to infinity or zero, respectively;

$$\tilde{h}_r^a = -j\tilde{h}_\theta^a \qquad (4.69)$$

$$\tilde{h}_r^h = -j\tilde{h}_\theta^h \qquad (4.70)$$

The boundary conditions which link regions are the special two introduced in parts 4Ba and 4Bb, plus continuity of normal B and tangential H at the other surfaces:

$$\mu_1\tilde{h}_r^b = \mu_o\tilde{h}_r^a \qquad \tilde{h}_\theta^b = \tilde{h}_\theta^a \qquad (4.71)$$

$$\mu_1\tilde{h}_r^c = \mu_o\tilde{h}_r^d \qquad \tilde{h}_\theta^c = \tilde{h}_\theta^d - S\tilde{h}_r^d \qquad (4.72)$$

$$\mu_3\tilde{h}_r^f = \mu_o\tilde{h}_r^e \qquad \tilde{h}_\theta^f = \tilde{h}_\theta^e - jH_o\,\frac{\tilde{\xi}_o}{R_3}\left(1 - \frac{\mu_o}{\mu_3}\right) \qquad (4.73)$$

$$\mu_3\tilde{h}_r^g = \mu_o\tilde{h}_r^h \qquad \hat{h}_\theta^g = \tilde{h}_\theta^h \qquad (4.74)$$

where $S = \mu_o\sigma d R_3 \Omega$.

These relations constitute a system of 16 equations in 16 unknowns. To solve them, first the surface at a is eliminated by combining equations 4.69 and 4.71. Similarly, the surface h is eliminated using 4.70 and 4.74;

$$\frac{\mu_1}{\mu_o}\,\tilde{h}_r^b = -j\tilde{h}_\theta^b \qquad \frac{\mu_3}{\mu_o}\,\tilde{h}_r^g = j\tilde{h}_\theta^g \tag{4.75}$$

The b surface is dropped in favor of c using equation 4.63, while the g surface is dropped in favor of f using 4.65;

$$\tilde{h}_\theta^c = j\tilde{h}_r^c\left\{\frac{f_1 + \frac{\mu_o}{\mu_1}}{f_1\,\frac{\mu_o}{\mu_1} + 1}\right\} \qquad \tilde{h}_\theta^f = -j\tilde{h}_r^f\left\{\frac{f_3 + \frac{\mu_o}{\mu_3}}{f_3\,\frac{\mu_o}{\mu_3} + 1}\right\} \tag{4.76}$$

where use has been made of the fact that $f^2-g^2=1$. Label these two bracketed terms as X_1' and X_3'. Combining equation 4.76a with equation 4.72, and combining 4.76b with 4.73 yields

$$\tilde{h}_\theta^d = \left[j\,\frac{\mu_o}{\mu_1}\,X_1' + S\right]\tilde{h}_r^d \qquad \tilde{h}_\theta^e = -j\,\frac{\mu_o}{\mu_3}\,X_3'\tilde{h}_r^e + jH_o\,\frac{\tilde{\xi}_o}{R_3}\left(1 - \frac{\mu_o}{\mu_3}\right) \tag{4.77}$$

Define two new geometric parameters for regions 1 and 3;

$$X_1 = \frac{\mu_o}{\mu_1}\,X_1' = \frac{f_1 + \frac{\mu_o}{\mu_1}}{f_1 + \frac{\mu_1}{\mu_o}} \tag{4.78}$$

$$X_3 = \frac{\mu_o}{\mu_3}\,X_3' = \frac{f_3 + \frac{\mu_o}{\mu_3}}{f_3 + \frac{\mu_3}{\mu_o}} \tag{4.79}$$

By combining equations 4.77 and 4.64, an explicit expression for one of the field quantities is obtained:

$$\tilde{h}_r^e = \frac{H_o\,\tilde{\xi}_o/R_3\,(1 - \mu_o/\mu_3)\{[f_2 + X_1] - jS\}}{[1 + f_2(X_1 + X_3) + X_1X_3] - jS[f_2 + X_3]} \tag{4.80}$$

and from equation 4.77b;

$$\tilde{h}^{e}_{\theta} = \frac{jH_o\,\tilde{\xi}_o/R_3(1-\mu_o/\mu_3)\{[1+f_2X_1]-jSf_2\}}{[1+f_2(X_1+X_3)+X_1X_3]-jS[f_2+X_3]} \qquad (4.81)$$

The finite iron permeability was retained because it has a strong impact on the values of X_1 and X_3. However, it is still reasonable to assume that where μ_o/μ appears compared to a value of one or greater, it can be neglected. Besides the obvious term in the numerator, this includes the numerators of X_1 and X_3 such that;

$$X_1 = \frac{f_1}{f_1 + \frac{\mu_1}{\mu_o}} \qquad X_3 = \frac{f_3}{f_3 + \frac{\mu_3}{\mu_o}} \qquad (4.82)$$

If the surface of integration for the stress tensor is selected at surface e, then sufficient information is already available to evaluate both the force and power dissipation.

All of the factors which appear in these expressions are clearly defined quantities for a given system with two exceptions. One is H_o, which must be found using the magnetic circuit techniques of chapter 3. The other is the iron permeability. It is important to notice that the effect of the permeability in this problem is to reflect the response of the iron to perturbations in the field, not its response to the total field. As a result, the appropriate values of μ_1

and μ_3 are the incremental permeabilities as measured at the operating point set by the dominant homopolar field. Thus once again it is necessary to solve the magnetic circuit problem first to find the operating point. A graph showing some incremental permeabilities for typical iron materials is shown in figure 4.5.

When solving the magnetic circuit problem it is helpful to realize that the conductor does not introduce any homopolar reaction fields. Consequently, it has no effect on the total flux in the gap, and the gap reluctance can be calculated as if the conductor was not there at all.

d. Force, Stiffness, and Power

In order to obtain the translational force from equation 4.41, repeated here;

$$f_x = \pi \mu_o H_o r_o \, Z[\mathrm{Re}\{\tilde{h}_r\} - \mathrm{Im}\{\tilde{h}_\theta\}] \qquad (4.83)$$

the integration surface radius is set to surface e;

$$f_x = \pi \mu_o H_o R_2 \, Z[\mathrm{Re}\{\tilde{h}_r^e\} - \mathrm{Im}\{\tilde{h}_\theta^e\}] \qquad (4.84)$$

and the necessary field components are determined:

$$\mathrm{Re}\{\tilde{h}_r^e\} = \frac{H_o \frac{\xi_o}{R_2} \{[f_2+X_1][1+f_2(X_1+X_3)+X_1X_3]+S^2[f_2+X_3]\}}{[1+f_2(X_1+X_3)+X_1X_3]^2 + S^2[f_2+X_3]^2} \qquad (4.85)$$

$$\mathrm{Im}\{\tilde{h}^e\} = \frac{H_o \frac{\xi_o}{R_2} \{[(f_2-1)(1-X_1)][1+f_2(X_1+X_3)+X_1X_3]-(f_2-1)S^2[f_2+X_3]\}}{[1+f_2(X_1+X_3)+X_1X_3]^2 + S^2[f_2+X_3]^2}$$

Figure 4.5

INCREMENTAL IRON PERMEABILITY

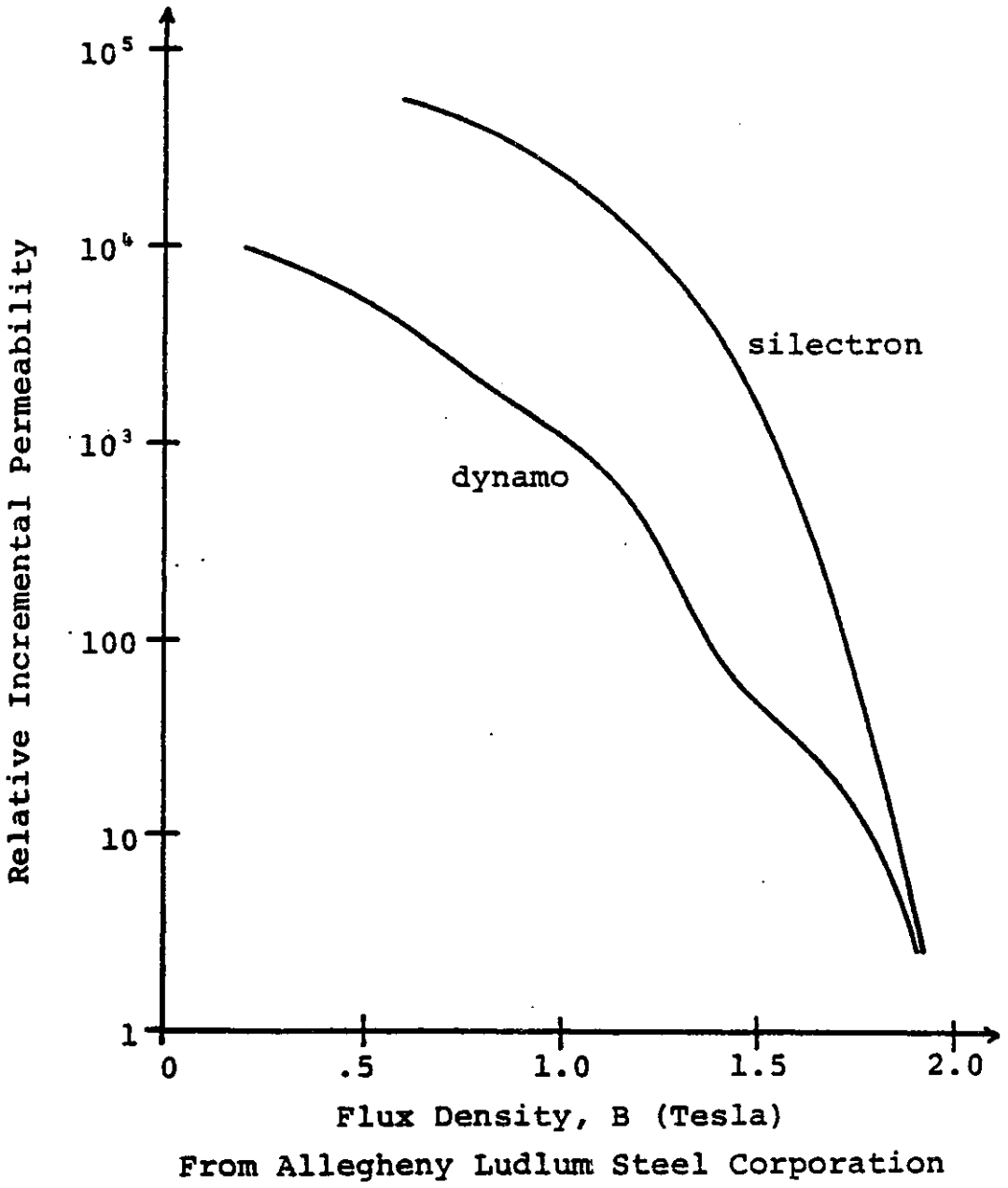

From Allegheny Ludlum Steel Corporation

Therefore,

$$f_x = \pi\mu_o Z H_o^2 \xi_o (f_2-1) \frac{\{(1-X_1)[1+f_2(X_1+X_3)+X_1X_3]-S^2[f_2+X_3]\}}{[1+f_2(X_1+X_3)+X_1X_3]^2+S^2[f_2+X_3]^2} \tag{4.86}$$

The stiffness is the change in the force due to displacement. Both ξ_o and H_o could potentially be affected by a shift in position. Fortunately, the reluctance of an annular gap is at a maximum for a centered rotor, hence its first derivative to translational motion is necessarily zero. Thus the dominant homopolar field, H_o, also has no first derivative, and

$$S_x = -\frac{\pi Z B_s^2}{\mu_o} \frac{(f_2-1)\{(1-X_1)[1+f_2(X_1+X_3)+X_1X_3]-S^2[f_2+X_3]\}}{[1+f_2(X_1+X_3)+X_1X_3]^2+S^2[f_2+X_3]^2} \tag{4.87}$$

where the gap flux at the stator has been introduced;

$$B_s = \mu_o H_o \tag{4.88}$$

As a function of speed, S, there are three values of particular interest which can be obtained from the stiffness expression. One is the stiffness as $S \to \infty$, another is the speed above which the stiffness is positive, and lastly is the stiffness when the rotor is still. For the case of $S \to \infty$, the stiffness becomes:

$$S_{x_{max}} = \frac{\pi Z B_s^2}{\mu_o} \frac{(f_2 - 1)}{(f_2 + X_3)} \tag{4.89}$$

For zero speed the stiffness represents instability,

$$S_{x_o} = - \frac{\pi Z B_s^2}{\mu_o} \frac{(f_2 - 1)(1 - X_1)}{1 + f_2(X_1 + X_3) + X_1 X_3} \tag{4.90}$$

and the speeds for which the system is stable are

$$S^2 > \frac{(1 - X_1)[1 + f_2(X_1 + X_3) + X_1 X_3]}{[f_2 + X_3]} \tag{4.91}$$

In order to obtain the power dissipation from equation 4.46, which was

$$P_D = \pi \mu_o r_o^2 \; Z \; \Omega \; \mathrm{Re}\{\tilde{h}_r \; \tilde{h}_\theta^*\} \tag{4.92}$$

the integration surface radius is again located at surface e;

$$P_D = \pi \mu_o R_2^2 \; Z \; \Omega \; \mathrm{Re}\{\tilde{h}_r^e \; \tilde{h}_\theta^{e*}\} \tag{4.93}$$

and the necessary field components found:

$$\mathrm{Re}\{\tilde{h}_r^e \; \tilde{h}_\theta^{e*}\} = H_o^2 \frac{\xi_o^2}{R_2} \frac{[f_2^2 - 1] \; S}{[1+f_2(X_1+X_3)+X_1X_3]^2 + S^2[f_2+X_3]^2} \tag{4.94}$$

By replacing Ω with its expression in terms of S, the power becomes

$$P_D = \frac{\pi Z B_s^2}{\mu_o} \frac{\xi_o^2}{\mu_o \sigma d R_3} \frac{[f_2^2 - 1] \; S^2}{[1+f_2(X_1+X_3)+X_1X_3]^2 + S^2[f_2+X_3]^2} \tag{4.95}$$

The power also approaches a saturation value as $S \to \infty$, given by

$$P_{D_{max}} = \frac{\pi Z B_s^2}{\mu_o} \frac{\xi_o^2}{\mu_o \sigma d R_3} \frac{[f_2^2 - 1]}{[f_2 + X_3]^2} \tag{4.96}$$

e. Useful Limiting Cases

For most implementations, the thickness of the gap is small compared to its radius. In this limit,

$$f_2 = \frac{R}{g}, \qquad f_2 >> 1 \tag{4.97}$$

where R is understood to be the mean radius of the gap, and $g=R_3-R_2$. This results in a significant simplification for the maximum stiffness as $S\to\infty$;

$$S_{x_{max}} = \frac{\pi Z B_s^2}{\mu_o}; \qquad R >> g \tag{4.98}$$

and the maximum power dissipation;

$$P_{D_{max}} = \frac{\pi Z B_s^2}{\mu_o} \frac{\xi_o^2}{\mu_o \sigma d R_3}; \quad R >> g \tag{4.99}$$

In both cases the effect of finite iron permeability is removed.

For parameters which continue to show the effect of finite permeability, another useful limit is to consider the relative size of μ/μ_o compared to f. In the high permeability limit where

$$\mu_1/\mu_o >> f_1; \qquad \mu_3/\mu_o >> f_3$$

the X-values take the forms

$$X_1 = \frac{f_1}{\mu_1/\mu_o} \; ; \qquad X_3 = \frac{f_3}{\mu_3/\mu_o} \tag{4.100}$$

where both are much less than one. The stiffness at zero speed becomes

$$S_{x_o} = - \frac{\pi Z B_s^2}{\mu_o} \frac{R/g}{1 + \frac{R}{g}\left(\frac{f_1}{\mu_1/\mu_o} + \frac{f_3}{\mu_3/\mu_o}\right)} \tag{4.101}$$

and the stable speeds are described by

$$S^2 > \frac{1 + \frac{R}{g}\left(\frac{f_1}{\mu_1/\mu_o} + \frac{f_3}{\mu_3/\mu_o}\right)}{R/g} \tag{4.102}$$

These expressions suggest two separate ranges of interest. Identify the first as the intermediate- permeability range, where

$$f_1 << \mu_1/\mu_o << f_1 \frac{R}{g}; \qquad f_3 << \mu_3/\mu_o << f_3 \frac{R}{g}$$

For this range of values, the stable speeds are given by

$$S^2 > \left(\frac{f_1}{\mu_1/\mu_o} + \frac{f_3}{\mu_3/\mu_o}\right) \tag{4.103}$$

The alternative is the infinite-permeability limit, where

$$\mu_1/\mu_o >> f_1 \frac{R}{g}; \qquad \mu_3/\mu_o >> f_3 \frac{R}{g}$$

In this limit, even the complete stiffness and power expressions have simple forms:

$$S_x = - \frac{\pi Z B_s^2}{\mu_o} \frac{R}{g} \frac{\left\{1 - \frac{R}{g} S^2\right\}}{\left\{1 + \left[\frac{R}{g}\right]^2 S^2\right\}} \tag{4.104}$$

$$P_D = \frac{\pi Z B_s^2}{\mu_o} \frac{\xi_o^2}{\mu_o \sigma d R_3} \frac{\left(\frac{R}{g}\right)^2 S^2}{\left\{1 + \left(\frac{R}{g}\right)^2 S^2\right\}} \qquad (4.105)$$

At the other extreme is the low-permeability limit, for which

$$\mu_1/\mu_o << f_1; \qquad \mu_3/\mu_o << f_3$$

For this limit,

$$X_1 = X_2 \simeq 1; \qquad (1 - X_1) = \frac{\mu_1/\mu_o}{f_1} \qquad (4.106)$$

so that the stable speeds are

$$S^2 > \frac{2\mu_1/\mu_o}{f_1} \qquad (4.107)$$

A graph of S^2 versus $f_1/(\mu_1/\mu_o)$ for various values of f_2 is given in figure 4.6, indicating all of these regimes. For the purposes of the graph, it is assumed that $f_1=f_3$, and $\mu_1=\mu_3$.

C. Homopolar - Finite Thickness

The objective in solving the stabilization problem with a finite-thickness conductor is to establish limits for the validity of the thin-sheet solution. As such, it is not necessary to incorporate all of the features of the system of section 4B. A simplified configuration can be used, and the

Figure 4.6

EFFECT OF IRON ON MINIMUM SPEED FOR STABILITY

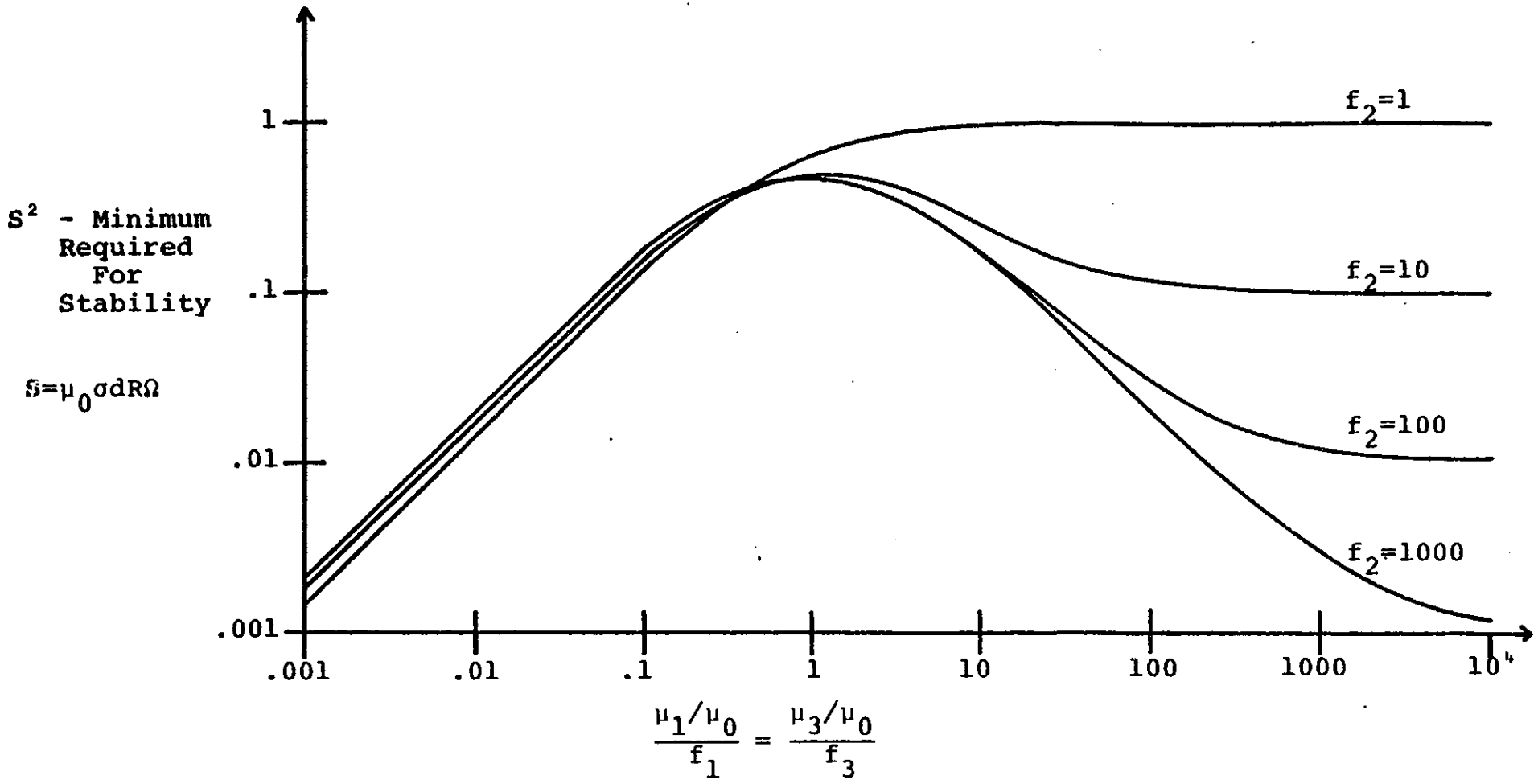

results compared to the equivalent limiting case for the thin-sheet derivation. The geometry to be solved is given in figure 4.7. A planar approximation is used, which corresponds to the case of R/g>>1. The iron is also taken as being infinitely permeable. Even with these simplifications, the thick conductor still introduces complex hyperbolic functions.

To obtain the field solution, the first step, as before, is to write down the appropriate transfer relations from figure 4.2. Space phasors are used, as defined by

$$h = \mathrm{Re}\{\tilde{h}\, e^{-jk_y}\} \tag{4.108}$$

where k=1/R. The appropriate transfer relations are:

$$\begin{bmatrix} \tilde{h}_x^a \\ \tilde{h}_x^b \end{bmatrix} = -j\,\frac{k}{\gamma}\begin{bmatrix} -f_1 & g_1 \\ -g_1 & f_1 \end{bmatrix}\begin{bmatrix} \tilde{h}_y^a \\ \tilde{h}_y^b \end{bmatrix} \quad \text{Region 1} \tag{4.109}$$

$$\begin{bmatrix} \tilde{h}_x^c \\ \tilde{h}_x^d \end{bmatrix} = -j\begin{bmatrix} -f_2 & g_2 \\ -g_2 & f_2 \end{bmatrix}\begin{bmatrix} \tilde{h}_y^c \\ \tilde{h}_y^d \end{bmatrix} \quad \text{Region 2} \tag{4.110}$$

where the f and g functions for the two regions are

$$f_1 = \coth(\gamma d) \qquad g_1 = \mathrm{csch}(\gamma d) \tag{4.111}$$
$$f_2 = \coth(kD) \qquad g_2 = \mathrm{csch}(kD)$$

and where

$$\gamma^2 = k^2\left(1 - j\,\frac{\mu_o \sigma v}{k}\right) \tag{4.112}$$

The boundary condition at surface d is set by the

Figure 4.7

THICK-SHEET MODEL

Planar Approximation

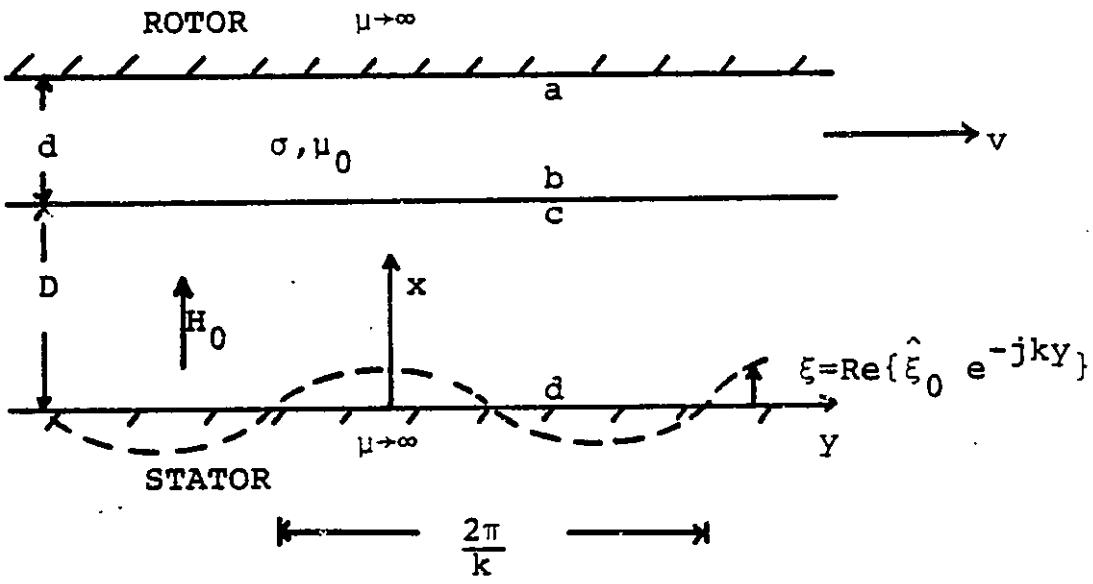

perturbation of the interface in exactly the manner described for cylindrical geometry;

$$\tilde{h}_y^d = jk\, H_o \tilde{\xi}_o \tag{4.113}$$

The remaining boundary conditions are

$$\tilde{h}_y^a = 0 \tag{4.114}$$

$$\tilde{h}_y^b = \tilde{h}_y^c \tag{4.115}$$

$$\tilde{h}_x^b = \tilde{h}_x^c \tag{4.116}$$

The result is 8 equations in 8 unknowns. Using equation 4.114, equation 4.109b becomes;

$$\tilde{h}_x^b = -j\,\frac{k}{\gamma}\, f_1 \tilde{h}_y^b \tag{4.117}$$

Equations 4.115 and 4.116 allow b to be replaced by c. Equations 4.113 and 4.110b combine to yield;

$$\tilde{h}_x^c = jf_2 \tilde{h}_y^c + g_2 k H_o \tilde{\xi}_o \tag{4.118}$$

Thus there two equations in $\tilde{h}_x^c$ and $\tilde{h}_y^c$. The solutions for the two are;

$$\tilde{h}_x^c = \frac{f_1 g_2 k H_o \tilde{\xi}_o}{f_1 + \frac{\gamma}{k} f_2} \tag{4.119}$$

$$\tilde{h}_y^c = \frac{j g_2 \gamma H_o \tilde{\xi}_o}{f_1 + \frac{\gamma}{k} f_2}$$

The force is given by equation 4.84, inserting $\tilde{h}_x^c$ for $\tilde{h}_r$,

$\tilde{h}_y^c$ for $\tilde{h}_\theta$, and using kR=1:

$$f_x = \pi\mu_o Z H_o^2 \xi_o g_2 \ \mathrm{Re}\left\{\frac{f_1 - \frac{\gamma}{k}}{f_1 + \frac{\gamma}{k} f_2}\right\} \qquad (4.121)$$

Expanding the f-functions;

$$f_x = \pi\mu_o Z H_o^2 \xi_o g_2 \ \mathrm{Re}\left\{\frac{\coth(\gamma d) - \frac{\gamma}{k}}{\coth(\gamma d) + \frac{\gamma}{k}\coth(kD)}\right\} \qquad (4.122)$$

The model is only valid in the narrow gap limit, so let R>>D. Then,

$$\sinh(kD) \approx kD; \quad \cosh(kD) \approx 1; \quad \text{making } f_2 = g_2 = \frac{1}{kD} \qquad (4.123)$$

Therefore;

$$f_x = \pi\mu_o Z H_o^2 \xi_o \ \mathrm{Re}\left\{\frac{\coth(\gamma d) - \gamma/k}{kD\coth(\gamma d) + \gamma/k}\right\} \qquad (4.124)$$

It follows as in section 4Bd that;

$$S_x = -\frac{\pi Z B_s^2}{\mu_o} \mathrm{Re}\left\{\frac{\coth(\gamma d) - \gamma/k}{kD\coth(\gamma d) + \gamma/k}\right\} \qquad (4.125)$$

The power dissipation is given by equation 4.93. Making the same substitutions as just done for the force;

$$P_D = \pi\mu_o \ Z \ \Omega \ H_o^2 \xi_o^2 g_2^2 \frac{\mathrm{Re}\left\{j \frac{\gamma}{k} \frac{1}{f_1}\right\}}{\left|1 + \frac{\gamma}{k}\frac{f_2}{f_1}\right|^2} \qquad (4.126)$$

Expanding the f and g functions under the condition that R>>D,

and replacing Ω with its expression in terms of S;

$$P_D = \frac{\pi Z B_s^2}{\mu_o} \frac{\xi_o^2}{\mu_o \sigma d R} \frac{S \, \mathrm{Re}\left\{ j \frac{\gamma}{k} \tanh(\gamma d) \right\}}{\left| kD + \frac{\gamma}{k} \tanh(\gamma d) \right|^2} \tag{4.127}$$

Consider limiting the speed so that $|\gamma d| << 1$. Then $\tanh(\gamma d) \simeq \gamma d$ and the stiffness, equation 4.125, becomes;

$$S_x = - \frac{\pi Z B_s^2}{\mu_o} \left\{ \frac{k(d+D) - (\mu_o \sigma v d)^2}{k^2 (d+D)^2 + (\mu_o \sigma v d)^2} \right\} \tag{4.128}$$

But $d+D=g$, and $\mu_o \sigma v d = \mu_o \sigma \Omega R d = S$, so:

$$S_x = - \frac{\pi Z B_s^2}{\mu_o} \frac{\left\{ 1 - \frac{R}{g} S^2 \right\}}{\left\{ 1 + \left(\frac{R}{g} \right)^2 S^2 \right\}} \tag{4.129}$$

which is exactly the result obtained in section 4Be for the narrow-gap, infinite-permeability limit, equation 4.104. Under these same conditions, the power expression becomes

$$P_D = \frac{\pi Z B_s^2}{\mu_o} \frac{\xi_o^2}{\mu_o \sigma d R} \frac{S(\mu_o \sigma v d)}{(kD+kd)^2 + (\mu_o \sigma v d)^2} \tag{4.130}$$

But again $\mu_o \sigma v d = S$ and $D+d=g$;

$$P_D = \frac{\pi Z B_s^2}{\mu_o} \frac{\xi_o^2}{\mu_o \sigma d R} \frac{\left(\frac{R}{g} \right)^2 S^2}{1 + \left(\frac{R}{g} \right)^2 S^2} \tag{4.131}$$

This is also exactly the result obtained for the thin sheet, equation 4.105. It can thus be concluded that the thin-sheet model is valid for $|\gamma d| << 1$, or effectively;

$$S << \frac{R}{d} \tag{4.132}$$

Not surprisingly, this turns out to be a statement that the magnetic skin depth must be much greater than the thickness of the conductor. Fortunately, this speed is so high that it is little or no restriction on the applicability of the thin-sheet model in actual applications.

It is interesting to consider the ultra-high-speed limit with the thick conductor. For $|\gamma d| >> 1$, $\tanh(\gamma d) \approx 1$, and

$$S_{x_{max}} = \frac{\pi Z B_s^2}{\mu_o} \qquad (4.133)$$

which is the same as the thin-sheet high-speed limit. The power, however, has a different form;

$$P_{D_{max}} = \frac{\pi Z B_s^2}{\mu_o} \frac{\xi_o^2}{\mu_o \sigma d R} \sqrt{2 S \frac{d}{R}} ; \qquad |\gamma d| >> 1 \qquad (4.134)$$

At very high speeds, the power is seen to begin to climb again with increasing speed. Thus the conclusion of this section is that the only important effect of the finite conductor thickness is to cause the power to increase for speeds where the skin depth becomes shorter than the conductor thickness.

D. Homopolar - Discrete Conductors

The geometry of the homopolar stabilization system is similar to that of an induction motor. It has long been the practice in large induction motors to place the conducting

material not as a sheet in the gap, but as a series of connected rods located in slots facing the gap. The advantages of such a scheme are a narrower gap and more rugged construction. The potential disadvantage of this scheme is the introduction of asymmetry which generates losses in the stator pole-pieces. Current paths are completed by shorting the bars together on both ends with large rings. The resulting configuration, shown in figure 4.8, is often called a squirrel-cage rotor.

The shorted bars form a large number of interconnected circuits, which could make solution quite difficult. Fortunately, if the number of bars is evenly divisible by the symmetry of the fields in the gap, then the current flowing up one bar can be matched to the current flowing down the bar directly opposite it in the ring. Because of this, each pair of opposing bars can be treated as an independent circuit.

Solution of the discrete-conductor problem is best done using lumped parameters. To emphasize the important differences between discrete and continuous conductors, the derivation will be restricted to infinite permeability and a narrow air gap. One aspect of a practical system which is well suited to this lumped-parameter method is the effect of a toothed gap on the stabilization. This influence will be evaluated in a quasi-one-dimensional fashion using the effective-gap coefficient, C, introduced in chapter 3. Consequently, the solution is appropriate only in the narrow-gap limit. This approach yields an analysis which is

Figure 4.8

SQUIRREL-CAGE ROTOR

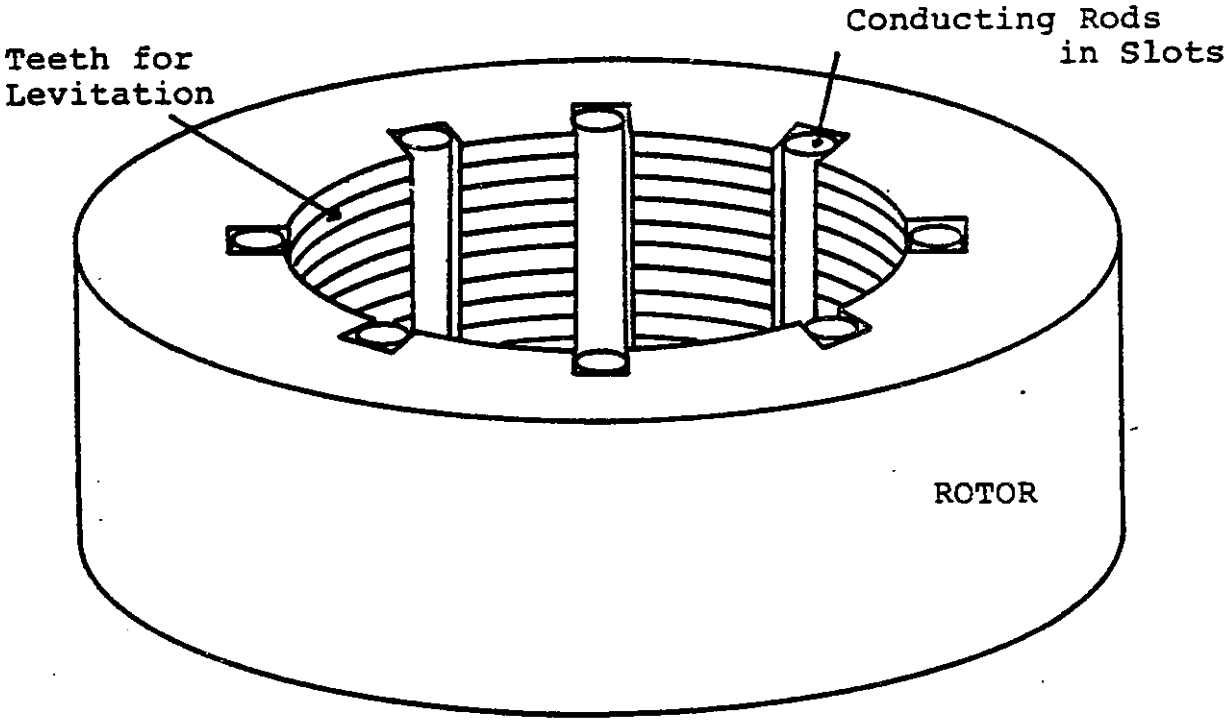

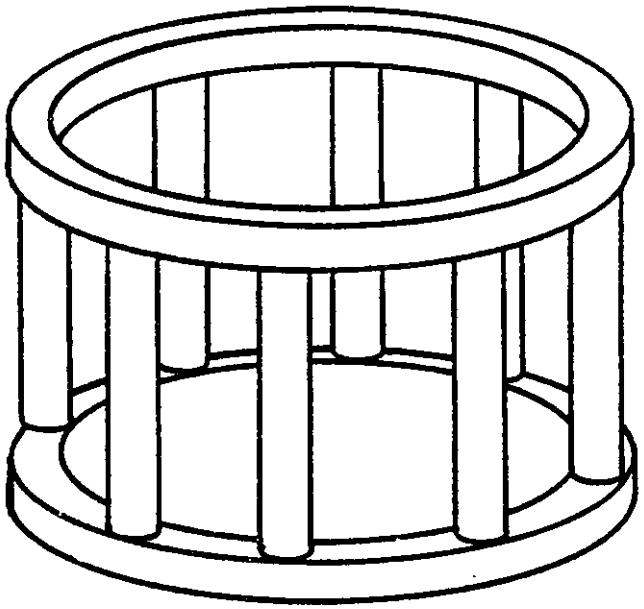

Conductor Structure
Showing End-Rings

somewhat approximate, but which provides useful results.

Initially there is a potential drop across the gap from stator to rotor of ψ_{go}. This gives rise to an average magnetic field in the radial direction of

$$\underline{H}_o = \frac{\psi_{go}}{Cg} \tag{4.135}$$

The stator is displaced an amount ξ_o in the x direction, introducing a perturbation field

$$\underline{h}_r(\theta) = - \frac{\partial H_r}{\partial x_n} \xi_o \cos(\theta) \tag{4.136}$$

where x_n is measured in the direction of increasing gap wid.

$$\underline{h}_r(\theta) = \frac{\psi_{go}}{(Cg)^2} \frac{\partial (Cg)}{\partial x_n} \xi_o \cos(\theta) \tag{4.137}$$

or

$$\underline{h}_r(\theta) = \underline{H}_o \left[\frac{\partial (Cg)}{\partial x_n}\right] \frac{\xi_o}{Cg} \cos(\theta) \tag{4.138}$$

Consider N rods equally spaced around the inner edge of the rotor such that the location of each is defined by

$$\theta_k = \Omega t + \alpha_k \tag{4.139}$$

where

$$\alpha_k = \frac{2\pi k}{N} \tag{4.140}$$

as shown in figure 4.9. The flux linked by the single-turn coil formed by rods k and k+N/2 is

$$\lambda_k = \mu_o \int_z \int_\theta h_r(\theta,z)\ r d\theta dz \qquad (4.141)$$

Let the integration over z be represented as

$$\underline{h}_r(\theta)Z = \int_z h_r(\theta,z)\ dz \qquad (4.142)$$

such that h_r represents the average perturbation field over the length Z, as defined in equation 4.138. Then

$$\lambda_k = \mu_o\ R\ Z\ \underline{H}_o\left[\frac{\partial(Cg)}{\partial x_n}\right]\ \frac{\xi_o}{Cg} \int_{\Omega t+\alpha_k-\pi}^{\Omega t+\alpha_k+\pi} \cos(\theta)d\theta \qquad (4.143)$$

or

$$\lambda_k = 2\mu_o\ R\ Z\ \underline{H}_o\left[\frac{\partial(Cg)}{\partial x_n}\right]\ \frac{\xi_o}{Cg}\ \sin(\Omega t + \alpha_k) \qquad (4.144)$$

The speed voltage becomes

$$\frac{d\lambda_k}{dt} = 2\mu_o\ R\ Z\ \underline{H}_o\left[\frac{\partial(Cg)}{\partial x_n}\right]\ \frac{\xi_o}{Cg}\ \Omega\ \cos(\Omega t + \alpha_k) \qquad (4.145)$$

Because the rods form a closed circuit,

$$\frac{d\lambda_k}{dt} + i_k \mathcal{R} = 0 \qquad (4.146)$$

where $\mathcal{R}$ is the resistance of the loop formed by two opposing rods, and i_k is the current in the kth rod. Therefore,

$$i_k = -\frac{1}{\mathcal{R}}\frac{d\lambda_k}{dt} = \frac{2\mu_o\ R\ Z\ \underline{H}_o\left[\frac{\partial(Cg)}{\partial x_n}\right]\ \xi_o\Omega}{\mathcal{R}\ Cg}\cos(\Omega t + \alpha_k) \qquad (4.147)$$

In terms of the space coordinate θ;

Figure 4.9

DISCRETE CONDUCTOR CONFIGURATION

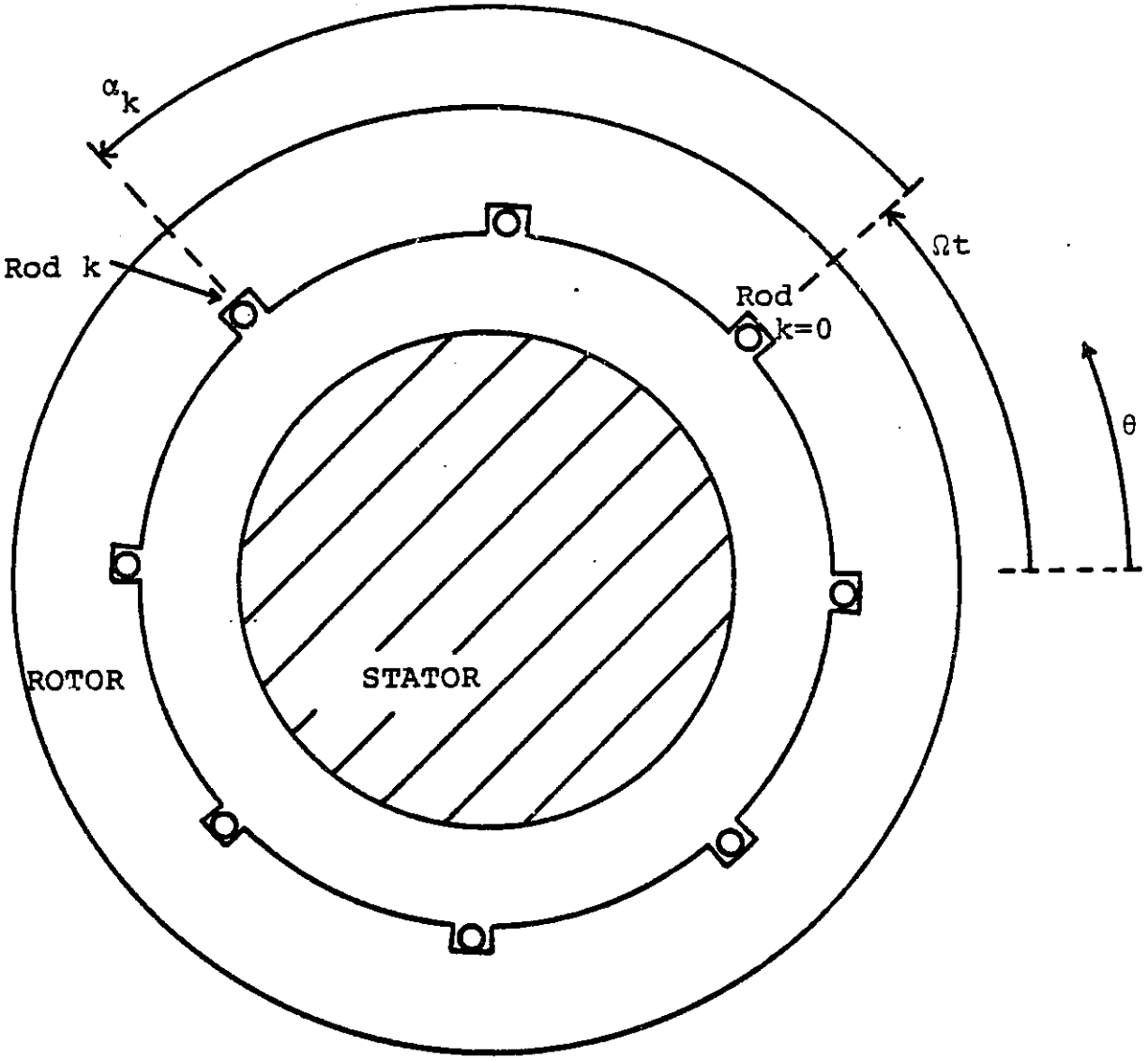

$$i(\theta) = \frac{2\mu_o R Z \underline{H}_o \left[\frac{\partial (Cg)}{\partial x_n}\right] \xi_o \Omega}{\mathcal{R} C g} \cos(\theta) \delta[\theta - (\Omega t + \alpha_k)] \quad (4.148)$$

where the Kronecker delta emphasizes that a current is present at location θ only when a conducting rod passes through that point.

The induced currents generate reaction magneto-motive forces which cause a magnetic potential to exist across the gap. The potential from stator to rotor generated at location θ due to a current at θ' and its complement at $\theta'+\pi$ is:

$$\psi'(\theta) = \begin{cases} \tfrac{1}{2} i(\theta'); & \theta < \theta' < \theta+\pi \\ \\ \tfrac{1}{2} i(\theta'); & \theta-\pi < \theta' < \theta \end{cases} \quad (4.149)$$

where infinite iron permeability has been assumed. By integrating θ' over a full π radians, the total reaction potential at θ can be found;

$$\psi'(\theta) = \int_{\theta}^{\theta+\pi} i(\theta') d\theta'$$

$$= \frac{\mu_o R Z \underline{H}_o \left[\frac{\partial (Cg)}{\partial x_n}\right] \xi_o \Omega}{\mathcal{R} Cg} \int_{\theta}^{\theta+\pi} \cos(\theta') \delta[\theta' - (\Omega t + \alpha_k)] d\theta' \quad (4.150)$$

This integral contains both a mean and a time-varying component. If there are a large number of rods, then the time-dependent part is small and the average part is well approximated by replacing the impulse function with a

spread-out version,

$$\delta[\theta' - (\Omega t + \alpha_k)] \rightarrow \frac{1}{2\pi/N}$$

since there are N rods in the range 2π. The integral is thus made trivial and

$$\psi'(\theta) = \frac{\mu_o \; R \; Z \; \underline{H}_o \left[\frac{\partial (Cg)}{x_n}\right] \; \xi_o \; \Omega \; N}{\pi \mathcal{R} \, Cg} \sin(\theta) \qquad (4.151)$$

For a given reaction potential, the average reaction field is given by

$$\underline{h}_r'(\theta) = \frac{\psi'(\theta)}{Cg} \qquad (4.152)$$

so that

$$\underline{h}_r'(\theta) = \frac{\mu_o \; R \; Z \; \underline{H}_o \left[\frac{\partial (Cg)}{\partial x_n}\right] \; \xi_o \; \Omega \; N}{\pi \mathcal{R} \, C^2 g^2} \sin(\theta) \qquad (4.153)$$

Introduce space-phasor form,

$$h = \mathrm{Re}\{\tilde{h} \; e^{-j\theta}\} \qquad (4.154)$$

so that

$$\underline{\tilde{h}}_r = \underline{H}_o \left[\frac{\partial (Cg)}{\partial x_n}\right] \frac{\xi_o}{Cg} \qquad (4.155)$$

and

$$\underline{\tilde{h}}_r' = \frac{j\mu_o \; R \; Z \; \underline{H}_o \left[\frac{\partial (Cg)}{\partial x_n}\right] \; \xi_o \; \Omega \; N}{\pi \mathcal{R} \, C^2 g^2} \qquad (4.156)$$

The reaction field can be expressed in terms of the initial field as

$$\underset{\sim}{\tilde{h}}_r' = \frac{j\mu_o \; Z \; R \; \Omega \; N}{\pi \mathcal{R} \; Cg} \underset{\sim}{\tilde{h}}_r \qquad (4.157)$$

If the reaction field was much smaller than the initial field, the problem would be finished. But if the reaction field is significant, then the original initial field was not correct, since it did not include the possibility of reaction. A corrected initial field can be used, which is the sum of the original initial field plus the reaction just calculated;

$$\underset{\sim}{\tilde{h}}_{r_{TOT}} = \underset{\sim}{\tilde{h}}_r + \underset{\sim}{\tilde{h}}_r' \qquad (4.158)$$

The reaction to this field is found in exactly the same way as before. In fact, the only difference is to replace the original field with the new total field,

$$\underset{\sim}{\tilde{h}}_r \rightarrow \underset{\sim}{\tilde{h}}_r + \underset{\sim}{\tilde{h}}_r'$$

so that the reaction field becomes, from equation 4.157;

$$\underset{\sim}{\tilde{h}}_r' = \frac{j\mu_o \; Z \; R \; \Omega \; N}{\pi \mathcal{R} \; Cg} \left(\underset{\sim}{\tilde{h}}_r + \underset{\sim}{\tilde{h}}_r'\right) \qquad (4.159)$$

In this form, the true reaction field can be determined;

$$\underline{h}_r' = \frac{\frac{j\mu_o \; Z \; R \; \Omega \; N}{\pi \mathcal{R} \; Cg} \; \underline{h}_r}{1 - \frac{j\mu_o \; Z \; R \; \Omega \; N}{\pi \mathcal{R} \; Cg}} \tag{4.160}$$

as can the true total field, $\underline{\tilde{h}}_r + \underline{\tilde{h}}_r'$;

$$\underline{\tilde{h}}_{r_{TOT}} = \frac{\underline{\tilde{h}}_r}{1 - \frac{j\mu_o \; Z \; R \; \Omega \; N}{\pi \mathcal{R} \; Cg}} \tag{4.161}$$

Identify the inductance as

$$L = \frac{\mu_o \; R \; N \; Z}{\pi \; Cg} \tag{4.162}$$

Then the familiar form results;

$$\underline{\tilde{h}}_{r_{TOT}} = \frac{\underline{\tilde{h}}_r}{1 - j\Omega L/\mathcal{R}} \tag{4.163}$$

Recalling equation 4.155, this becomes

$$\underline{\tilde{h}}_r = \frac{H_o \left[\frac{\partial (Cg)}{\partial x_r}\right] \frac{\tilde{\xi}_o}{Cg}}{1 - j\Omega L/\mathcal{R}} \tag{4.164}$$

or

$$\underline{\tilde{h}}_r = \frac{\frac{\psi_o}{Cg}\left[\frac{\partial (Cg)}{\partial x_n}\right] \frac{\tilde{\xi}_o}{Cg}}{1 - j\Omega L/\mathcal{R}} = \frac{\frac{B_g}{C\mu_o}\left[\frac{\partial (Cg)}{\partial x_n}\right] \frac{\tilde{\xi}_o}{Cg}}{1 - j\Omega L/\mathcal{R}} \tag{4.165}$$

Compare this result to the continuous-sheet case in the narrow-gap, infinite-permeability limit, taken from equation

4.80;

$$\underset{\sim}{\tilde{h}}_r^e = \frac{H_o \frac{\tilde{\xi}_o}{g}}{1 - jSR/g} \tag{4.166}$$

or

$$\underset{\sim}{\tilde{h}}_r^e = \frac{\frac{B_s}{\mu_o}\frac{\tilde{\xi}_o}{g}}{1 - \frac{j\mu_o \sigma d R^2 \Omega}{g}} \tag{4.167}$$

There are two effects present which create differences between equations 4.165 and 4.167, discrete conductors and toothed gap structure. To consider only the first effect, let C=1 in equation 4.165. Then the results are identical if

$$\frac{\Omega L}{\mathcal{R}} = \frac{SR}{g} \tag{4.168}$$

Expanding both of these expressions,

$$\frac{\Omega \mu_o RNZ\sigma A_1}{2\pi g Z} = \frac{\mu_o \sigma \Omega d R^2}{g} \tag{4.169}$$

where A_1 is the cross-sectional area of one rod. Eliminating like terms;

$$NA_1 = 2\pi\ Rd \tag{4.170}$$

But each side is just the total cross-sectional area of conductor in each system. Consequently, a discrete-conductor system can be analyzed like a continuous sheet if the conductor cross-sectional areas are the same. It is

reasonable to assume that this equivalence holds for finite permeability and wide gaps also. In determining the speed at which the power begins to increase, the skin depth should be compared to the radius of the rods, rather than to d.

The effect of toothed gap structure is not clear at this point. If the derivative term,

$$\frac{\partial (Cg)}{\partial x_n}$$

is associated with the field $\underline{H}_o$, then it will appear squared in the force expression. If it is considered to be a modification of the displacement, ξ_o, then it will only appear to the first power. One way to solve this problem is to find an expression for the force.

For slow speeds, the radial field is much larger in magnitude than the circumferential field, as indicated by equations 4.80 and 4.81. Thus the field energy can be determined in this limit by

$$W_f = \int_{V_{gap}} \tfrac{1}{2} \mu_o H^2 \, dV \qquad (4.171)$$

The homopolar field will not contribute to the force, so it is neglected such that

$$W_{f_{eff}} = \int_{V_{gap}} \tfrac{1}{2} \mu_o [Re\{\tilde{\underline{h}}_r \, e^{-j\theta}\}]^2 dV \qquad (4.172)$$

In the static limit, from equation 4.165,

$$Re\{\tilde{\underline{h}}_r \, e^{-j\theta}\} = \frac{B_g}{C\mu_o} \left[\frac{\partial (Cg)}{\partial x_n}\right] \frac{\xi_o}{Cg} \cos(\theta) \qquad (4.173)$$

Therefore,

$$W_{f_{eff}} = \tfrac{1}{2}\,\mu_o\, Z\, R\, Cg\, \frac{B_g^2}{C^2\mu_o^2}\left[\frac{\partial(Cg)}{\partial x_n}\right]^2 \frac{\xi_o^2}{C^2 g^2}\,\pi \qquad (4.174)$$

and

$$f_x = \frac{\pi Z B_g^2}{\mu_o C^2}\,\frac{R}{Cg}\left[\frac{\partial(Cg)}{\partial x_n}\right]^2 \xi_o \qquad (4.175)$$

Compare the field and force equations with and without the effective-gap coefficient in the limit of zero speed and infinite permeability:

Smooth Gap	Toothed Gap	
$\tilde{h}_r = \frac{B_s \xi_o}{\mu_o g}$	$\tilde{h}_r = \frac{B_g \xi_o}{\mu_o Cg}\left[\frac{1}{C}\,\frac{\partial(Cg)}{\partial x_n}\right]$	(4.176)
$f_x = \frac{\pi Z B_s^2}{\mu_o}\,\frac{R}{g}\,\xi_o$	$f_x = \frac{\pi Z B_g^2}{\mu_o}\,\frac{R}{Cg}\left[\frac{1}{C}\,\frac{\partial(Cg)}{\partial x_n}\right]^2 \xi_o$	(4.177)

Clearly, the appropriate substitutions to include the effect of toothed gap structure are

$$B_s \rightarrow B_g\left[\frac{1}{C}\,\frac{\partial(Cg)}{\partial x_n}\right]; \qquad g \rightarrow Cg$$

Although it is not conclusive that these substitutions remain valid for finite permeability, it is expected that they will remain approximately correct. Since g has a meaningful value only in the narrow-gap limit, this solution is restricted to that regime.

E. Null-Flux Stabilization

In the course of study toward developing magnetically-levitated high-speed ground transportation, several researchers proposed a system known as the null-flux approach, shown in figure 4.10a. This concept was first proposed by Danby and Powell in 1969, and was noted for its high stiffness and low power dissipation [13]. Although high stiffness was considered undesirable in a transportation system, the attributes of this scheme appear very suitable for flywheel magnetic bearing stabilization.

Although the null-flux system was designed originally to provide a stable lift force, it also has high stiffness under no-load conditions. In this case, the conductor remains centered along the field's plane of symmetry. In this position the field is almost entirely in the direction of motion, so that $v \times B$ is nearly zero. As a result, very little current flows and if the conductor is quite thin then the power dissipation becomes negligible. Any displacement away from the symmetry plane, however, moves the conductor into a region of alternating transverse fields. This induces currents which create restoring forces. The capabilities of the null-flux concept are best utilized if permanent magnets are used to provide the lift force and the conducting sheet serves only to stabilize the system.

In order to estimate the potential of the null-flux

Figure 4.10

NULL-FLUX

a. As Proposed for Vehicle Levitation

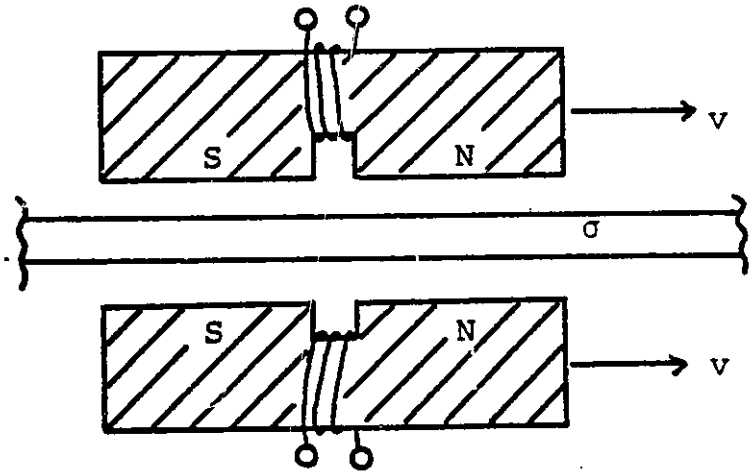

b. Field Solution Configuration

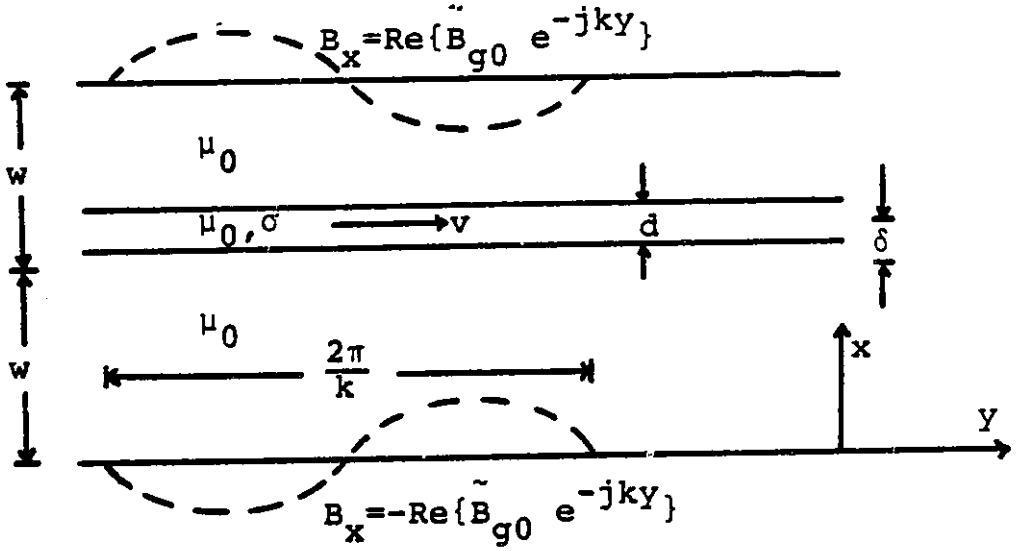

concept, the model shown in figure 4.10b was used to solve for the force and power dissipation as a function of displacement, δ, for various sets of the parameters w, d, σ, and v. The imposed boundary condition was a sinusoidal x-directed magnetic field on the boundaries. The fields were solved assuming a thick conductor using transfer relations similar to the method of section 4C. The complex hyperbolic functions required computer analysis. A large number of parameter combinations were evaluated in this manner. Typical force and power dissipation curves are shown in figure 4.11. Review of the data generated showed that the situations with the best performance corresponded to

$$|\gamma d| << 1$$

where

$$\gamma^2 = k^2\left(1 - j\,\frac{\mu_o \sigma v}{k}\right) \qquad (4.178)$$

Just as in section 4C, this corresponds to a statement that the magnetic skin depth be much greater than the thickness of the conductor. The range of interest is thus seen to correspond to the thin-sheet model.

The boundary condition for a translating thin sheet is found analogously to section 4Ba;

$$\tilde{h}_y^b - \tilde{h}_y^c = -\mu_o \sigma v d\, \tilde{h}_x^b \qquad (4.179)$$

or

$$\tilde{h}_y^b - \tilde{h}_y^c = -s\tilde{h}_x^b \qquad (4.180)$$

Figure 4.11a

NULL-FLUX STIFFNESS

d = 1mm, w = 1cm, B_{g0} = .5T, Copper sheet

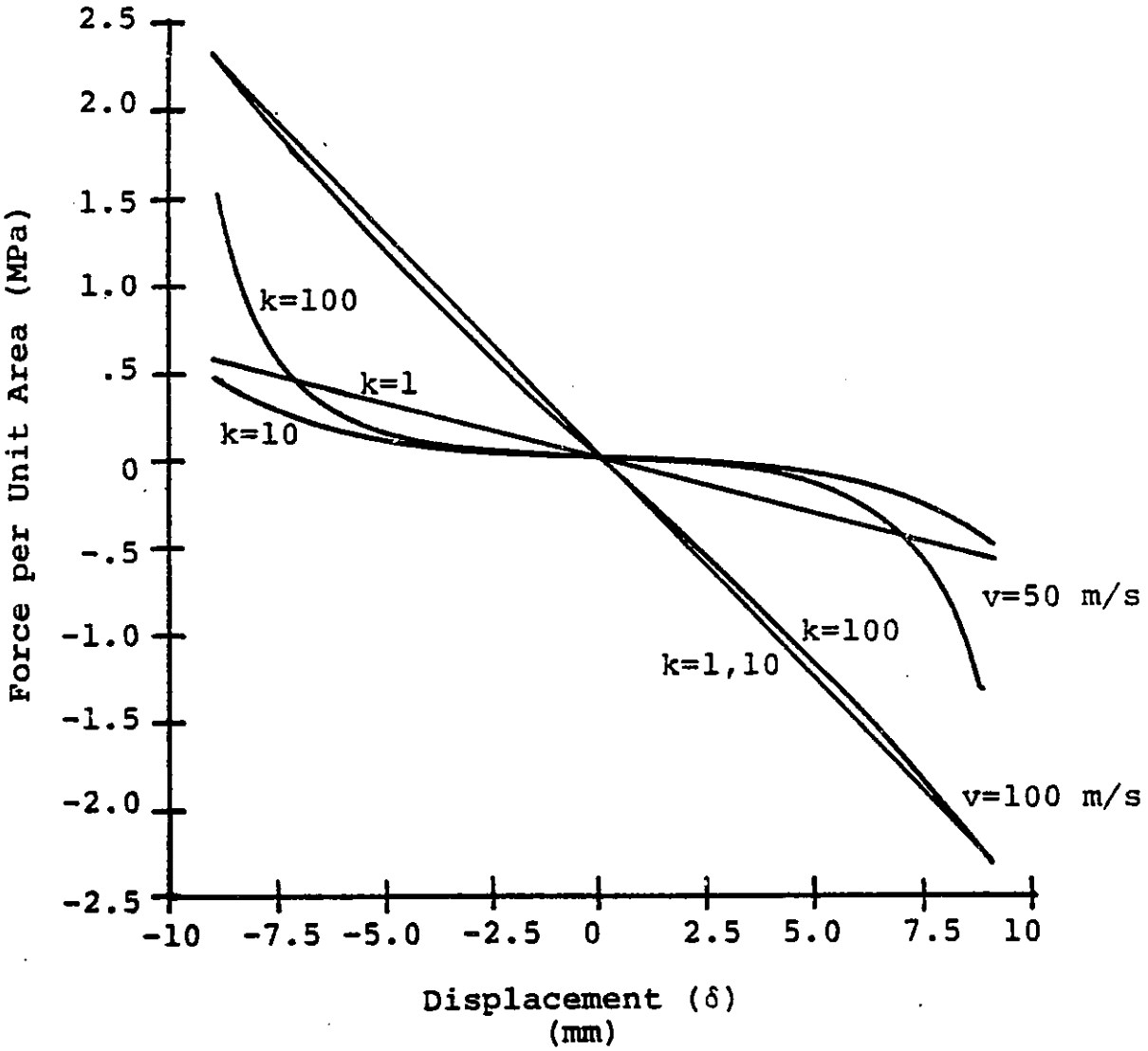

Figure 4.11b

NULL-FLUX POWER DISSIPATION

d = 1mm, w = 1cm, B_{g0} = .5T, Copper sheet

v = 100 m/s

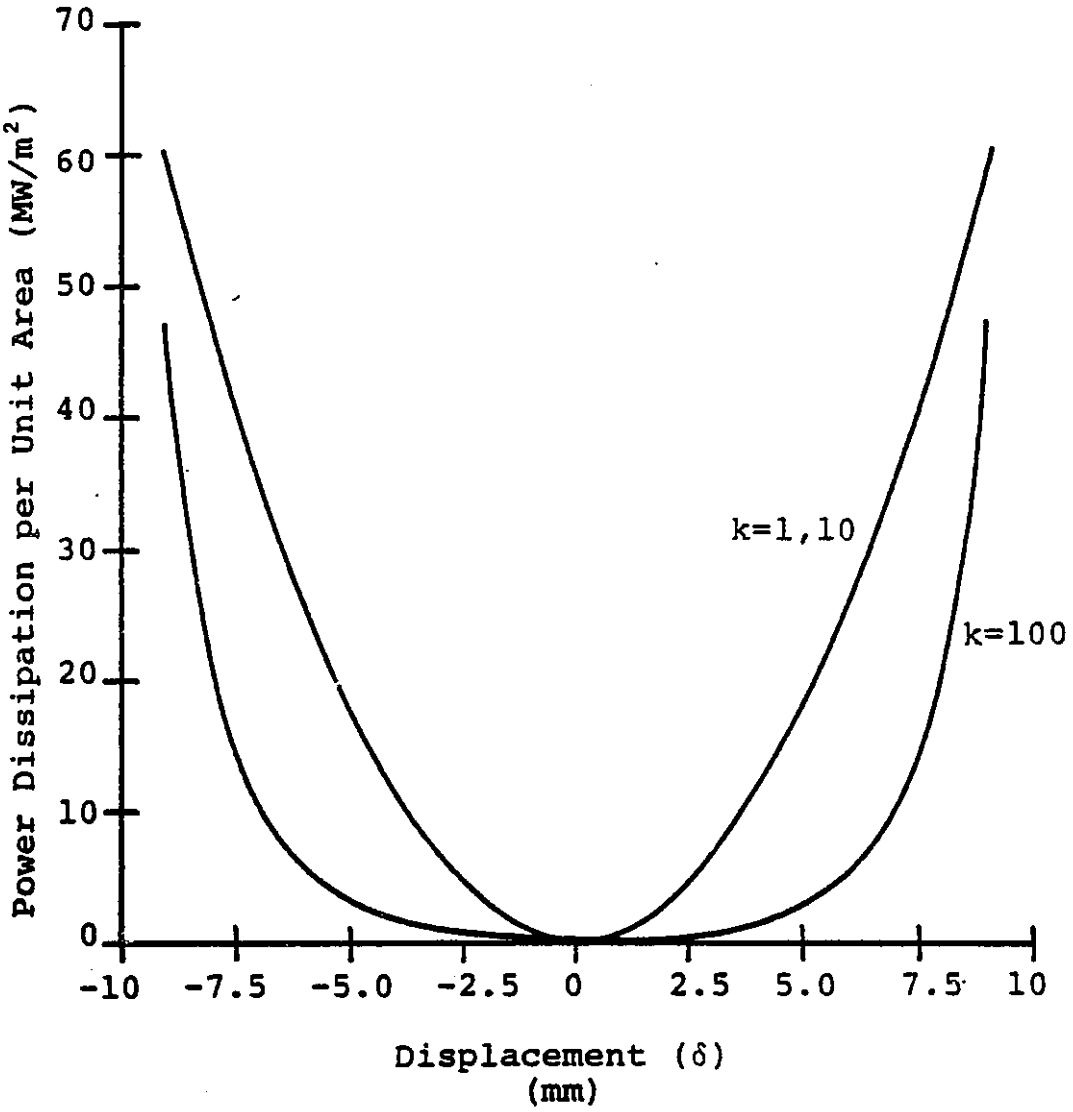

Using the transfer relations from figure 4.2, and the boundary conditions that

$$\tilde{h}_x^a - \tilde{h}_x^d = \tilde{H}_o \qquad \tilde{h}_x^b = \tilde{h}_x^c \tag{4.181}$$

then the fields can be determined. Using equation 4.33, the force and power dissipation become

$$f_x = \frac{\frac{1}{4}\mu_o H_o^2 S^2 \{\operatorname{csch}^2[k(w-\delta)] - \operatorname{csch}^2[k(w+\delta)]\} A_s}{\{\coth[k(w-\delta)] + \coth[k(w+\delta)]\}^2 + S^2} \tag{4.182}$$

$$P_D = \frac{\frac{1}{2}\mu_o H_o^2 S^2 \{\operatorname{csch}[k(w-\delta)] - \operatorname{csch}[k(w+\delta)]\}^2 A_s}{\mu_o \sigma d \{\coth[k(w-\delta)] + \coth[k(w+\delta)]\}^2 + S^2} \tag{4.183}$$

where A_s is the surface area of one side of the conducting sheet which is exposed to the imposed field.

The best performance in terms of high stiffness and large stiffness-to-power ratio is obtained when $kw \ll 1$. This corresponds to the narrow-gap limit in the homopolar system. In this limit;

$$f_x = \frac{1}{4}\mu_o H_o^2 A_s \frac{S^2(\delta/w)}{1 + \frac{1}{4}S^2(kw)^2} \tag{4.184}$$

$$P_D = \frac{\frac{1}{2}\mu_o H_o^2 A_s}{\mu_o \sigma d} \frac{S^2(\delta/w)^2}{1 + \frac{1}{4}S^2(kw)^2} \tag{4.185}$$

Both of these parameters saturate at high speed as they did in the homopolar scheme, to give

$$S_{x_{max}} = \frac{B_{go}^2 A_s}{\mu_o k^2 w^3} \tag{4.186}$$

$$P_{D_{max}} = \frac{2B_{go}^2 A_s \delta^2}{\mu_o^2 \sigma d k^2 w^4} \qquad (4.187)$$

where $B_{go}=\mu_o H_o$.

One important aspect of the situation which was eliminated in using the thin-sheet approximation was the power dissipated when $\delta=0$ due to the finite thickness of the conductor. Miericke and Urankar have shown that this term is [71]:

$$P_{Do} = \frac{B_{go}^2 A_s S^2 d}{24\ \mu_o^2 \sigma w^2} \qquad (4.188)$$

From equation 4.184, some minimum value of S^2 is necessary to supply enough stabilization to overcome the destabilizing forces induced by the levitation system. But for a given value of S^2, the steady-state power dissipation, P_{Do}, is proportional to d while the displacement power behaves inversely with d. Therefore, efforts to decrease the steady power increase the displacement power.

The stiffness of a levitation system using axial opposing flat plates is, from chapter 3;

$$S_z \approx \frac{f_z}{g} \qquad (4.189)$$

Using this value to find a minimum stabilizing stiffness for

the null-flux system, the relationship between steady and displacement power can be expressed as

$$P_D = \frac{f_z^2[1 + \frac{1}{4} S^2 (kw)^2]}{3(\mu_o \sigma g)^2 P_{Do}} \left(\frac{\delta}{w}\right)^2 \qquad (4.190)$$

The power is least when Skw<<2 such that

$$P_D = \left(\frac{f_z}{g}\right)^2 \frac{1}{3(\mu_o \sigma)^2 P_{Do}} \left(\frac{\delta}{w}\right) \qquad (4.191)$$

The gap width, g, varies only slowly with lift force, but the allowable power, P_{Do}, is likely to be linearly proportional to the force. Hence the displacement power is nearly proportional to the lift force, and not much advantage is seen for either very large or very small applications. As an example, consider a 1000 kg rotor with a 1 mm air gap and allowable steady dissipation of 100 watts. For displacements δ/w of only 1%, the power dissipation is a whopping 6000 watts.

The problem of excessive power dissipation under conditions of displacement, combined with the difficulty of creating an alternating flux field using permanent magnets, makes the null-flux scheme of limited use for magnetic bearing stabilization.

V. SYSTEM SUMMARY

The principles of magnetic levitation have been presented along with the important aspects of effective flywheel design. A method for passively stabilizing the levitation system was proposed which permits the use of a radial-gap motor-generator with the efficient multi-rim rotor configuration. It is now necessary to tie the flywheel, levitation, and stabilization subsystems together into a practical, unified design, and evaluate the resulting performance.

To completely determine the capabilities of passive stabilization, and the homopolar scheme in particular, would require several experimental tests of the theories herein proposed, and a great deal more work in comparative design analysis. Consequently, the treatment offered in this chapter represents only a speculation on the form that a practical system might take. The larger problem of thorough evaluation will constitute the basis of continuing work on this project.

The initial design target has been the storage needs of an individual residence. In section A scaling laws are derived which not only clarify the interdependence of the flywheel, levitation, and stabilization subsystems, but which indicate the applicability of the proposed design to a wide range of energy storage needs. In section B, a sample bearing is presented and evaluated, and section C concludes with a short discussion of the topics which need further

investigation.

A. Scaling Laws

Under consideration is a radial-gap magnetically-levitated multi-rim flywheel. The rotor will be assumed to have one of the cost-effective designs presented in chapter 2. Important aspects of all three subsystems will be expressed in terms of the energy storage capacity of the system. It is important to realize that the formulas derived include numerous approximations and assumptions which must be considered. Although not all of these statements apply to every result, the formulas are all valid under these conditions:

1. Narrow-gap limit
2. Inner rotor surface is set for 200 m/s.
3. The ratio of inner-to-outer rotor radius is small.
4. The rotational velocity is limited by the stress in the outermost ring, which is thin.
5. Expansion of the rotor pole piece is constrained by an alloy-steel ring.

The resulting expressions are only intended as a design guide, and not as fundamental performance restrictions or analysis tools. The scaling behavior for various aspects of the system is presented in figure 5.1. The behavior given is restricted to a range of storage capacities determined on the

Figure 5.1

SCALE DEPENDENCE FOR PASSIVELY-STABILIZED MAGNETIC LEVITATION

Symbol	Description	Nominal Value*	$\sim E^n$
b	outer rotor radius	.46 m	$\frac{1}{3}$
h	rotor height	.69 m	$\frac{1}{3}$
g	gap width	.75 mm	$\frac{1}{3}$
R	inner rotor radius	.15 m	$\frac{1}{3}$
V_c	volume in stator core	.05 m^3	1
A_i	area on inner rotor surface	.65 m^2	$\frac{2}{3}$
V_{m-g}	volume required for motor-generator	.03 m^3	$\frac{4}{3}$
V_m	volume of magnets required	.003 m^3	$\frac{4}{3}$
A_{g_T}	total gap area for levitation	.15 m^2	1
S_x max	translational stiffness at full speed	.3 N/μm	$\frac{2}{3}$
$\omega_o/2\pi$	fundamental translational mode frequency	2.9 Hz	$-\frac{1}{6}$
P_d	power dissipation due to precession	.1 W	$\frac{2}{3}$
$\Omega_{stable}/2\pi$	minimum speed necessary for stability	18 Hz	$-\frac{2}{3}$
$\Omega_{max}/2\pi$	maximum rotor speed	210 Hz	$-\frac{1}{3}$
ξ_c/g	displacement due to precession	.05	0

*based on: E-glass rotor, ceramic magnets, 10^8J capacity, $h/b=1.5$, $f_1=.15$, $f_2=.05$, 4340 steel retaining ring, $\eta=.75$, $R/g=200$, $A_o/(R_o g_o)=3$, $f_{1n}=.5$, $f_1=f_3=10$, $\mu_1=\mu_3=100$, $\sigma=5.8\cdot10^7$ mhos/m

high end by figure 5.2, and on the low end by equation 5.49.

a. Rotor

The mass required to store a given amount of energy using a particular rotor configuration is $M=E/E_s$. The aspect ratio of the rotor is determined by the whirl stability concerns expressed in equation 2.15. Assuming the ratio of inner-to-outer radii to be small, the outer radius can be written as

$$b = \{\pi\rho(\frac{h}{b})E_s\}^{-\frac{1}{3}} E^{\frac{1}{3}} \tag{5.1}$$

Similarly the height of the rotor is

$$h = (\frac{h}{b})\{\pi\rho(\frac{h}{b})E_s\}^{-\frac{1}{3}} E^{\frac{1}{3}} \tag{5.2}$$

In order to fully utilize the capacity of the rotor materials, the maximum speed should be determined by the outermost ring;

$$\Omega^2_{max} = (\frac{\sigma}{\rho})_{max} \frac{1}{b^2} \tag{5.3}$$

where $(\sigma/\rho)_{max}$ is the specific strength of the outermost material. Substituting for b from above:

$$\Omega_{max} = (\frac{\sigma}{\rho})^{\frac{1}{2}}_{max}\{\pi\rho(\frac{h}{b})E_s\}^{\frac{1}{3}} E^{-\frac{1}{3}} \tag{5.4}$$

The moment due to earth's precession, equation 2.18,

Figure 5.2

STORAGE LIMIT FOR OPTIMUM ROTOR DESIGN

Rotor Configuration	Magnet Type	V_{core} (m^3)	V_{m-g} (m^3)	V_{mag} (m^3)	A_i (m^2)	A_{gT} (m^2)	E_{max} (J)
E-Glass	Ceramic	$.050(\frac{E}{E_o})$	$.030(\frac{E}{E_o})^{4/3}$	$.005(\frac{E}{E_o})^{4/3}$	$.65(\frac{E}{E_o})^{2/3}$	$.15(\frac{E}{E_o})$	$4 \cdot 10^8$
E-Glass	$SmCo_5$	$.050(\frac{E}{E_o})$	$.030(\frac{E}{E_o})^{4/3}$	$.001(\frac{E}{E_o})^{4/3}$	$.65(\frac{E}{E_o})^{2/3}$	$.15(\frac{E}{E_o})$	$4 \cdot 10^8$
E-Glass/S-Glass	Ceramic	$.025(\frac{E}{E_o})$	$.022(\frac{E}{E_o})^{4/3}$	$.003(\frac{E}{E_o})^{4/3}$	$.45(\frac{E}{E_o})^{2/3}$	$.11(\frac{E}{E_o})$	$1 \cdot 10^8$
E-Glass/S-Glass	$SmCo_5$	$.025(\frac{E}{E_o})$	$.022(\frac{E}{E_o})^{4/3}$	$.001(\frac{E}{E_o})^{4/3}$	$.45(\frac{E}{E_o})^{2/3}$	$.11(\frac{E}{E_o})$	$1 \cdot 10^8$
E/S/Kevlar	Ceramic	$.013(\frac{E}{E_o})$	$.017(\frac{E}{E_o})^{4/3}$	$.001(\frac{E}{E_o})^{4/3}$	$.30(\frac{E}{E_o})^{2/3}$	$.08(\frac{E}{E_o})$	$4 \cdot 10^7$
E/S/Kevlar	$SmCo_5$	$.013(\frac{E}{E_o})$	$.017(\frac{E}{E_o})^{4/3}$	$.000(\frac{E}{E_o})^{4/3}$	$.30(\frac{E}{E_o})^{2/3}$	$.08(\frac{E}{E_o})$	$4 \cdot 10^7$

Assumptions:

$E_o = 10^8$ Joules

$\eta = .75$

$(BH)_m$

ceramic 26 kJ/kg

$SmCo_5$ 120 kJ/kg

$\frac{h}{b} = 1.5$

$f_1 = .15$

$\frac{R}{g} = 200$

$f_2 = .05$

Material parameters as given in tables 2.9 and 2.12

$$m_o = J_p \Omega \dot{\phi} \sin(\theta) \tag{5.5}$$

can be restated without J_p if the fundamental storage equation is used:

$$E = \tfrac{1}{2} J_p \Omega^2 \tag{5.6}$$

so that

$$m_o = \frac{2E}{\Omega} \dot{\phi} \sin(\theta) \tag{5.7}$$

or

$$m_0 = 2 \left(\frac{\sigma}{\rho}\right)^{-\frac{1}{2}}_{max} \{\pi \rho \left(\frac{h}{b}\right) E_s\}^{-\frac{1}{3}} \dot{\phi} \sin(\theta) \; E^{\frac{4}{3}} \tag{5.8}$$

b. Gap Width

There are three primary factors influencing how small the air gap can be. They are thermal expansion, mechanical strain, and machining tolerance. Interestingly, the three have nearly equal effects in a radial-gap flywheel.

The magnetic structure on the rotor should be contained by a steel ring. This prevents plastic deformation of the soft permeable iron. A steel ring is preferred over an anisotropic ring since the iron will introduce an additional radial stress. This steel ring is thus the determining factor in the increase of the gap due both to thermal expansion and

centrifugal force.

The thermal expansion coefficient for an alloy steel such as 4340 is near $10^{-5}/°C$. Temperature rises of up to 100°C may by encountered, since in the vacuum all rotor dissipation must be by radiation. Thus the increase in the circumference of the inner edge of the rotor in going from a cold start to full power is

$$\Delta(2\pi R) = \alpha_T \Delta T (2\pi R) \tag{5.9}$$

where R is the radius of the gap. The radius change manifests itself as a change in the gap width

$$\Delta g = \alpha_T \Delta T \; R \approx 10^{-3} R \tag{5.10}$$

The exact radial displacement for a ring on the rotor was given in figure 2.2 If the ring is thin, as the steel retaining ring is presumed to be, then

$$\Delta g = \frac{\sigma_{steel}}{E_Y} R \tag{5.11}$$

where σ_{steel} is the circumferential stress in the steel ring and E_Y is the Young's modulus of elasticity for the material. For alloy steel, $E_Y = 200$ GPa . Since the iron is limited to a velocity of 200 m/sec, this is approximately the velocity of the steel ring. Thus from equation 2.10

$$\sigma_{steel} = \rho v^2 = 300 \text{ MPa} \tag{5.12}$$

Therefore the increase in gap width in going from a standstill

to full speed is

$$\Delta g \approx 1.5 \cdot 10^{-3} R \qquad (5.13)$$

The machining tolerance is an ambiguous function of size, shape and cost. Since both attributes of the gap so far have been proportional to the radius of the gap, a reasonable empirical formula for machining tolerance is to assume a linear dependence on radius, based on .1mm clearance at 10cm:

$$g \approx 10^{-3} R \qquad (5.14)$$

This gap represents a minimum which must be present at zero speed. The other two effects add to this at full speed, so that the total gap under full speed conditions is the sum of all three;

$$\Delta g_{TOT} \approx 3.5 \cdot 10^{-3} R \qquad (5.15)$$

To leave a margin of safety, and to minimize the proportional change in the gap with speed, let the gap at zero speed be $2.5 \cdot 10^{-3} R$, so that at full speed,

$$g = 5 \cdot 10^{-3} R \qquad (5.16)$$

To relate the gap width to the energy storage, the scale dependence of R must be determined.

c. Inner Radius

As was shown in figure 2.11, it is advantageous to select

the inner radius so that it corresponds to the maximum allowed velocity for silicon steel. Doing so completely determines the ratio of inner to outer radius for a given rotor configuration. Recognizing that the inner radius is R,

$$R = \left(\frac{R}{b}\right)b = \left(\frac{R}{b}\right)\left\{\pi\rho\left(\frac{h}{b}\right)E_s\right\}^{-1/3} E^{1/3} \tag{5.17}$$

Having selected the inner radius in this manner, an important concern is whether such a choice leaves adequate room for the motor-generator, magnets, and gap surface area. In terms of the stored energy capacity, the volume in the stator core is

$$V_c = \pi R^2 h = \frac{\left(\frac{R}{b}\right)^2}{\rho E_s} E \tag{5.18}$$

and the area on the inner surface is

$$A_i = 2\pi Rh = 2\pi\left(\frac{h}{b}\right)\left(\frac{R}{b}\right)\left\{\pi\rho\left(\frac{h}{b}\right)E_s\right\}^{-2/3} E^{2/3} \tag{5.19}$$

The size of the motor-generator is determined by its power-handling capability and the rotational speed of the flywheel. In Rockwell's IPACS study for NASA [54], the predicted volume required for a noncontacting motor-generator was

$$V_{m-g} = \frac{10^{-3} P_{out}}{\Omega} \quad m^3 \tag{5.20}$$

Take for the minimum speed one half of the maximum. The maximum output power is related to the energy storage by the time over which the energy might need to be extracted from the system;

$$P_{out} = \frac{E}{t_{discharge}} \tag{5.21}$$

For a system designed to run on a fundamental cycle of one day, the energy should be available over a span of one to two hours. t_d=5000 seconds will be assumed for numerical comparisons. Thus

$$V_{m-g} \simeq \frac{2 \cdot 10^{-3} \{\pi \rho (\frac{h}{b}) E_s\}^{-1/3}}{t_d \ (\frac{\sigma}{\rho})^{1/2}_{max}} E^{4/3} \tag{5.22}$$

The volume required to house the magnets follows from equation 3.65,

$$V_m = \frac{2 \ g \ g \ E}{(BH)_m \ \eta \ f_1 \ E_s} \tag{5.23}$$

where g is the acceleration of gravity. Replacing g by R and using equation 5.17 for R yields

$$V_m = \frac{2g (\frac{R}{b}) \{\pi \rho (\frac{h}{b}) E_s\}^{-1/3}}{(\frac{R}{g}) (BH)_m \ \eta \ f_1 \ E_s} E^{4/3} \tag{5.24}$$

The gap area required to provide the necessary lift force follows from equation 3.75,

$$A_g = \frac{\mu_o \, g}{B_g^2 \; f_2 \; E_s} E \qquad (5.25)$$

Notice, however, that the actual surface area on the rotor that is needed is actually $2A_g$, since there must be both inward and outward flux paths. This surface area required will be termed the "total gap area", given by

$$A_{gT} = \frac{2\mu_o g}{B_g^2 \; f_2 \; E_s} E \qquad (5.26)$$

The space demands for the motor-generator, magnets, and total gap area all increase faster than the available room as the energy storage capacity is raised. There exists, then, some quantity of energy storage above which the optimum rotor design cannot be maintained. Shown in figure 5.2 are the energy break-points corresponding to various rotor configurations and magnet selection. The three rotor configurations are from those indicated in figure 2.12. The substitution of steel in the innermost ring has only a minor effect.

As is apparent from this figure, the limiting effect is the motor-generator volume, which restricts most configurations to residential-sized systems or smaller. It should be noted that larger systems can be built, only that the cost-effectiveness of the rotor is decreased. So long as the energy storage capacity allows the use of an optimum rotor configuration, a formula giving the scaling of the gap width

can be deduced;

$$g = 5 \cdot 10^{-3} \left(\frac{R}{b}\right) \left\{\pi \rho \left(\frac{h}{b}\right) E_s\right\}^{-\frac{1}{3}} E^{\frac{1}{3}} \tag{5.27}$$

d. Stabilization

The maximum value for R/g was shown in part b to be 200. This clearly establishes the narrow-gap limit as the appropriate condition. Consequently, the translational stiffness at full speed, corrected to account for a toothed gap, is

$$S_{x_{max}} = \frac{\pi Z B_g^2}{\mu_o} \left[\frac{1}{C} \frac{\partial (Cg)}{\partial x_n}\right]^2 \tag{5.28}$$

or

$$S_{x_{max}} = \frac{\pi Z B_g^2}{\mu_o} f_{1n}^2 \tag{5.29}$$

Z is related to the total gap area through R,

$$A_{gT} = 2\pi RZ \tag{5.30}$$

R is given by equation 5.17, while A_{gT} is related to the energy capacity using equation 5.26, yielding

$$S_{x_{max}} = \frac{g\left\{\pi \rho \left(\frac{h}{b}\right) E_s\right\}^{\frac{1}{3}} f_{1n}^2}{\left(\frac{R}{b}\right) f_2 E_s} E^{\frac{2}{3}} \tag{5.31}$$

From this the fundamental translational-mode frequency can be

found;

$$\omega_o = \sqrt{\frac{S_x}{M}} = \left[\frac{g\{\pi\rho(\frac{h}{b})E_s\}^{1/3} f_{1n}^2}{(\frac{R}{b})\ f_2}\right]^{1/2} E^{-1/6} \qquad (5.32)$$

The power dissipation at full speed, from equation 4.99, is

$$P_{D_{max}} = \frac{\pi Z B_\sigma^2}{\mu_o} \frac{2\pi\xi_o^2}{\mu_o \sigma A_c} f_{1n}^2 \qquad (5.33)$$

or

$$P_{D_{max}} = S_{x_{max}} \frac{2\pi\xi_o^2}{\mu_o \sigma A_c} \qquad (5.34)$$

The conductor cross-sectional area, A_c, is proportional to Rg. Thus if A_0 is the area for a system with radius R_0 and gap width g_0;

$$P_{D_{max}} = S_{x_{max}} \frac{2\pi\xi_o^2}{\mu_o \sigma [\frac{Ao}{R_0 g_0}] Rg} \qquad (5.35)$$

Expressing ξ_o as a fraction of the gap width;

$$P_{D_{max}} = S_{x_{max}} \frac{2\pi(\frac{\xi_o}{g})^2}{\mu_o \sigma [\frac{A_o}{R_0 g_0}] (\frac{R}{g})} \qquad (5.36)$$

or in terms of the storage capacity

$$P_{D_{max}} = \frac{2\pi g\{\pi\rho(\frac{h}{b})E_s\}^{1/3} f_{ln}^2(\frac{\xi_o}{g})^2}{(\frac{R}{b})\ E_s\mu_o\sigma[\frac{A_0}{R_0 g_0}]\ (\frac{R}{g})\ f_2} E^{2/3} \tag{5.37}$$

Clearly ξ_o cannot be permitted to exceed g. There is also a minimum restriction on ξ_o, imposed by the earth's precession. Assume that there are two levitation structures at each end of the stator, separated by a distance h. Then the moment due to precession results in a dispacement at each end given by

$$m_0 = S_x \xi_o h \tag{5.38}$$

Substituting equations 5.8, 5.31, and 5.2 for the moment, stiffness, and height, respectively;

$$\xi_o = \frac{2(\frac{R}{b}) f_2\ E_s\ \dot{\phi}\ \sin(\theta)}{g(\frac{\sigma}{\rho})_{max}^{1/2}\{\pi\rho(\frac{h}{b})E_s\}^{1/3} f_{ln}^2(\frac{h}{b})} E^{1/3} \tag{5.39}$$

or, more importantly,

$$\frac{\xi_o}{g} = \frac{2(\frac{R}{g}) f_2 E_s\ \dot{\phi}\sin(\theta)}{g(\frac{\sigma}{\rho})_{max}^{1/2}\ f_{ln}^2\ (\frac{h}{b})} \tag{5.40}$$

which is independent of size.

The speed above which the power begins to increase above its nominal full-speed value is

$$S > \frac{R}{d} \tag{5.41}$$

where d is the narrow-conductor dimension. In terms of Ω, the expression for the continuous-sheet case is

$$\Omega_{pi} > \frac{1}{\mu_o \sigma d^2} \tag{5.42}$$

which can be applied approximately to the discrete-conductor situation as well. d is generally restricted in proportion to the gap width so that for an optimum rotor design;

$$\Omega_{pi} > \frac{1}{\mu_o \sigma (\frac{d}{g})^2 \ g^2} = \frac{(\frac{R}{g})^2 \{\pi \rho (\frac{h}{b}) E_s\}^{2/3}}{\mu_o \sigma (\frac{d}{g})^2 (\frac{R}{b})^2} E^{-2/3} \tag{5.43}$$

The ratio of this speed to the maximum speed for the rotor is

$$\frac{\Omega_{pi}}{\Omega_{max}} = \frac{(\frac{R}{g})^2 \{\pi \rho (\frac{h}{b}) E_s\}^{1/3}}{\mu_o \sigma (\frac{d}{g})^2 (\frac{R}{b})^2 (\frac{\sigma}{\rho})^{1/2}_{max}} E^{-1/3} \tag{5.44}$$

For reasonable configurations this ratio is greater than one for storage capacities up to 10^{13} Joules.

The speed above which the system is stable follows from equation 4.102,

$$s > \frac{g}{R} + \frac{f_1}{\mu_1/\mu_o} + \frac{f_3}{\mu_3/\mu_o} \tag{5.45}$$

Not much can be said about the f functions, other than the fact that they are scale-independent for a given topology, since they depend only on length ratios. In some configurations the width of the iron poles is restricted only by the available space. g/R has also been shown to be scale-independent, so in terms of Ω,

$$\Omega > \frac{2\pi\{\frac{g}{R} + \frac{f_1}{\mu_1/\mu_o} + \frac{f_3}{\mu_3/\mu_o}\}^{\frac{1}{2}}}{(\mu_o\sigma)\ A_c} \qquad (5.46)$$

Substituting for A_c as done for the power dissipation;

$$\Omega > \frac{2\pi\{\frac{g}{R} + \frac{f_1}{\mu_1/\mu_o} + \frac{f_3}{\mu_3/\mu_o}\}^{\frac{1}{2}}}{\mu_o\sigma[\frac{A_0}{R_0 g_0}]\ Rg} \qquad (5.47)$$

or

$$\Omega_s = \frac{2\pi(\frac{R}{g})\{\frac{g}{R} + \frac{f_1}{\mu_1/\mu_o} + \frac{f_3}{\mu_3/\mu_o}\}^{\frac{1}{2}}\{\pi\rho(\frac{h}{b})E_s\}^{\frac{2}{3}}}{\mu_o\sigma\ [\frac{A_o}{R_0 g_0}]\ (\frac{R}{b})^2} E^{-\frac{2}{3}} \qquad (5.48)$$

Thus the ratio of the minimum stable speed to maximum speed is

$$\frac{\Omega_s}{\Omega_{max}} = \frac{2\pi(\frac{R}{g})\{\frac{g}{R} + \frac{f_1}{\mu_1/\mu_o} + \frac{f_3}{\mu_3/\mu_o}\}^{\frac{1}{2}}\{\pi\rho(\frac{h}{b})E_s\}^{\frac{1}{3}}}{\mu_o\sigma\ [\frac{A_o}{R_0 g_0}](\frac{R}{b})^2\ (\frac{\sigma}{\rho})^{\frac{1}{2}}_{max}} E^{-\frac{1}{3}} \qquad (5.49)$$

This ratio is less than 10% for energy storage capacities in excess of roughly $5 \cdot 10^6$ Joules.

B. Sample System

a. Design

Shown in figure 5.3 is an example of a typical system

Figure 5.3

PROPOSED FLYWHEEL SYSTEM

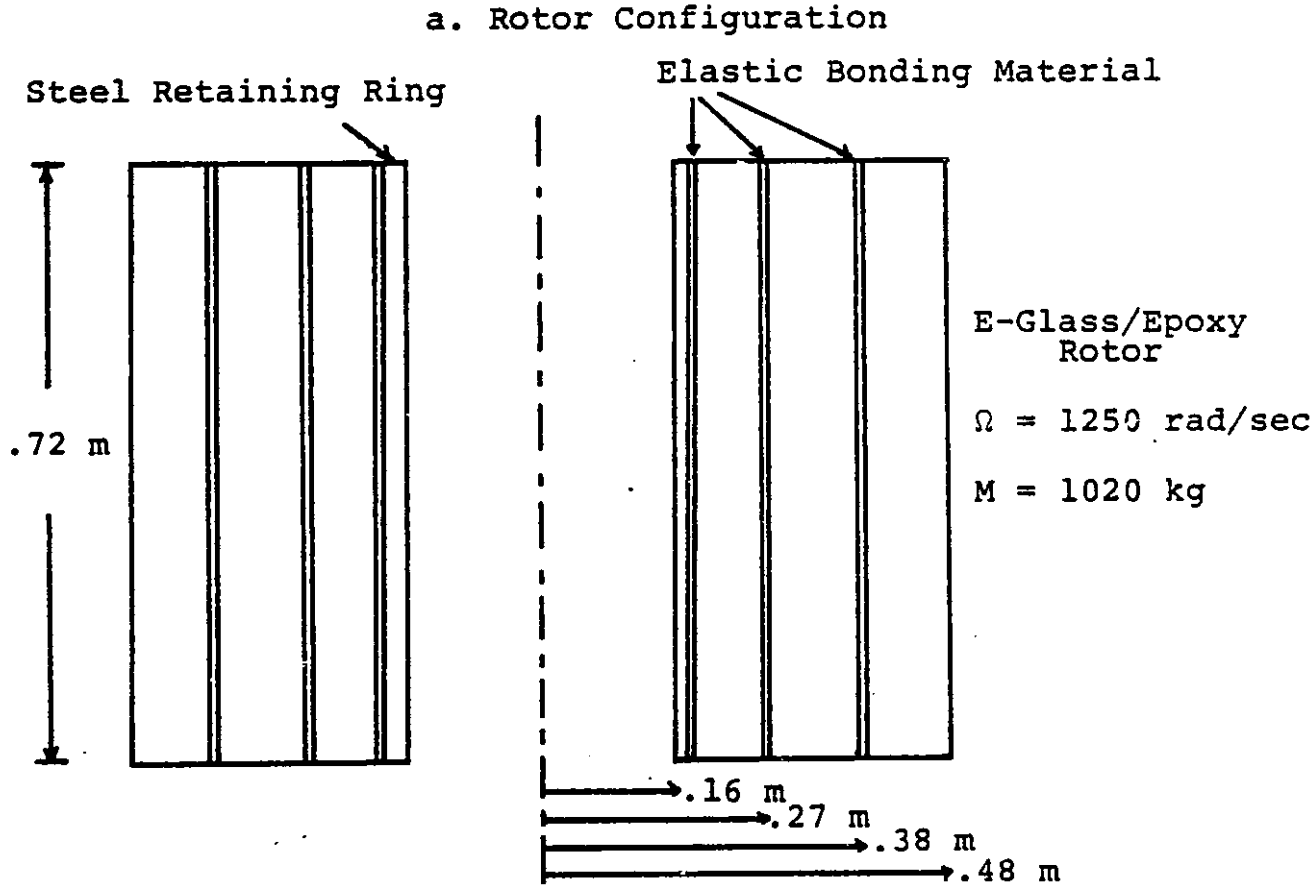

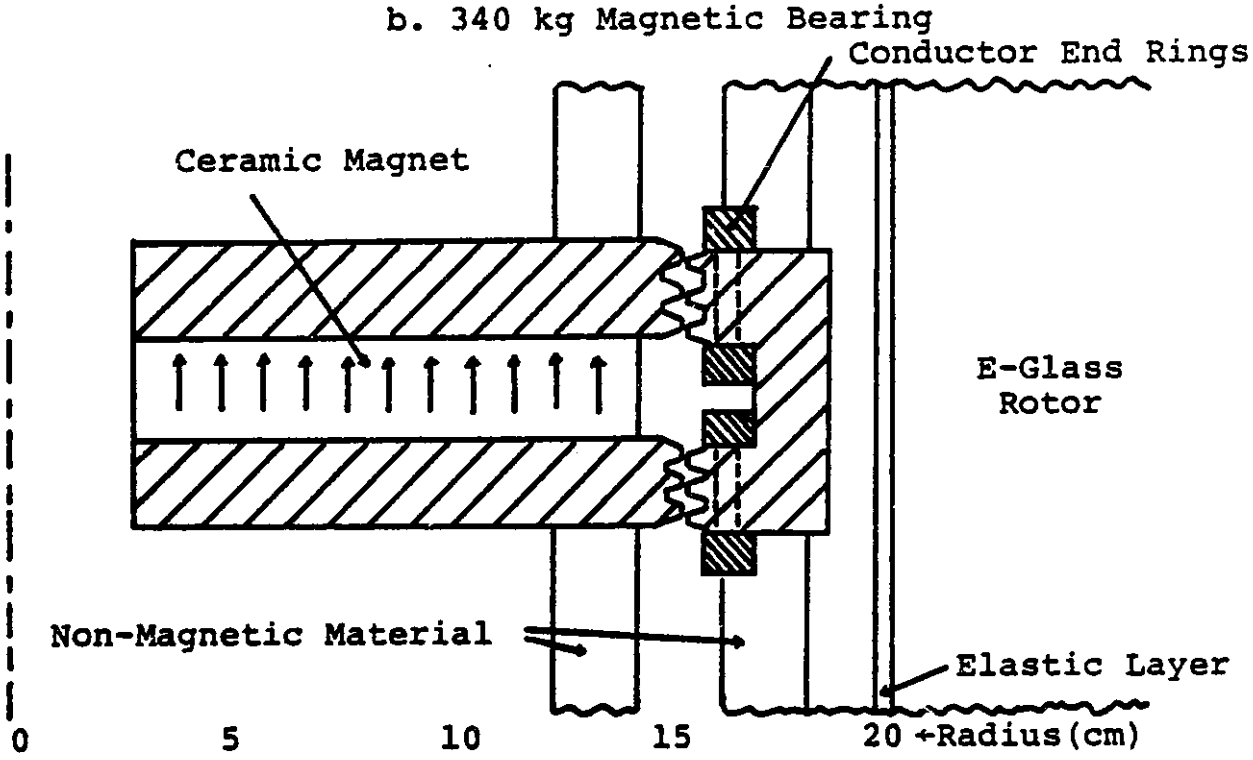

design. The geometry shown is not claimed to be optimum, but is only an intermediate-level design which might lend insight to further improvements. Ceramic magnets are used with an E-glass/epoxy rotor. The system is designed to store 10^8 Joules, or about 25 kilowatt-hours of energy. An aspect ratio h/b of 1.5 is assumed, and material values presented in previous chapters are used.

The basic rotor specifications are determined using equations 2.1, 2.2, and 2.7;

$$b = .48 \text{ m} \qquad h = .72 \text{ m}$$
$$\Omega_{max} = 1250 \text{ rad/sec} \qquad R = 16 \text{ cm}$$
$$M = 1020 \text{ kg} \tag{5.50}$$

The individual rings must be sized to keep their radial stresses within limits. The maximum allowable radial stress in E-glass is about 40 MPa, 5% of its longitudinal strength. Using figure 2.3, at the maximum rotational speed a conservative a/b ratio of .80 is acceptable. Thus an elastic layer is needed at r=.38 m. This becomes the outer radius for the next ring. This rim is not stressed as heavily as the outer layer, and an a/b ratio of .70 is acceptable. Thus another elastic layer is needed at r=.27 m. The remaining ring has an a/b of .6, which is acceptable as well. Each elastic layer is given 5 mm of space off of the inside edge of each ring so that the outer dimensions are unchanged. Finally, a thin steel retaining ring is added on the innermost surface. The result is the rotor of figure 5.3a.

The design of the magnet system begins with a determination of the number of separate bearings to be used. It has been shown that it is desirable to have several flux paths to reduce the volume of iron required. The gap width, from equation 5.16 is .75 mm. The toothed structure will be the optimum found in chapter 3, part H, having $\lambda/g=10$. A minimum of three teeth per gap is desirable, making the minimum area for each gap

$$A_{g\ min} = 2\pi R(3 \cdot 10 \cdot .75mm) = .023\ m^2 \qquad (5.51)$$

The total gap area needed for the levitation of a 1020 kg rotor is, from equations 3.75 and 5.16,

$$A_{gT} = \frac{2gM\mu_o}{B_g^2 f_2} \simeq .14\ m^2 \qquad (5.52)$$

for B_g=1.8 Tesla. Thus there can be six separate gaps, corresponding to three individual bearing sections. Emphasis will be placed on the design of a single bearing having a load capacity of 340 kg.

From equation 3.65 the volume of magnets can be found. η is initially chosen to equal .75.

$$V_m = \frac{2\ M\ g\ g}{\eta (BH)_m\ f_1} \simeq 1.6 \cdot 10^{-3}\ m^3 \qquad (5.53)$$

The face area of the magnet is given by equation 3.83 with p=2, A_m=.067 m^2, and the thickness must be V_m/A_m=2.4 cm.

The total flux in the circuit is roughly

$$\Phi = \frac{p}{p+1} B_o A_m \simeq .017 \text{ Wb} \qquad (5.54)$$

In order to carry this flux, the iron pole pieces must have a cross-section normal to the flux of

$$A_i = \frac{\Phi}{B_i} \simeq .015 \text{ m}^2 \qquad (5.55)$$

A bearing with dimensions meeting the specifications given is shown in figure 5.3b

b. Analysis

The proposed bearing design will be analyzed using the circuit-analog methods of chapter 3. The steel retaining ring is considered to be highly permeable for the purposes of estimating leakage flux. The factor

$$\frac{A_o}{R_0 g_0}$$

is assumed to equal 3, and the pole pieces are made of dynamo-grade iron.

The magnet's circuit parameters are, from figure 3.5,

$$\Psi_o = 7090 \qquad R_m = .268 \text{ MA/Wb} \qquad (5.56)$$

The gap has a reluctance at $\delta/\lambda = .2$ of

$$R_g = \frac{2 \cdot 2.75 (.75\text{mm})}{\mu_o (2.26 \cdot 10^{-2} \text{m}^2)} = .145 \text{ MA/Wb} \qquad (5.57)$$

The average path length for the flux through the bulk iron is about 19 cm. The effective cross-section is at least .017 m .

If there were no losses, the flux would be

$$\Phi = \frac{\Psi_o}{R_m + R_g} = .017 \text{ Wb} \tag{5.58}$$

yielding an iron flux density of 1 Tesla. At this density, from figure 3.9, $\mu_i = 3500\mu_o$. Thus the iron reluctance is on the order of 2.5 kA/Wb. The leakage reluctance can be estimated using the arcs-and-lines technique as approximately .7 MA/Wb. Therefore $\eta = .77$, close to the original design estimate. The effective circuit parameters become;

$$\begin{aligned} \Psi_o' &= 5130 \qquad & R_{eq} &= .122 \\ R_m' &= .196 \text{ MA/Wb} \end{aligned} \tag{5.59}$$

From these values the force and stiffness can be calculated using the formulas given in chapter 3:

$$\begin{aligned} f_z &= 3480 \text{ N} \\ S_z &= 1.7 \text{ N/}\mu\text{m} \end{aligned} \tag{5.60}$$

The stabilization system can be analyzed for full-speed operation using the narrow-gap limit from chapter 4. The normal derivative gap-influence coefficient, f_{1n}, was calculated using the tooth-reluctance computer program described in section 3H. It was found to be .49 for $\lambda/g=10$, $t/\lambda=.25$, $\delta/\lambda=.2$, as is used in the design shown. Calculations of stiffness are based on three identical bearings of the type just described.

The stiffness at full speed is

$$S_{x_{max}} = 270 \text{ N/mm} \tag{5.61}$$

From figure 5.3, the geometry functions (f) can be evaluated for the iron pole pieces;

$$f_1 \sim 7 \qquad f_3 \sim 1$$
$$\mu_1 = \mu_3 \approx 1000\mu_o \tag{5.62}$$

Therefore the speed for stability is

$$S^2 > .02 \tag{5.63}$$

or

$$\Omega > 34 \text{ rad/sec} \quad (320 \text{ rpm}) \tag{5.64}$$

The fundamental translational mode frequency is

$$\omega_o = \sqrt{\frac{S_x}{M}} = 16 \text{ rad/sec } (2.6 \text{ Hz}) \tag{5.65}$$

Only the essential results of the analysis of this structure have been given. Much more work remains to be done in the optimization of this and other similar bearing designs before any one concept is accepted to the exclusion of others.

C. Further Investigation

The first thing that needs to be tested in the proposed system is the stabilization scheme. A small rotor could be designed to have a low minimum speed for stability. First

experiments could even replace the magnetic levitation by a flexible hanging support. Of particular concern are stability against torsional modes and reaction to step displacements.

Another aspect of the system for which no simple analytical methods are available is the determination of the damping constant of the stabilization system. Magnetic levitation is inherently low in damping, but some means for predicting this parameter is needed.

The details of the motor-generator have not been examined. Because this aspect of the system has an influence on the stability of the levitation, work needs to be done on designing an efficient variable-speed machine which is compatible with the proposed design.

Levitation by transverse magnetic forces is less efficient than normal forces, by a factor of 4.5 compared to a toothed axial structure, and by a factor of 6.5 compared to opposing flat plates. Because of this, some thought should be given the possibility of providing at least some of the lift with normal forces, while keeping the axis of stabilization in the radial direction. The generation of a new stabilization concept might be required to fully realize this option.

Finally, more information is needed on the dynamics of the rotor. In particular the extent and behavior of rotor imbalance and its effect on power dissipation in the stabilization system needs review.

The ultimate goal of this project should be to design a complete flywheel energy storage system which is

cost-effective, uses widely available materials, and is safe and reliable enough to find acceptance in the consumer market. To succeed would substantially increase the desirability of photovoltaics as a residential energy source.

APPENDIX 1: LINCOLN LAB BEARING ANALYSIS

While working on a flywheel energy storage system for spacecraft at MIT's Lincoln Lab, Alan Millner designed an actively-controlled magnetic bearing for use in conjunction with the project. A test system was built in 1977. Since then, this same bearing has been used by Millner, now with Lincoln Lab's solar energy division, as a prospect for flywheel storage systems [49]. One of these bearings was tested for lift force as a function of air-gap width by Duncan Hay, magnetic-system engineer. These measurements constitute a good check on the accuracy of the models proposed in chapter 3.

Shown in figure A1.1 are the physical dimensions of the bearing, taken from detailed mechanical drawings. The magnetic properties shown in figure A1.2 are based on the stated bearing dimensions. The values given for the iron reluctance are for bulk only. The reluctance of the teeth themselves is deferred. Permeabilities are from figure 3.9. The permanent magnetization value was determined by Millner, utilizing data from the supplier.

The arcs-and-lines technique is applied in figure A1.3 to find the total leakage reluctance. This is combined with the previous results for gap, iron, and magnet properties to solve for the flux in the circuit. From this, the flux density in the teeth is computed. The density is high enough that the tooth iron reluctance could be significant. In figure A1.5

this reluctance is calculated. For the smallest gap, a saturation value for the flux is assumed. From these values a corrected gap flux is determined for each of the four gap widths of interest.

Finally, in figure A1.6, the computed values of Φ_g, R_g, and f_1 are used to predict the lift force. The experimentally measured values are shown for comparison. In light of the fact that the losses are fairly large (η=.48), the agreement is remarkably good.

A few interesting deductions are possible from this analysis. At the intended operating gap of .46 mm, the modified permeance ratio, p, is 1.6. Only 6% of additional lift force could be generated by improving this to p=1. Clearly the dominant concerns are the high flux leakage and tooth iron reluctance. From figure A1.3, the majority of the leakage occurs between the pole-pieces. Some slight improvement might be had by increasing the separation for path 4, but the high pole leakage appears to be a fundamental attribute of the design. Placing the magnet closer to the gap, perhaps in two separate pieces, could improve this situation. The tooth iron reluctance could be reduced by flanging the teeth, but the effect this might have on the transverse stiffness would require evaluation.

Figure A1.1

LINCOLN LAB BEARING-PHYSICAL DIMENSIONS

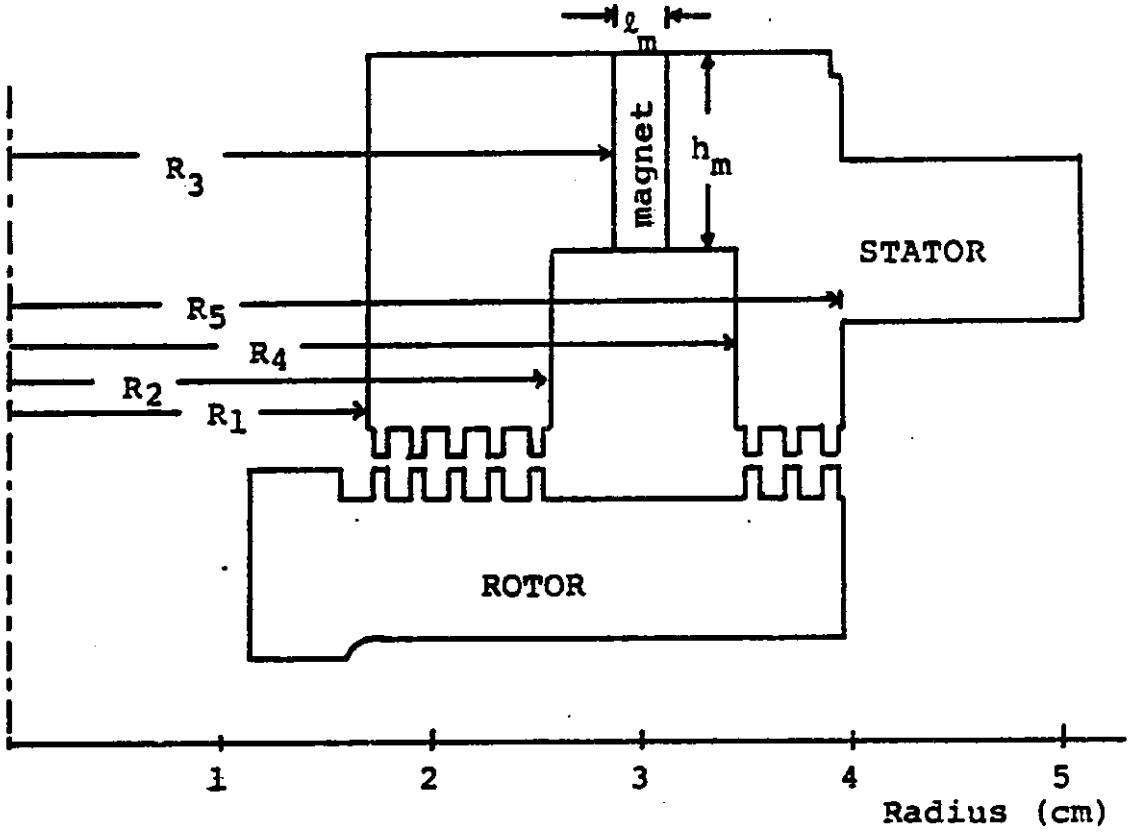

R_1=1.72 cm R_4=3.48 cm h_m=.914

R_2=2.58 cm R_5=3.98 cm

R_3=2.88 cm ℓ_m=.295 cm

Tooth Detail

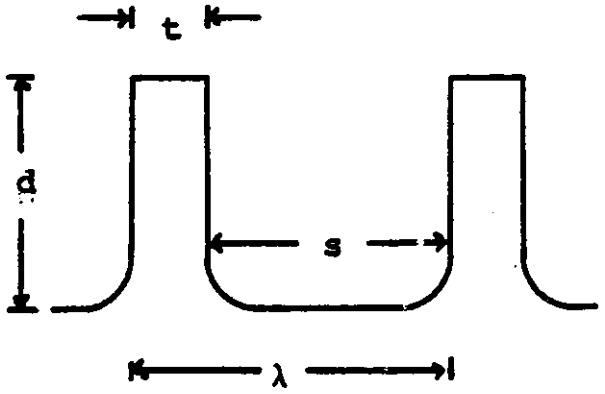

t=.46 mm

s=1.45 mm

d=1.45 mm

λ=1.91 mm

Figure A1.2

LINCOLN LAB BEARING - MAGNETIC PARAMETERS

Magnet

Material: $SmCo_5$, B_o=.8 Tesla, $\mu_m=1.05\mu_o$

Circuit Values: $$\Psi_o = \frac{B_o R_3 \ln\left(\frac{R_3+\ell_m}{R_3}\right)}{\mu_m} = 1700 \text{ A.}$$

$$R_m = \frac{R_3 \ln\left(\frac{R_3+\ell_m}{R_3}\right)}{\mu_m 2\pi R_3 h} = 1.29 \text{ MA/Wb}$$

Gap

Inner Gap Area (based on 5 complete tooth pitches)=12.9.cm^2

Outer Gap Area (based on 3 complete tooth pitches)=13.4 cm^2

t/λ = .241

gap (mm)	λ/g	C	f_1	R_{gin} (MA/Wb)	R_{gout} (MA/Wb)	R_g (MA/B)
.254	7.52	2.11	.686	.331	.319	.654
.457	4.18	1.75	.68	.493	.474	.967
.838	2.28	1.45	.72	.75	.722	1.47
1.09	1.75	1.36	.748	.916	.882	1.80

Iron

Material: AISI Type S-5, 1.85%Si (similar to Dynamo grade)

Bulk Iron: Area = 12 cm , Length 17 cm.

gap (mm)	Flux (mWb)	$\overline{B}$ (T)	μ_r/μ_o	R_i (MA/Wb)
.254	.876	.73	5000	.023
.457	.753	.63	6000	.019
.838	.616	.51	7000	.016
1.09	.55	.46	6000	.018

Figure A1.3

LINCOLN-LAB BEARING - LEAKAGE FLUX

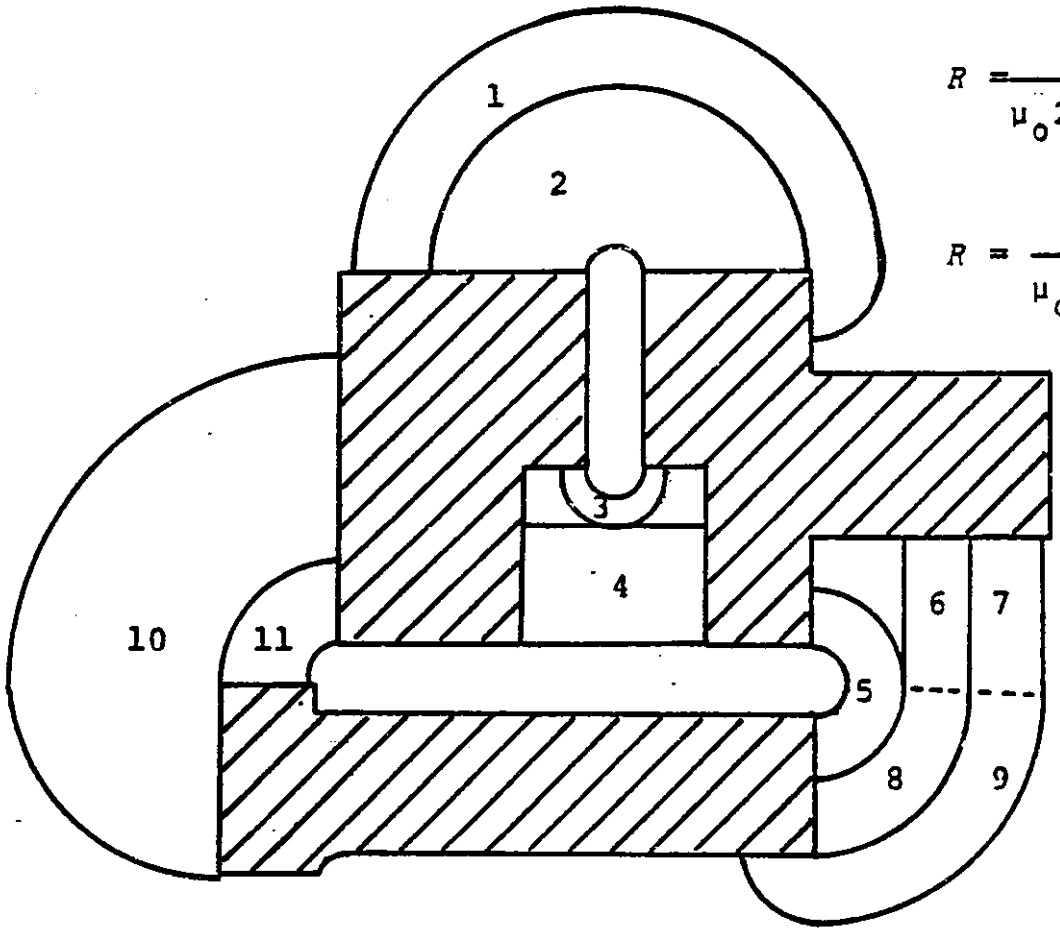

$$R = \frac{\theta}{\mu_o 2\pi \bar{R} \ln(r_2/r_1)}$$

or

$$R = \frac{\ell}{\mu_o 2\pi \bar{R}(r_2 - r_1)}$$

Path #	Avg. Radius (cm)	R (MA/Wb)
1	3.0	34
2	3.0	7.6
3	3.0	22
4	3.0	6.3
5	4.0	9.1
6	4.5	5.2
7	5.0	5.2
8	4.2	6.8
9	4.3	15
10	1.0	18
11	1.5	10

Total reluctance from pole-to-pole

R_ℓ = 2.2 MA/Wb

Figure A1.4

LINCOLN LAB BEARING-PRELIMINARY CIRCUIT ANALYSIS

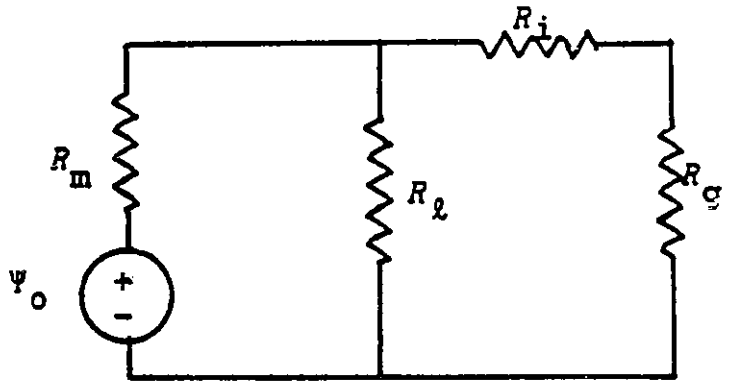

$\Psi_o = 1700$ $\quad R_\ell = 2.2 \cdot 10^6$

$R_m = 1.29 \cdot 10^6$ $\quad R_i = .02 \cdot 10^6$

gap (mm)	R_g (MA/Wb)	R_{eq} (MA/Wb)	R_m' (MA/Wb)	Ψ_o' (A)	$-\Phi_m$ (mWb)	Φ_g (mWb)
.254	.650	.514	.833	1070	.942	.722
.457	.967	.681	.833	1070	.863	.594
.838	1.47	.888	.833	1070	.780	.465
1.09	1.80	.996	.833	1070	.744	.406

gap (mm)	B_g (T)	B_{max} (at base of teeth)
.254	1.2	2.3
.457	.79	1.9
.838	.51	1.5
1.09	.42	1.3

Figure A1.5

LINCOLN LAB BEARING - TOOTH IRON RELUCTANCE

Since most of the flux which enters a tooth moves nearly its entire length before exiting, the appropriate value of flux density to use when calculating the iron tooth reluctance is the induction of the base of the tooth.

gap (mm)	B_{base} (T)	μ/μ_o	R_i (teeth) (MA/Wb)	R_i (total) (MA/Wb)
.254	2.3	*	*	*
.457	1.9	50	.286	.305
.838	1.5	500	.029	.045
1.09	1.3	1500	.010	.028

* this flux density is well into the saturation region. A good model is to assume that the tooth-base flux density is limited to 1.9 T.

Figure A1.6

LINCOLN LAB BEARING - FINAL CIRCUIT ANALYSIS

$\Psi_o = 1700$, $R_m = 1.29 \cdot 10^6$, $R_\ell = 2.2 \cdot 10^6$

gap (mm)	R_g (MA/Wb)	R_i (MA/Wb)	R_{eq} (MA/Wb)	R_m' (MA/Wb)	Ψ_o (A)	$-\Phi_m$ (mWb)	Φ_g (mWb)
.254	.650	-	-	-	-	-	.610*
.457	.967	.305	.806	1.12	1070	.811	.513
.838	1.47	.045	.897	.858	1070	.777	.460
1.09	1.80	.028	.998	.841	1070	.743	.405

* Based on tooth-base flux density of 1.9 T

Figure A 1.6

LINCOLN LAB BEARING - FORCE ANALYSIS

$$f_z = -\tfrac{1}{2}\,\phi_g^2\,\frac{\partial R_g}{\partial z} = \frac{\tfrac{1}{2}\,\phi_g^2\,R_g}{g}\left[\frac{-1}{C}\,\frac{\partial (Cg)}{\partial z}\right]$$

gap (mm)	ϕ_g (mWb)	R_g (MA/Wb)	f_1	Lift Force Model (N)	Lift Force Experiment (N)	error (%)
.254	.610	.650	.686	325	310	5
.457	.513	.967	.680	190	190	0
.838	.460	1.47	.720	135	120	12
1.09	.405	1.80	.748	100	95	5

APPENDIX 2

Consider the following simple problem:

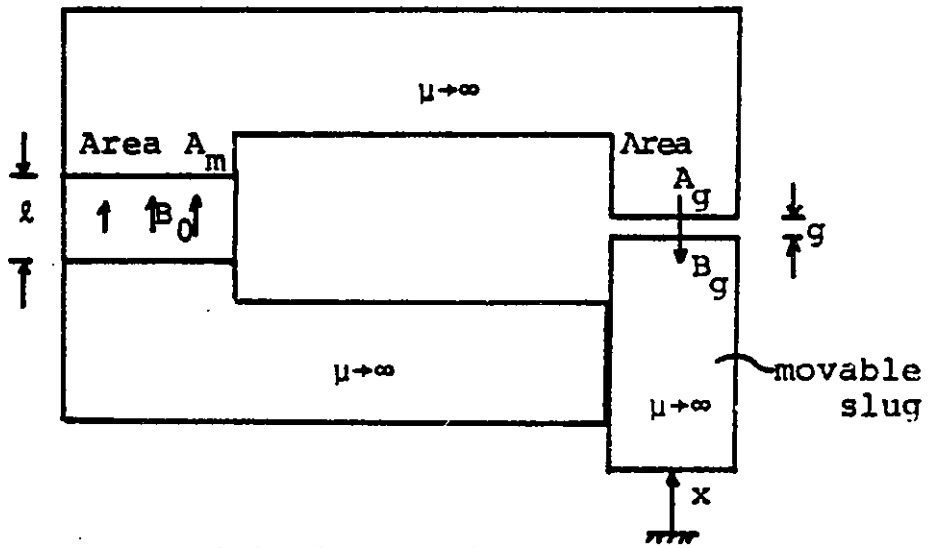

Neglect leakage, fringing of fields, and the reluctance of the sliding contact. Assume that in the magnet $B_m = B_o + \mu_m H_m$, and in the gap $B_g = \mu_o H_g$.

a. Traditional Energy Method

The total energy in the magnetic fields is found using

$$W_f = W_m + W_g$$

$$W_m = A_m \ell \int_0^{B_m} H_m \delta B_m' = A_m \ell \int_0^{B_m} \frac{B_m' - B_o}{\mu_m} \delta B_m'$$

$$= A_m \ell \left[\frac{B_m^2}{2\mu_m} - \frac{B_o B_m}{\mu_m} \right]$$

$$W_g = A_g \cdot g \int_0^{B_g} H_g \delta B_g' = A_g \cdot g \frac{B_g^2}{2\mu_o}$$

Therefore,

$$W_f = A_m \ell \left[\frac{B_m^2}{2\mu_m} - \frac{B_o B_m}{\mu_m} \right] + A_g \cdot g \frac{B_g^2}{2\mu_o}$$

Ampere's and Gauss' magnetic law relate these quantities:

$$H_m \ell + H_g \cdot g = 0 \qquad B_m A_m = B_g A_g$$

so that W_f can be expressed in terms of the constant, B_o.

$$W_f = -\frac{B_o^2}{2\mu_m} A_m \ell \frac{1}{1 + \frac{\mu_m g A_m}{\mu_o \ell A_g}}$$

The force is given by the derivative,

$$f = -\frac{\partial W_f}{\partial z} = \frac{B_o^2}{2\mu_o} A_m \frac{A_m/A_g}{[1 + \frac{\mu_m g A_m}{\mu_o \ell A_g}]^2}$$

b. Maxwell Stress Tensor

$$f = A_g (\tfrac{1}{2} \frac{B_g^2}{\mu_o})$$

But from Ampere's and Gauss' magnetic law,

$$B_g = \frac{A_m/A_g \; B_o}{[1 + \frac{\mu_m g A_m}{\mu_o \ell A_g}]}$$

Thus $$f = \frac{B_o^2}{2\mu_o} A_m \frac{A_m/A_g}{[1 + \frac{\mu_m g A_m}{\mu_o \ell A_g}]^2}$$

which is the same as in part a.

c. Gap-Flux Method

$$f = -\tfrac{1}{2} \phi_g^2 \frac{\partial R_g}{\partial z} = \tfrac{1}{2} \frac{\psi_o^2}{(R_m + R_g)^2} \frac{1}{\mu_o A_g}$$

$$= \frac{B_o^2}{2\mu_o} A_m \frac{A_m/A_g}{[1 + \frac{R_g}{R_m}]^2} = \frac{B_o^2}{2\mu_o} A_m \frac{A_m/A_g}{[1 + \frac{\mu_m g A_m}{\ell \mu_o A_g}]^2}$$

which is the same once again.

BIBLIOGRAPHY

1. Aaland, K. and J. Lane, "Ideas and Experiments in Magnetic Interfacing," Proceedings of the 1975 Flywheel Technology Symposium, (October 1975), p. 195.

2. Beer, F. and E. Johnston Jr., Vector Mechanics for Engineers, 2nd ed., New York, McGraw-Hill, 1972.

3. Binns, K., "Calculation of some Basic Flux Quantities in Induction and other Doubly-Slotted Electrical Machines," Proceedings of the IEE, 111, (November 1964), p. 1847.

4. Binns, K., M. Jabbar and W. Bernard, "A Rapid Method of Computation of the Magnetic Field of Permanent Magnets," IEEE Transactions on Magnetics, MAG-11, (September 1975), p. 1538.

5. Bohn, G. and J. Langerholc, "Theoretical Calculations of the Electrodynamic Properties of Ferromagnetic Levitation Systems," Journal of Applied Physics, 48, (July 1977), p. 3093.

6. Borcherts, R., L. Davis, C. Wan, A. Mohdulla and J. Reitz, "Parameter Optimization Studies of Magnetic Suspensions for High Speed Ground Transportation," FRA-74-42, (April 1974).

7. Braunbek, W., "Freely Suspended Bodies in Electric and Magnetic Fields," Zeitschrift fur Physik, 112, (1939), p. 753, (English Translation by R. Durham).

8. Brenner III, J., "The External Electric and Magnetic Fields Surrounding an Axially Symmetric Rotating Magnet," MIT Thesis, Physics, 1966.

9. Brobeck, W., "Flywheel Energy Storage for Utility Applications," IEEE Power Engineering Society Summer Meeting, 1977.

10. Carter. F., "The Magnetic Field of the Dynamo-Electric Machine," Journal of the IEE, 64, (1926), p. 1115.

11. Churchill, R., J. Brown and R. Verhey, Complex Variables and Applications, 3rd ed., New York, McGraw-Hill, 1974.

12. Cormack III, A., J. Notti Jr. and M. Ruiz, "Design and Test of a Flywheel Energy Storage Unit for Spacecraft Application," Intersociety Energy Conversion Engineering Conference Record, 1975, p. 1275.

13. Danby, G. and J. Powell, "Integrated Systems for Magnetic Suspension and Propulsion of Vehicles," Proceedings of the 1972 Applied Superconductivity Conference, (May 1972).

14. Danfelt, E., S. Hewes and T. Crow, "Optimization of Composite Flywheel Design," International Journal of Mechanical Science, 19, (February 1977), p. 69.

15. Davis, D., D. Hodson and C. Heise, "Rocketdyne's High-Energy-Storage Flywheel Module for the U.S. Army," Proceedings of the 1977 Flywheel Technology Symposium, (October 1977).

16. Dempsey, F., Arnold Engineering Company, private communication.

17. Dodd, H., "An Assessment of Mechanical Energy Storage for Solar Systems," 12th Intersociety Energy Conversion Engineers Conference, (1977), p. 1174.

18. Earnshaw, S., "On the Nature of the Molecular Forces which Regulate the Constitution of the Luminiferous Ether," Transactions of the Cambridge Philosophical Society, 7, (1842), p. 97.

19. Electrical Materials Handbook, Allegheny Ludlum Steel Corporation, 1961.

20. Federmann, E., W. Feduska, W. McAllister and S. Nearhoof, "Potential for Stand-Alone Photovoltaic On-Site Total-Energy Systems," Conference Record of the Thirteenth Photovoltaic Specialists Conference, (November 1978), p. 1004.

21. Frazier, R., P. Gilinson Jr. and G. Oberbeck, Magnetic and Electric Suspensions, Cambridge, Mass., MIT Press, 1974.

22. Friedericy, J. and A. Raynard, "Garrett's Outlook on Vehicle Flywheels," Proceedings of the 1975 Flywheel Technology Symposium, (November 1975), p. 62.

23. Gallagher, B., D. Bickler and L. Sanchez, "A Candidate Low-Cost Processing Sequence for Terrestrial Silicon Solar Cell Panels," Conference Record of the Thirteenth Photovoltaic Specialists Conference, (November 1978), p. 241.

24. Geary, P., Magnetic and Electric Suspensions, SIRA, Kent, England, 1964.

25. Glicksman, L., "Heat Pumps: Off and Running Again," Technology Review, (June/July 1978), p. 64.

26. Gould, J., "Permanent Magnets," Proceedings of the IEE, 125, (November 1978), p. 1137.

27. Habermann, H. and G. Liard, "Practical Magnetic Bearings," IEEE Spectrum, (September 1979).

28. Hagen, D. and A. Erdman, "Flywheels for Energy Storage: A Review with Bibliography," ASME 76-DET-96, (July 1976).

29. Harris, M., A. Hughes and P. Lawrenson, "Static Torque Production in Saturated Doubly-Salient Machines," Proceedings of the IEE, 122, (October 1975), p. 1121.

30. Heh, H. and M. Shalaby, "Magnetic Levitation with Controlled Permanetic Excitation," IEEE Transactions on Magnetics, MAG-13, (September 1977).

31. Henrikson, C., J. Lyman and P. Studer, "Magnetically Suspended Momentum Wheels for Spacecraft Stabilization," AIAA 74-128, (January 1974).

32. Hodson, D., "Development of a High Energy Storage Flywheel Module," AD-A060-351, (May 1978).

33. Holmes, L., "Stability of Magnetic Levitation," Journal of Applied Physics, 49, (June 1978), p. 3102.

34. Huddleston, R., "Composite Flywheel Development Completion Report," Proceedings of the 1977 Flywheel Technology Symposium, (October 1977).

35. Ireland, J., Ceramic Permanent-Magnet Motors, New York, McGraw-Hill, 1968.

36. Johnk, C., Engineering Electromagnetic Fields and Waves, New York, McGraw-Hill, 1972.

37. Johnson, A., W. Terrill and R. Barchet, "Applied Research on Energy Storage and Conversion for Photovoltaic and Wind Energy Systems," HCP/T22221-01, (January 1978).

38. Jung, V. and B. Rinnert, "Indifferent Magnetic Levitation System with Permanent Magnets and Dynamic Stabilization," Journal of Magnetism and Magnetic Materials, 4, (1977), p. 24.

39. Kaplan, B. and D. Regev, "Dynamic Stabilization of Tuned-Circuit Levitators," IEEE Transactions on Magnetics, MAG-12, (September 1976).

40. Kirk, J., "Flywheel Energy Storage - I," International Journal of Mechanical Science, 19, (1977), p. 223.

41. Kirk, J. and R. Huntington, "Energy Storage - An Interference Assembled Multi-Ring Superflywheel," Intersociety Energy Conversion Engineering Conference, (1977), p. 517.

42. Kirk, J. and P. Studer, "Flywheel Energy Storage - II," International Journal of Mechanical Science, 19, (1977), p. 1155.

43. Kittel, C., Introduction to Solid State Physics, 5th ed., J. Wiley and Sons, New York, 1976.

44. Lee, S. and R. Menendez, "Forces on Current Coils Moving over a Conducting Sheet with Applications to Magnetic Levitation," University of Illinois Electromagnetics Laboratory Report 73-8.

45. Lustenader, E., "Demonstration of an Inductor Motor/Alternator/Flywheel Energy Storage System," COO-4010-1, (September 1976).

46. Lustenader, E., "Laboratory Evaluation of a Composite Flywheel Energy Storage System," UCRL-80604, (January 1978).

47. Melcher, J., Continuum Electromechanics, Cambridge, Mass., MIT Press, 1980.

48. Miericke, J. and L. Urankar, "Theory of Electrodynamic Levitation with a Continuous Sheet Track," Applied Physics, 2, (1973), p. 201.

49. Millner, A., "A Flywheel Energy Storage and Conversion System for Solar Photovoltaic Applications," ASME 79-Sol-1, (December 1978).

50. Millner, A., "Flywheels for Energy Storage," Technology Review, (November 1979), p. 32.

51. Millner, A., personal communication.

52. Mukherji, K. and S. Neville, "Magnetic Permeance of Identical Double Slotting," Proceedings of the IEE, 118, (September 1971), p. 1257.

53. Neville, R., "Solar Energy and the Residence - Some Systems Aspects," Solar Energy, 19, (1977), p. 539.

54. Notti, J., A. Cormack III and W. Schmill, "Integrated Power/Attitude Control System (IPACS) Study," NASA CR-2383 and CR-2384, (April 1974).

55. Papas, C., "On the Contactless Suspension of Objects by Electric and Magnetic Fields," Applied Physics, 13, (August 1977), p. 361.

56. Parker, R. and R. Studders, Permanent Magnets and Their Application, New York, J. Wiley and Sons, 1962.

57. Post, R. and S. Post, "Flywheels," Scientific American, 229, (December 1973), p. 17.

58. Proceedings of the 1975 Flywheel Technology Symposium, (November 1975).

59. Proceedings of the 1977 Flywheel Technology Symposium, (October 1977).

60. Rabenhorst, D., "Use of Flywheels for Energy Storage," Energy Sources, 2, (1975), p. 251.

61. Rabenhorst, D. and R. Taylor, "Design Considerations for a 100-MegaJoule/500 MegaWatt Superflywheel," AD-774-736, (December 1973).

62. Ramakumar, R., H. Allison and W. Hughes, "Solar Energy Conversion and Storage Systems for the Future," IEEE Transactions on Power Apparatus and Systems, PAS-94, (November/December 1975) p. 1926.

63. Rockwell Corporation, "Economic and Technical Feasibility Study for Energy Storage Flywheels," ERDA 76-65, (December 1975).

64. Sabnis, A., J. Dendy and F. Schmitt, "A Magnetically Suspended Large Momentum Wheel," Journal of Spacecraft and Rockets, 12, (July 1975), p. 420.

65. Studer, P., "A Practical Magnetic Bearing," IEEE Transactions on Magnetics, MAG-13, (September 1977), p. 1155.

66. Thomson, W., F. Younger and H. Gorson, "Whirl Stability of the Pendulously Supported Flywheel System," Transactions of the ASME, (June 1977), p. 322.

67. Thornton, R., "Design Principles for Magnetic Levitation," Proceedings of the IEEE, (May 1973), p. 586.

68. Thornton, R., "Magnetic Levitation and Propulsion, 1975," IEEE Transactions on Magnetics, MAG-11, (July 1975), p. 981.

69. Toland, R., "Current Status of Composite Flywheel Development," UCRL-80604, (January 1978).

70. Torossian, R., "Momentum Wheels," Proceedings of the 1975 Flywheel Technology Symposium, (October 1975), p. 195.

71. Urankar, L. and J. Miericke, "Forces on Null-Flux Magnetic Levitation Systems," Journal of Applied Physics, 44, (April 1973), p. 1907.

72. Walowit, J., "A Theoretical and Experimental Investigation of the Magnetic Fields and Forces Arising in Magnetic Suspension Systems," AD/A-006-109, (January 1975).

73. Wang, C., Applied Elasticity, New York, McGraw-Hill, 1953, p. 58-71.

74. Ward, P. and P. Lawrenson, "Magnetic Permeance of Double-Salient Airgaps," Proceedings of the IEE, 124, (June 1977), p. 542.

75. Wiesmann, "Recoma Magnets used in Motors and Bearings," Brown Boveri Review, 62, (May 1975), p. 215.

76. Woodson, H. and J. Melcher, Electromechanical Dynamics, New York, J. Wiley and Sons, 1968.

77. Yonnet, J., "Passive Magnetic Bearings with Permanent Magnets," IEEE Transactions on Magnetics, MAG-14, (September 1978).

78. Zijlstra, H., "Trends in Permanent Magnet Material Development," IEEE Transactions on Magnetics, MAG-14, (September 1978).